UAB
Universitat Autònoma de Barcelona

Persistent current readout for coherent quantum annealing

Luca Cozzolino

Persistent current readout for coherent quantum annealing

Luca Cozzolino

Director: Pol Forn-Díaz
Tutor: Anna Sanpera Trigueros

PhD thesis at the Universitat Autònoma de Barcelona

UAB
Universitat Autònoma
de Barcelona

2025

Year: 2025
Title: Persistent current readout for coherent quantum annealing
Author: Luca Cozzolino

Acknowledgements

This thesis marks the final step of a long journey that began in 2020, and it is only right to thank all the people who made it possible. Of course, I must begin with my supervisor, Pol. First of all, thank you for giving me the opportunity to move to Catalunya and start a new life here. You are a great professional, and I've learned a lot from you. But more importantly, you have incredible human stature. There are many good physicists who supervise students, but very few truly care about the mental health and well-being of the entire group. Thank you for everything you've done for us.

Then, I couldn't possibly continue without mentioning Alba, my lab-wife. We started together, moved desks, built the lab, shouted at each other, and approached life in completely different ways. Still, I would have never learned so much (including the basics of my next job...) or, above all, Catalan. Thank you for always being there.

When I started, I joined a lab full of people I soon felt grateful to call friends. David and Fabian showed us the first steps of PhD life. I learned a lot from them, both inside and outside the lab (e.g. at Molly Malone's). Alongside them, David E. and Yifei were part of my daily routine: Mondays weren't so bad with them around. Later on, my linguistic saviour arrived in the QCT lab: Elia, a Venetian who understands Neapolitan. Besides being a always present PostDoc (whose chapuzas saved, and will save, the lab), he has been a good friend, always available for a coffee when I needed a break to avoid setting the lab on fire.

Years passed, things changed, and new brothers- and sisters-in-arms joined the group. Ariadna, Guille: thank you for the laughs and the support during this last stretch. A special thanks to Manel, who taught me a lot about error bars, and even more about veganism and K2.

Since too many people have passed through our lab, I'll define the QiliBrigade: Chris, Cata, Mirella, Fabio, María, Omar, Adri, Paul, Matthias, Ana... Usually too many around the lab, which became a plus when going out after work ("Thirstday" didn't last long, though). Thank you for the camaraderie and the good times we shared.

A special thanks to the IFAE engineers, especially Alex: working with you made life easier and more fun. And finally, my gratitude and best wishes go to the Comité d'Empresa (only the fight pays off).
Before closing these acknowledgments, I want to thank the people outside the lab who supported me through these challenging years. You are too many, so please don't be offended if I don't name you all.
Thanks to my family for their incessant support. Especially to my sister, for deciding to move here, bringing a little piece of home with her (and a niece!).
Thanks to the Italian group (Stefano, Stefano, Stefano, Biri, Alfredo, Paolo, Costanza, Carmelita, Joana...), the bar group (Sara, Marco P., Federica, Federico, Tai, Maurizio, Manu, Cisky, Fabri, Carlo, Juanjo...), the Can Batlló volunteers (too many to name, but let's mention Glòria, Ale, Mia, Edu, and Marc), the Neapolitan crew (Michi, Julita, Roberta, Maria d'A., Manu, Marina), and the "foreigners" (Tonia, Vale, Ila, Claudio, Vittorio, Cocca, Lino...). To all of you: thank you. Without you, my life here would have been empty.
Clearly, two people deserve special mention.
Thank you to Rafa, for the patience we both need to get along. I honestly can't imagine what the past years would have been like without your support and care. Or maybe I can: "fatal". Thank you for always being there.
And last but not least, the one everyone expected and I almost left out as a joke, thank you to Mattia. You've literally been my everyday companion for five years, through good and bad, like a marriage. Anxiety attacks, joyful moments, and depressing memories wouldn't have been the same without you.
And yet, on the other hand, what must be said — and what everyone, in fact, knows perfectly well — is that[1] this thesis is just the first step of a longer journey, whose end is still unknown.

[1] B. Craxi, Chamber of Deputies, Rome, 3 July 1992

Abstract

Quantum computing is one of the most intriguing challenges for physicists in this century. The possibility to explore new quantum phenomena and solve complex problems is fascinating, and many efforts are in place by the international community to achieve a functioning quantum processor. Among the different types of quantum computers, quantum annealers are perhaps the most promising in the middle term. Today, existing quantum annealers are limited by qubit coherence times, despite their complexity, and they are able to perform coherent quantum annealing processes only for a short time and cannot overcome classical computers. The main goal of this thesis is to advance towards the development of a coherent quantum annealer based on superconducting flux qubits by introducing a novel dispersive readout method. In this thesis, the first formulation and experimental results of a persistent current readout (PCR) circuit, composed of a dc-SQUID resonator, are presented.

Experiments on single, uncoupled flux qubits were realized with conventional dispersive readout methods to establish a benchmark for the PCR. A profound analysis on coherence time is fundamental to understand and, eventually, mitigate noise sources affecting the qubit. Although the best measured value of T_1 is $\sim 40\ \mu$s, the qubits exhibit low coherence times, probably due to flux and environmental electric noise. Moreover, due to uncontrolled parameters during the fabrication process, the qubit gaps resulted to be too low to perform any characterization at the sweetspot.

After analyzing the conventional dispersive readout, which is based on a resonator capacitively coupled to a qubit, other couplings are investigated. In particular, we investigate the galvanic coupling between a qubit and a resonator, and between two qubits. We show that, assuming a small shared inductance, the coupling Hamiltonian reduces to the classical energy stored in the coupling inductor itself. The first system has interesting applications for exploring different coupling regimes, such as the ultrastrong coupling regime, whereas the second system is relevant for studying a qubit coupled to a strongly nonlinear object.

Similarly, the Hamiltonian of two qubits sharing part of the loops is derived. Applying the same methodologies, the coupling Hamiltonian is reduced to the classical

energy stored in the shared inductance, in the limit of low coupling inductance, as in the previous case. This system is the simplest coupling between two qubits. Despite the limited practical value, the Hamiltonian describes the qubit behaviour when coupled to another strongly non-linear object, giving interesting insights for other inductive coupling. Building on these results, the PCR system is defined as dc-SQUID-based resonator coupled to a flux qubit via mutual geometric inductance. The dc-SQUID acts as a non-linear inductor, whose inductance depends on the qubit persistent current state. Fixing the dc-SQUID operational point, a change in the qubit persistent current causes a shift in the resonator frequency. Moreover, adjusting the flux in the dc-SQUID loop, it is possible to decouple the qubit from the readout circuitry, leading to an improvement of the qubit coherence times, while the readout is idle. Moreover, the Hamiltonian of the whole system is derived and particular emphasis is given to the two-photon contribution and the dispersive shift is calculated.

To experimentally demonstrate the PCR, a single qubit device is designed and fabricated. On the chip, the flux qubit is coupled inductively to the dc-SQUID resonator and capacitively coupled to a coplanar waveguide (CPW) resonator. The presence of the CPW permits to perform the conventional dispersive readout measurements, being a benchmark for the PCR. Unfortunately, due to device imperfections, it was not possible to perform any qubit characterization. Nevertheless, the dc-SQUID shift due to the inversion of the qubit persistent current when crossing the sweetspot was observed through a flux period measurement. This result constitutes proof of the concept of the PCR we are presenting, pointing to a new way to design quantum annealers.

Resumen de la tesis

La computación cuántica es uno de los desafíos más fascinantes para los físicos en este siglo. La posibilidad de explorar nuevos fenómenos cuánticos y resolver problemas complejos es apasionante, y la comunidad internacional está realizando muchos esfuerzos para lograr un procesador cuántico funcional. Entre los distintos tipos de ordinador cuánticos, el "quantum annealer" es probablemente el más prometedor a medio plazo. A pesar de ello, los quantum annealers existentes en la actualidad están limitados por los tiempos de coherencia de los cúbits, por lo que no son capaces de llevar a cabo procesos de quantum annealing coherentes en tiempos breves y no logran superar un ordinador clásico.

El objetivo principal de esta tesis es avanzar hacia el desarrollo de un quantum annealer coherente basado en cúbits de flujo superconductores, mediante la introducción de un nuevo método de lectura dispersiva (*dispersive readout*). Por ende, se presenta la primera formulación, en conjunto con los resultados experimentales, de un circuito de lectura de corriente persistente (*persistent current readout* – PCR), compuesto por un dc-SQUID con una capacidad en paralelo.

Se realizaron experimentos con cúbits de flujo individuales desacoplados, utilizando métodos convencionales de lectura dispersiva basados en un resonador acoplado capacitivamente a un cúbit, con el fin de establecer una referencia para los resultados obtenidos del PCR. Para identificar las fuentes de ruido y reducir sus efectos sobre los cúbits es necesario un análisis exhaustivo de los tiempos de coherencia. Aunque los valores medidos de T_1 fuera de los puntos de simetría de los cúbits son altos, aproximadamente 40 s, los tiempos de coherencia de los dispositivos fabricados resultaron ser bajos. Estos resultados probablemente se encuentran asociados al ruido de flujo. Asimismo, errores imprevistos en el proceso de fabricación impidieron la caracterización de los cúbits en sus puntos de simetría, debido a que los valores de los *gaps* obtenidos fueron demasiado bajos.

Posteriormente, tras analizar la lectura dispersiva convencional, se estudian otros tipos de acoplamiento. Específicamente, se investiga el acoplamiento galvánico entre un cúbit y un resonador, y entre dos cúbits. Suponiendo una pequeña inductancia compartida, se demuestra, para ambos casos, que el hamiltoniano de

acoplamiento se reduce a la energía clásica almacenada en el inductor de acoplamiento. Por tanto, el primer sistema presenta aplicaciones interesantes para explorar distintos regímenes de acoplamiento, como el régimen de acoplamiento ultra fuerte (*ultrastrong*), mientras que el segundo sistema es relevante para estudiar un cúbit acoplado a un objeto fuertemente no lineal. A partir de estos resultados, el sistema PCR se define como un resonador, cuya inductancia es constituida por un dc-SQUID, acoplado a un cúbit de flujo mediante inductancia geométrica mutua. El dc-SQUID actúa como un inductor no lineal, cuya inductancia depende del estado de la corriente persistente del cúbit. Al fijar el punto de trabajo del dc-SQUID, el cambio de dirección de la corriente persistente del cúbit provoca un desplazamiento de la frecuencia del resonador. Además, es posible desacoplar el cúbit del circuito de lectura, ajustando el flujo en el lazo del dc-SQUID. De esta forma, el cúbit se aísla de los ruidos provenientes del sistema de lectura, ocasionando una mejora en los tiempos de coherencia, mientras que el resonador está inactivo. Asimismo, se deriva el Hamiltoniano de todo el sistema, prestando especial atención a la contribución de dos fotones, para realizar el cálculo del desplazamiento dispersivo (*dispersive shift*) del resonador.

Para demostrar experimentalmente el PCR, se diseña y fabrica un dispositivo de un sólo qubit acoplando inductivamente al resonador dc-SQUID y capacitivamente a un resonador de guía de ondas coplanar (coplanar waveguide – CPW). La presencia del CPW permite realizar medidas con el método convencional de lectura dispersiva, cuyos resultados sirven como punto de comparación para el PCR. Desafortunadamente, debido a imperfecciones en el dispositivo, no fue posible realizar ninguna caracterización del qubit. No obstante, se observó el desplazamiento de la frecuencia del dc-SQUID causado por la inversión de la corriente persistente del qubit, cuando pasa por el punto de simetría, mediante la medida del período. Este resultado constituye la validación preliminar del PCR que se presenta en la presente tesis, demostrando una nueva forma de diseñar los quantum annealers.

Resum de la tesi

La computació quàntica és un dels reptes més intrigants pels físics d'aquest segle. La possibilitat d'explorar nuos fenòmens i resoldre problems complexos és fascinant, i la comunitat international està realitzant nombrosos esforços per a aconseguir un processador quàntic coherent. Entre els diferents tipus de computació quàntica, el "quantum annealing" és probablement el més prometedor a mitjà termini. Actualment, els "quantum annealers" que ja existexen estan limitats pels temps de coherència dels qubits i no poden realitzar processos de quantum annealing coherent.

L'objectiu principal d'aquesta tesi és avançar en el desenvolupament d'un quantum annealer coherent basat en qubits de flux superconductors, mitjançant la introducció d'una nova metodologia de "dispersive readout". En aquesta tesi, es presenta la primera formulació, juntament amb els resultats experimentals, d'un nou circuit de "persistent current readout" (PCR), compost per un "dc-SQUID" amb una capacitat en paral·lel.

Per a aquesta tesi, es van realitzar experiments amb qubits de flux desacoblats, mitjançant els mètodes convencionals del "dispersive readout". Els resultats constitueixen una referència pels resultats del PCR. Per identificar i reduir els efectes de les fonts de soroll que afecten els qubits, és necessària una anàlisi profunda dels temps de coherència. Tot i que els valors de T_1 mesurats lluny del punt de simetria dels qubits són alts, els temps de coherència dels dispositius fabricats van resultar baixos. Probablement, aquest resultat és degut al soroll de flux. Així mateix, el procés de fabricació va tenir faltes, reflectits en els valors baixos dels "gap" dels qubits i, per això, no es van poder realitzar mesures de caracterització en els seus punts de simetria.

Després d'analitzar el dispersive readout conventional, basat en un ressonador acoblat a un qubit per mitjà de una capacitat, s'investiguen altres tipus de acoblaments. En particular, s'investiga l'acoblament galvànic entre un qubit i un ressonador i entre dos qubits. Mostrem que, suposant una petita inducància compartida, l'Hamiltoniá d'acoblament es redueix a l'energia clàssica emmagatzemada en el mateix inductor d'acoblament. El primer sistema té aplicacions interessants per a tractar diferents

règims d'acoblament, com ara l'acoblament ultrafort, mentre que el segon sistema és rellevant per a l'estudi d'un qubit acoblat a un objecte fortament no-lineal
Basant-nos en aquests resultats, el sistema PCR es defineix com un ressonador, la inductància del qual està constituit per un dc-SQUID, acoblat a un qubit a través de la inductància geomètrica mùtua. El dc-SQUID actua com un inductor no lineal, amb l'inductancia que depèn de l'estat del qubit, expressat en la base de les corrents persistents. Fixant el punt de treball del dc-SQUID, el canvi de direcció de la corrent persistent del qubit provoca un desplaçament de la freqüència del ressonador. Fent servir un dc-SQUID, és possible desacoblar el qubit del circuit de readout, causant un milloria dels temps de coherència. Així mateix, es deriva l'Hamiltoniá de tot el sistema, amb particular èmfasi a la contribució a dos fotons en l'Hamiltoniá d'acoblament. Finalment, es càlcula el dispersive shift del ressonador.
Per a demonstrar experimentalment el PCR, es va dissenyar i fabricar un dispositiu d'un sol qubit acoblat inductivament al ressonador del PCR i capacitivament a un ressonador de guia d'ones coplanar (CPW, de les seves sigles en anglès). La presència del CPW ens permet realitzar les mesures convencionals en el règim dispersiu, els resultats del qual costituiexen una referència pel PCR.
Malhauradament, per imperfeccions en el dispositiu, no va ser possible realitzar cap cataracterització del qubit. Malgrat això, es va observar el desplaçament de la freqüència del dc-SQUID degut a l'inversió de la corrent persistent del qubit, a través de la mesura del període. Aquest resultat constitueix la validació preliminar del PCR que presentem, i mostra una nova manera per dissenyar quantum annealers.

List of publications

- Superconducting penetration depth of Aluminum thin films, *David López-Núñez, Alba Torras-Coloma, Queralt Portell Montserrat, Elia Bertoldo,* ***Luca Cozzolino****, Gemma Rius, M. Martínez and P. Forn-Díaz*, Superconductor Science and Technology (accepted for publication, 2025).
- Superinductor-based ultrastrong coupling in a superconducting circuit, *Alba Torras-Coloma,* ***Luca Cozzolino****, Ariadna Gómez-del-Pulgar-Martínez, Elia Bertoldo and P. Forn-Díaz*, (pre-print), arXiv:2507.09339
- Persistent current readout for coherent quantum annealing, ***Luca Cozzolino****, Elia Bertoldo and P. Forn-Díaz* (in progress)

Contents

List of Figures

1

Introduction to quantum computing

The idea of simulating a quantum system with quantum-based computers started to be common among physicists already in the 80's [1, 2] and novel concepts such as the Shor's algorithm were developed [3, 4]. Among the different possible realizations of a quantum computer [5, 6, 7, 8], in this thesis we focus on superconductor-based quantum processors [9, 10, 11, 12], with a particular emphasis on quantum annealers [13, 14].
To introduce the main concepts of quantum computing, it is necessary to introduce superconductivity. In Sec. 1.1, the principal elements of quantum processors, in Sec. 1.2. In Sec. 1.3, the circuit quantum electrodynamics (cQED) architecture [12, 15], which is extensively employed in this thesis, is introduced. Finally, in Sec. 1.4, the basic aspects of quantum annealing are given.

1.1 Elements of superconductivity

In 1911, Heike Kamerlingh Onnes observed that the Hg resistance vanishes below 4.2 K, discovering in this way a new physical phenomenon: superconductivity. The efforts in understanding superconductivity, brought the discovery of a second key property, the so-called Meissner effect [16]. The effect consists of the magnetic field expulsion from the superconducting material while transitioning to the superconducting state, i.e. a superconductor behaves as a perfect diamagnet.
Later, in 1961, it was experimentally demonstrated that the magnetic flux generated by a current flowing through a superconducting ring is quantized [17], after having been hypothesized [18]. Such magnetic flux quantum is defined as $\Phi_0 \equiv h/2e$.

Meanwhile, in 1962, Brian Josephson theorized about the presence of a supercurrent flowing through two superconductors separated by a thin insulating barrier [19, 20], due to tunnelling of the superconductor wave function. This tunnelling current was firstly measured in [21]. Such effect was later named in Josephson's honour.
To explain these four fundamental properties (zero resistivity, Meissner effect, flux quantization, Josephson effect), several theories have been proposed throughout the 20th century [22, 23, 24, 25]. Nevertheless, for what concerns us, the Ginzburg-Landau theory [23, 26], dispite being a phenomenological model, is sufficient to allow us to introduce several key concepts. This theory is a macroscopic description of superconductors through the definition of a macroscopic quantum state Ψ

$$\Psi = \rho^{1/2} e^{i\varphi} , \tag{1.1}$$

where ρ is the charge carrier density of the "superelectrons"[1] in the material, which is the order parameter of the superconducting phase transition, whereas $\varphi = 2\pi\Phi/\Phi_0$ is the normalized phase common to all superelectrons, with Φ the magnetic flux [28]. Thanks to the definition of such a macroscopic wave function, the main properties of a superconductor could be explained. For brevity, only the Josephson effect will be discussed, being the fundamental element of superconducting quantum computers.

1.1.1 Josephson effect and Josephson junctions

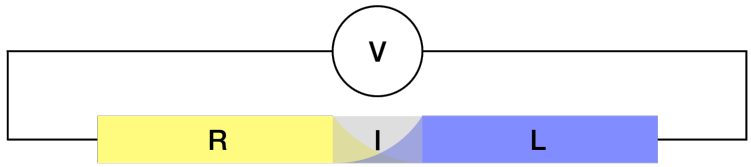

Figure 1.1: Josephson junction schematic with a voltage bias. The module of Ψ_L and Ψ_R are represented by yellow and blue fillings.

Let us consider two superconductors separated by a thin insulating barrier connected to a voltage source V (Fig. 1.1). Being both superconductors described by a macroscopic quantum state, it is possible to write the Schrödinger equations of both

[1] The superelectrons are defined as charge carrier with $Q = 2e$. Later, they were found to be Cooper pairs [27].

leads of the junction in Fig. 1.1

$$\begin{cases} i\hbar\frac{\partial\Psi_L}{\partial t} = -eV\Psi_L + K\Psi_R \\ i\hbar\frac{\partial\Psi_R}{\partial t} = eV\Psi_R + K\Psi_L \end{cases},$$

where $E_R - E_L = 2eV$ and K is the tunnel coupling between the two superconductors. Separating the real from the imaginary parts and using Eq. (1.1), we obtain two equations,

$$\begin{cases} J = J_c \sin\varphi \\ \frac{\partial\varphi}{\partial t} = \frac{2eV}{\hbar} \end{cases}, \tag{1.2}$$

where $J_c = 2K\sqrt{\rho_L\rho_R}/\hbar$ is the maximum current density through the junction, whereas $\varphi = \varphi_R - \varphi_L$ is the phase difference across the junction. If the junction has a constant cross-section, the first equation reduces to $I = I_c \sin\varphi$, where I_c is the critical current. Equation (1.2) are called the Josephson equations and the physical phenomenon is called the Josephson effect.
The Josephson equations can be related taking into account that $\frac{\partial I}{\partial t} = \frac{\partial I}{\partial\varphi}\frac{\partial\varphi}{\partial t}$, leading to

$$V = L_J \frac{\partial I}{\partial t},$$

where

$$L_J = \frac{\Phi_0}{2\pi I_c \cos\varphi}. \tag{1.3}$$

Hence, a Josephson junction can be considered as a nonlinear inductor, with inductance L_J, as defined in Eq. (1.3). The energy stored in such inductor is given by

$$E(\varphi) = \int_0^t IV\,dt' = L_J I^2 = \frac{\Phi_0 I_c}{2\pi}(1-\cos\varphi) = E_J(1-\cos\varphi). \tag{1.4}$$

with $E_J = \Phi_0 I_c/2\pi$.
Note that the phase depends on the magnetic field [22]

$$\nabla\varphi = \frac{2\pi}{\Phi_0}\left(\mathbf{A} + \frac{m}{2e\rho}\mathbf{J}\right). \tag{1.5}$$

Assuming a thick superconductors ($\int \vec{I}\cdot d\vec{l} = 0$), Eq. (1.5) leads to

$$\varphi(x+dx) - \varphi(x) = \oint \mathbf{A}\cdot\mathbf{dl}$$

where $\mathbf{A}$ is the vectorial potential, i.e. $\nabla \times \mathbf{A} = \mathbf{H}$. This dependence affects the current across the junction, leading to

$$I(\Phi) = I_0 \left| \frac{\sin \frac{\pi\Phi}{\Phi_0}}{\frac{\pi\Phi}{\Phi_0}} \right|,$$

where Φ is the magnetic flux applied on the junction surface. To obtain these results, the fluxoid relation was used. [28, 22], for which the magnetic flux is quantized, being Φ_0 the magnetic flux quantum.
Furthermore, due to its geometry, a real junction also has self-capacitance C_J, which must be taken into account in applications in electrical circuits. Josephson junctions are the fundamental element of superconducting quantum circuits, as shown in Sec. 1.2. In Fig. 1.2, a circuit symbol of a real Josephson junction is shown.

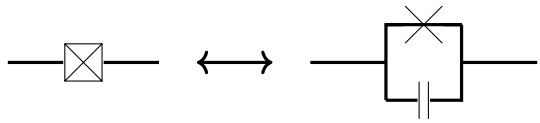

Figure 1.2: Capacitively shunted Josephson junction as a circuit element.

1.2 Quantum circuits

Due to the intrinsic quantum nature of the superconductors, a superconducting circuit behaves as a macroscopic quantum object, i.e. as a quantum circuit. Following [15, 29], the energy of circuital elements, such as capacitors, inductors, and Josephson junctions, can be described as functions of the superconducting phase variables ϕ_X across its ends.
The Kirchhoff equations of the circuit can be seen as the Euler-Lagrange equations [30, 31] of the circuit and in this way the system Lagrangian can be found. Thus, applying the Legendre transformation, it is possible to define the Hamiltonian of the circuit. In Table 1.1, the currents through the principal circuit elements are presented as a function of the phase difference, where each element is assumed between nodes A and B.

C	$I = C(\ddot{\phi}_A - \ddot{\phi}_B)$
L	$I = \frac{\dot{\phi}_A - \dot{\phi}_B}{L}$
Josephson junction	$I = I_0 \sin\left(\frac{2\pi}{\Phi_0}(\phi_A - \phi_B)\right)$

Table 1.1: The currents through the principal circuit elements as function of the phase difference across nodes A and B.

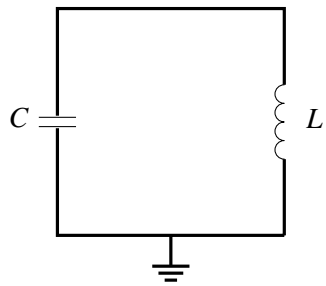

Figure 1.3: LC resonator circuit diagram.

Note that only the Josephson junction has a nonlinear relation with respect to the phase, thus it can used as source of anharmonicity.
Hereby, the main features of the principal quantum circuits are presented.

1.2.1 LC resonator

As explained in Sec. 1.3, the *LC* resonator is a fundamental element in quantum circuits and it is one of the simplest. Following [15, 29, 32], the Hamiltonian of the *LC* circuit in Fig. 1.3 is

$$\hat{\mathscr{H}}_{LC} = \frac{\hat{q}^2}{2C} + \frac{\hat{\phi}^2}{2L} \tag{1.6}$$

where $\hat{q} = 2e\hat{n}$ is the conjugate variable of $\hat{\phi} = (\Phi/2\pi)\hat{\varphi}$. In particular, $[\hat{\varphi},\hat{n}] = i$. Similarly to the quantum mechanical oscillator Hamiltonian, Eq. (1.6) can be rewritten as

$$\mathscr{H}_{LC} = \hbar\omega\left(\hat{a}^\dagger\hat{a} + \frac{1}{2}\right) \tag{1.7}$$

where the annihilation and creation operators, $[\hat{a},\hat{a}^\dagger] = 1$, are defined as

$$\hat{a} = \left(\sqrt{\frac{\hbar}{2C\omega}} + i\sqrt{\frac{\hbar C\omega}{2}}\hat{n}\right) \tag{1.8}$$

with $\omega = (LC)^{-1/2}$. The spectrum defined by Eq. (1.7) is harmonic, since all the elements in the circuit have a linear relation with the phase. In real-life circuits, *LC* resonators are usually realized with coplanar waveguide [33] or lumped-element circuits [34].

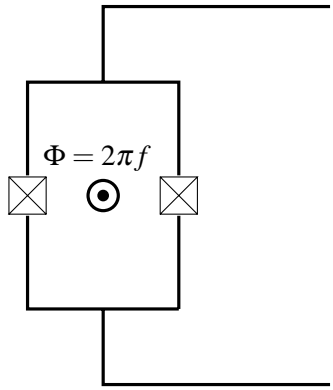

Figure 1.4: Dc-SQUID circuit diagram.

1.2.2 dc-SQUID

A first anharmonic superconducting quantum circuit is the dc-SQUID, which can be realized as a loop with two Josephson junctions, as shown in Fig. 1.4. The name stands for "direct current superconducting quantum interference device", whose meaning is explained at the end of this section.
Defining the current flowing through the left and right junctions as $i_1 = I_1 \sin\gamma_1$ and $i_2 = I_2 \sin\gamma_2$, respectively, it is possible to define the bias current I_b and the circulating current I_{circ} as

$$\begin{cases} I_b = I_0 \sin\gamma_1 + \alpha I_0 \sin\gamma_2 \\ I_{circ} = \frac{I_0 \sin\gamma_1 - \alpha I_0 \sin\gamma_2}{2} \end{cases} . \tag{1.9}$$

where it is assumed $I_1 = I_0 \neq I_2 = \alpha I_0$, $\alpha = I_2/I_1$ and γ_i is the phase difference across the junction i. If $\alpha \neq 1$, the device is called asymmetric dc-SQUID.
Introducing the semi-sum and the semi-difference phases

$$\begin{cases} \varphi_- = \frac{\gamma_1 - \gamma_2}{2} \\ \varphi_+ = \frac{\gamma_1 + \gamma_2}{2} \end{cases} , \tag{1.10}$$

Eq. (1.9) can be rewritten as

$$\begin{cases} I_b = I_0[\sin(\varphi_+ + \varphi_-) + \alpha \sin(\varphi_+ - \varphi_-)] \\ I_{circ} = \frac{I_0}{2}[\sin(\varphi_+ + \varphi_-) - \alpha \sin(\varphi_+ - \varphi_-)] \end{cases} . \tag{1.11}$$

Considering $\alpha \neq 1$, it possible to re-express the results in Eq. (1.11) using the relation

$$A\sin(\xi + \zeta) \pm B\sin(\xi - \zeta) = C\sin(\xi + \theta) .$$

Thus, Eq. (5.14) can be re-expressed as

$$\begin{cases} I_b = I_b^c(\varphi_-)\sin(\varphi_+ + \beta(\varphi_-)) \\ I_{circ} = I_{circ}^c(\varphi_-)\sin(\varphi_+ + \delta(\varphi_-)) \end{cases}, \tag{1.12}$$

with

$$I_b^c(\varphi_i) = I_0\sqrt{1+\alpha^2+2\alpha\cos(2\varphi_i)}, \tag{1.13}$$

$$I_{circ}^c(\varphi_i) = \frac{I_0}{2}\sqrt{1+\alpha^2-2\alpha\cos(2\varphi_i)}, \tag{1.14}$$

$$\beta(\varphi_-) = \arctan\left[\frac{1-\alpha}{1+\alpha}\tan\varphi_-\right], \tag{1.15}$$

$$\delta(\varphi_-) = \arctan\left[\frac{1+\alpha}{1-\alpha}\tan\varphi_-\right], \tag{1.16}$$

where I_b^c (I_{circ}^c) is the critical current for the dc-SQUID bias current (circulating current).
In case of a symmetric dc-SQUID, i.e. $\alpha = 1$, Eq. (1.17) reduces to

$$\begin{cases} I_b = 2I_0\cos\varphi_-\sin\varphi_+ \\ I_{circ} = I_0\sin\varphi_-\cos\varphi_+ \end{cases}. \tag{1.17}$$

Following [28, 35, 36],

$$\varphi_i \equiv \varphi_- = \pi\frac{\Phi_e}{\Phi_0}, \tag{1.18}$$

$$\varphi_e \equiv \varphi_+ = \varphi_{SQ} + \varphi_{DC} \tag{1.19}$$

where Φ_e is the applied magnetic flux, φ_{SQ} is the normalized phase of the dc-SQUID, whereas φ_{DC} is the phase due to the bias current.
The behaviour of I_b^c and I_{circ}^c as function of the external flux $\Phi = 2\pi f$ for different α values are presented in Fig. 1.5. In Fig. 1.5a, the dc-SQUID critical current of the bias current is suppressed for $f = 0.5$, while the critical current of the circulating current is at its maximum, as shown in Fig. 1.5b. Note that the critical currents can be suppressed to zero, if we are in the symmetric case.
Building on Eq. (1.17), Eq. (1.18), and Eq. (1.19), a dc-SQUID can be used as a magnetometer, being able to measure the changes of the magnetic flux Φ_e when biased by a direct current (dc). The interference pattern generated by sweeping the external magnetic flux permits to measure small magnetic field variations and gives the name to the device (Superconducting QUantum Interference Device).
As for the single Josephson junction, a dc-SQUID can be considered as a non-linear

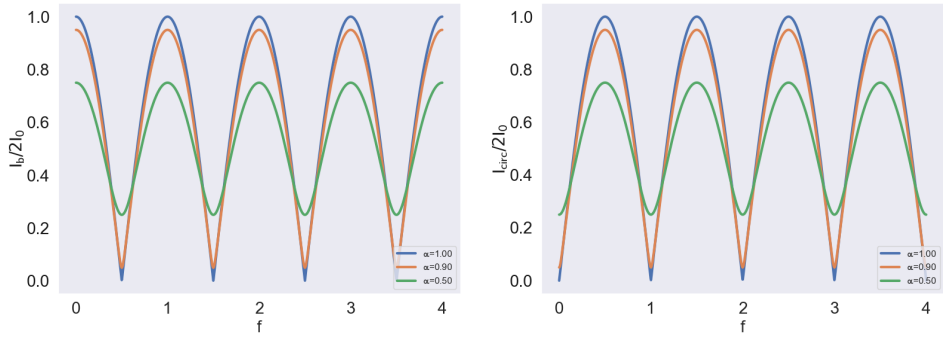

(a) (b)

Figure 1.5: (a) The behaviour of the normalized bias current I_b as a function of the applied flux $\Phi = 2\pi f$ and three values of the junction asymmetry. (b) The behaviour of the normalized circulating current I_{circ} as a function of the applied flux $\Phi = 2\pi f$ and three values of the junction asymmetry.

inductance, under certain assumptions. A profuse discussion of this case and its consequences is presented in Sec. 5.1.
Following [35], the Hamiltonian of a dc-SQUID is

$$\hat{\mathscr{H}}_{SQ} = E_c \hat{q}^2 + E_J \cos\hat{\varphi}_i \cos\hat{\varphi}_e \tag{1.20}$$

where $E_C = e^2/2C_{SQ}$ is the charging energy, $\hat{\varphi}_i$ and $\hat{\varphi}_e$ are the phase operators related to Eq. (1.18) and Eq. (1.19), and E_J is the Josephson energy of a single dc-SQUID junction, as defined in Eq. (1.4). A dc-SQUID has an anharmonic spectrum. In Sec. 5.1, a more detailed discussion on the dc-SQUID is presented, being a fundamental part of this thesis.

1.2.3 Qubit

To realize a quantum computer, it is necessary to define a "quantum bit", i.e. a quantum system with only two states, playing the role of the logic 0 and 1 of the classical computation. To realize this quantum system, called qubit [3], in a physical platform, the system has to show a strongly anharmonic spectrum, in order to isolate two quantum levels from the rest. In fact, if the first two energy levels are well separated from the higher levels, it is possible to reduce the system to a bidimensional Hilbert subspace, defined by the so-called computational basis. Usually, but not always (see Sec. 3.1), the computational basis coincides with the ground and the first excited state, $\{|g\rangle, |e\rangle\}$ of the qubit. In this basis, a generic

qubit state is defined as

$$|\Psi\rangle = \alpha\,|g\rangle + \beta\,|e\rangle \qquad \text{with} \qquad |\alpha|^2 + |\beta|^2 = 1\,,$$

and its Hamiltonian reduces to

$$\mathscr{H}_q = -\frac{\hbar\omega_q}{2}\sigma_z\,, \tag{1.21}$$

where ω_q is the qubit transition frequency between the ground and the excited state and $\sigma_z = |e\rangle\langle e| - |g\rangle\langle g|$ is the Pauli matrix defined in the computational base.
Clearly, Eq. (1.21) is only valid for a qubit isolated from the environment. In real-life cases, external noises cause a loss of information in the qubit state, which takes place over characteristic times, called coherence times. Depending on the effect on the qubit state, we can distinguish an energy relaxation time T_1 and a dephasing time T_2. More details are given in Sec. 3.4.3 and Sec. 3.4.4.
Usually, superconducting qubit realizations are based on Josephson junctions circuits. Other implementations rely on so-called superinductors, which behave as a large arrays of Josephson junctions [37, 38]. The simplest qubit circuit is a *LC* resonator, with the inductor replaced by a Josephson junctions.

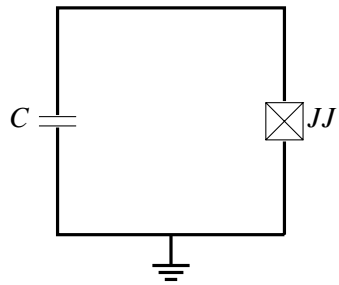

Figure 1.6: Charge qubit circuit diagram.

The device in Fig. 1.6 is known as charge qubit, whose Hamiltonian is given by

$$\hat{\mathscr{H}} = 4E_c\hat{n}^2 - E_J\cos\hat{\varphi}\,,$$

with E_c the charging energy and E_J the Josephson energy.
The name refers to the fact that the qubit state is determined by the accumulation of charge carriers. The first realizations of this circuit were under the name of Cooper pair box and were characterize with a ratio $E_J/E_c \approx 1$. The Cooper pair box was strongly limited by charge noise. A successive version of this qubit, called transmon [11], included a larger capacitance, i.e. $E_J/E_c \gg 1$, leading to a low sensitivity to charge noise.

Furthermore, recalling Eq. (1.20), a dc-SQUID can be operated as a qubit, under suitable circumstances. In particular, dc-SQUIDs were used in phase qubit implementations [39]. Phase qubits are characterized by $E_J \gg E_c$ ans its first realizations were based on a single Josephson junction in an inductive loop, biased by a current. The phase qubit states are defined by the local minima of the potential energy with respect to the phase variable.
Between the charge and the phase qubit, the so-called flux qubit is characterized by $E_J/E_c \sim 100$. Flux qubits are composed of a loop with three [40, 9] or more Josephson junctions [41]. The qubit state is defined by the direction of the macroscopic current circulating in the qubit loop. A more comprehensive presentation of a flux qubit is given in Sec. 3.1.

1.3 Circuit Quantum Electrodynamics

As a two-state quantum system, a qubit can be regarded as an artificial atom, with properties which in a specific parameter range can be designed and fabricated to meet the requirements. This consideration has inspired the so-called circuit quantum electrodynamics (cQED) [12], where the common cavity-atom system of quantum optics is replaced by the superconductor-based qubit-resonator system to investigate light-matter interactions.
The total Hamiltonian of a qubit coupled to a resonator can be expressed as

$$\mathscr{H} = \hbar\omega_r \hat{a}^\dagger \hat{a} - \frac{\hbar\omega_q}{2}\sigma_z + \mathscr{H}_{int} \ ,$$

where $\mathscr{H}_{int}$ is a generic interaction Hamiltonian. The Hamiltonian defines a Hilbert space with basis $\{|g\rangle, |e\rangle\} \otimes |n\rangle$. Thus, a generic quantum state is defined as $|\Psi\rangle$

$$|\Psi\rangle = \sum_n (c_n |g,n\rangle + d_n |e,n\rangle) \ .$$

Typically, the whole Hamiltonian is simplified in order to reduce it to the famous Jaynes-Cummings model Hamiltonian $\mathscr{H}_{JC}$

$$\mathscr{H} = \hbar\omega_r \hat{a}^\dagger \hat{a} - \frac{\hbar\omega_q}{2}\sigma_z + \hbar g(\hat{a}^\dagger \hat{\sigma}_- + \hat{a}\hat{\sigma}_+) \ ,$$

where $[\hat{\sigma}_+, \hat{\sigma}_-] = \sigma_z$ are the ladder Pauli matrices and g is the so-called coupling strength. Hence, a generic dressed state of the system can be defined as

$$|\Psi\rangle = \sum_n \left[\cos\frac{\theta_n}{2}|g,n\rangle + \sin\frac{\theta_n}{2}|e,n-1\rangle\right] \tag{1.22}$$

with $\theta_n = \arctan(2g\sqrt{n}/\delta)$, where $\delta \equiv \omega_r - \omega_q$ is the detuning [42]. When $|\delta| \gg |g|$, the system is in the so-called dispersive regime, where the changes of state of the artificial atoms change the frequency of the resonator [43].
In this regime, the state of the qubit can be "read" by observing the resonator frequency shift, without probing directly the qubit. This measurement method is known as dispersive readout measurement.
Due to the coupling with the resonator and, thus, with the environment, the qubit is affected by noise, causing an energy relaxation decay and dephasing processes of the quantum state. Hence, studying the interactions between the resonator and the qubit can provide information about the nature of the decoherence processes. Understanding these processes is fundamental to design devices with high coherence times, which is necessary for quantum computing.

1.4 Introduction to quantum annealing

Historically speaking, the first implementation of quantum computing was proposed as the quantum version of classical computing, i.e. a quantum processor where quantum bits are manipulated by discrete quantum logic gates. Digital quantum computing, or gate-based quantum computing, is widely implemented by the scientific community and major industry players of the field, such as Google or IBM. In principle, a gate-based quantum processor can perform any algorithm if provided with enough resources. For this reason, a digital quantum computer is a candidate for the realization of a universal quantum computer. A throwback of this quantum computing technology is the necessity of error-correction routines.
Later, a second approach to quantum computing was proposed, where the qubits are manipulated by continuously changing the energy landscape, i.e. by continuous variation of the frequencies and the interactions between the qubits. In other words, in analog quantum computing, the system is initially described by the initial Hamiltonian, $\mathscr{H}_0$, which is modified until the final Hamiltonian, $\mathscr{H}_f$, is reached. Based on this concept, adiabatic quantum computing was developed. Adiabatic quantum computing is based on the adiabatic theorem, which affirms that if a system sits in a given state and evolves slowly enough, it will remain in that state. This approach is demonstrated to be equivalent to the gate-based quantum computing; thus, it leads to a universal quantum computer. Nevertheless, the exact definition of the parameters necessary to build an adiabatic quantum processor is not obvious, leading to few promising results, so far.
In this framework, quantum annealing offers a mid-term solution in which computing universality is sacrificed in favor of a pragmatic approach to quantum computing. In a quantum annealing processor, as known as quantum annealer, the state is pre-

pared in the ground state of a well-known Hamiltonian $\mathscr{H}_0$ and then the Hamiltonian is adiabatically transformed to the final $\mathscr{H}_f$, whose ground state represents the solution to a specific problem, i.e. a given processor can compute only problems that can be encoded in the given $\mathscr{H}_f$. In other words, taking a liner time interpolation between $\mathscr{H}_0$ and $\mathscr{H}_f$,

$$\mathscr{H} = \left(1 - \frac{t}{T}\right)\mathscr{H}_0 + \frac{t}{T}\mathscr{H}_f \ ,$$

where T is the total time of the annealing schedule, i.e. the time necessary to perform the annealing algorithm. It is clear that the qubit coherence times have to be larger than T to perform a coherent annealing schedule.
Valuable realizations of quantum annealers have been achieved employing flux qubits, whose coherence times have been shown up to $100\,\mu$s [44, 45, 46, 47, 48]. Hence, it is fundamental to enhance qubit coherence times to realize a coherent quantum annealer. Thus, it is fundamental to understand and mitigate the main decoherence processes, one of them being the coupling to the readout resonator. In this thesis, we will focus on qubit interactions with resonating circuits, leading to the definition of a novel persistent current readout circuit, that aims to minimize the impact on qubit coherence.

1.5 Thesis overview

Based on the concept so far presented, the aim of this thesis is to present a novel readout for quantum annealing able to enhance the coherence time of the qubit.
As a first step for a better understanding of the qubit interactions, in Ch. 3, the Hamiltonians of an isolated flux qubit and of a flux qubit capacitively coupled to a linear resonator are presented and discussed. Particular emphasis is given to corrections to the dispersive shift estimate presented in [49]. Then, the chip design and its realizations are described, along with the experimental results. More details on the fabrication process and measurements are presented in Ch. 2.
The focus on a single flux qubit capacitively coupled to a resonator leads to the analysis of different qubit couplings in Ch. 4. In detail, in Sec. 4.1 the Hamiltonian of a flux qubit galvanically coupled to a resonator is presented, whereas the interaction between two flux qubits galvanically coupled to each other is discussed in Sec. 4.2. The analysis presented in Ch. 4 is preparatory to the presentation of a novel readout circuit. The persistent current readout presented in Ch. 5 consists of a dc-SQUID based resonator that couples to the flux qubit via mutual geometric inductance, permitting the direct detection of the persistent current state of the qubit. Being dc-SQUID based, one of the most important features of this readout resonator is the possibility to decouple it from the flux qubit, by biasing the dc-SQUID to a

flux-insensitive point. The system is first studied in a semiclassical framework in Sec. 5.1, to later derivate the dc-SQUID resonator Hamiltonian. Finally, the quantum optics model of the whole system is presented and discussed.
In Ch. 6, a chip design for persistent current readout benchmarking is presented. In the end, the experimental results of the persistent current readout are given. Even though it was not possible to fully characterize the qubit, the proof of concept of the persistent current readout is presented. Further steps are discussed in Ch. 7, where the future perspectives of this thesis are presented.

2

Experimental methods

In this chapter, we outline the experimental methods used along this thesis. In Sec. 2.1, we present the software used to simulate the different components of the chips designed. Then, the process to fabricate chips is described in Sec. 2.2. Once a chip is fabricated, it is placed in the experimental setup presented in Sec. 2.3 and measured with the techniques described in Sec. 2.4

2.1 Design software

The design process of a chip is not linear: usually a chip is firstly designed, then simulated, and, according to the results, the design is adjusted. This process is repeated until the simulations lead to the desired circuit parameters.
Working in the cQED framework, inductances, capacitances and and microwave transmission lines are the main components to be simulated. The different simulation software packages used in this thesis are presented hereinafter in this section.

FastHenry is a frequency-dependent impedance extraction software from a generic 3D conductive structure, developed in the Massachusetts Institute of Technology [50]. Although the software was initially developed for normal conductors circuits, later versions permit the simulation of superconducting circuits, by solving the London equations [22].

To simulate a circuit, it is necessary to define the structure through nodes and the segments between them. Thus, fixing the frequency range of the simulation, the input and output ports of each circuit component, and the London penetration depth, the software provides the impedance matrix between the ports. If two ports are connected by a conductor, FastHenry evaluates the galvanic inductance between the two point. If the ports are located in different structures, it computes the mutual geometric inductance between the structures. FastHenry is the only finite-element solver that takes into account the kinetic inductance [34].

```
* Default units will be micrometers
.units um

* Default height will be 10nm and width
      20nm.
.default nwinc=7 nhinc=7 h=0.01 w=0.02

* Thickness is 50nm
.default z = 0.05

* Make it superconductor
.default lambda=0.150

* Let's define wire A
nQA_1 x=0 y=0
nQA_2 x=0 y=-5
* Port definitions
.external nQA_1 nQA_9 wire A

.freq fmin=1.59155e11 fmax=1.59155e11 ndec=1
.end
```

Figure 2.1: Example of code for a FastHenry simulation.

In our simulations, since the results are given as $Z = j\omega L = j(2\pi f)L$, the frequency f is fixed at $f = 1/2\pi$. In this way, the matrix elements provides directly to the inductances written in Henrys. In this work, FastHenry plays a fundamental role, particularly to design the chip presented in Ch. 6, where it is used to compute the mutual inductance between two loops. An example of a FastHenry code is presented in Fig. 2.1.

COMSOL is a finite element analyser software that simulates a large set of physics phenomena [51]. In this thesis, COMSOL is mainly used to estimate the capacitances on a chip. To perform a simulation, the whole structure has to be accounted for, including the substrate and the air surrounding the chip. Defining the conductors on the chip as ports, it is possible to evaluate the Maxwell capacitance matrix of the system. For a network of three conductors, the Maxwell capacitance matrix is defined as

$$\begin{pmatrix} C_{11}^M & C_{12}^M & C_{13}^M \\ C_{21}^M & C_{22}^M & C_{23}^M \\ C_{31}^M & C_{32}^M & C_{33}^M \end{pmatrix} = \begin{pmatrix} C_{11}+C_{12}+C_{13} & -C_{12} & -C_{13} \\ -C_{12} & C_{12}+C_{22}+C_{23} & -C_{23} \\ -C_{13} & -C_{23} & C_{13}+C_{23}+C_{33} \end{pmatrix},$$

where C_{ij} is the capacitance between conductor i and j.
We define the elements of the chip as ideal conductors and not as superconductors, since there would be no differences in capacitance estimation. COMSOL is used to simulate the capacitances in Ch. 3 and Ch. 6.

Sonnet is an RF model software simulator for planar circuits [34, 52]. As in COMSOL, Sonnet needs the physical properties of the whole structure to simulate the chip response, such as the effective relative electric permittivity. In Ch. 3 and in Ch. 6, Sonnet is used to simulate the transmission parameter S_{21} of the readout coplanar waveguide (CPW) resonator. In Sonnet it is possible to effectively take into account the kinetic inductance of superconductors introducing a surface inductance [34].

2.2 Fabrication

The fabrication processes of the chips presented in this thesis were carried out in different facilities. At the Institute of Photonic Sciences (ICFO), optical and electron beam lithography, as well as resist deposition and development, were performed in the Nanofabrication Laboratory (NFL) cleanroom. The metallization and lift-off processes have been carried out in the IFAE cleanroom, using a metal evaporator made available by Qilimanjaro Quantum Tech. In the following part of this section, we are presenting the different processes carried out in these facilities.
In general, qubit device fabrication can be divided in two main steps: the device patterning and the metal evaporation. The first step consists in shaping a polymer by either optical or electron beam lithography. In fact, since qubit designs contain structures with dimensions in $> 1\ \mu$m and in $< 1\ \mu$m ranges, different patterning processes are needed. For structures in the $> 1\ \mu$m dimension range, the chip patterning is carried out through a photolithography process, whereas structures below $1\ \mu$m dimension range are patterned through electron beam lithography (EBL).
The patterned chip is then covered by a metal layer deposited by evaporation, performed in a PLASSYS evaporator. Then, a lift-off process is realized, returning the chip with the metallic structures.
Generally, the device patterning and metal evaporation steps are repeated three times to fabricate the flux qubit devices used in this thesis. In the first iteration, the bigger structures (i.e. ground planes, resonators, capacitors, etc...) are patterned through photolithography and, for this reason, we are referring to this layer as "optical layer". Then, the sub-micron structures, such as the Josesphson junctions, are patterned with EBL. The last iteration is dedicated to the contact structures that connect the different metal layers. This step is fundamental to connect the microscopic structures with the sub-micron structures. Prior to depositing the contacts, an Ar milling stepis performed [53] to avoid spurious parasitic Josephson junctions at the contacts. The three patterns are aligned using different sets of alignment markers.
In the following sections, the different patterning techniques and the evaporation

processes are presented.

2.2.1 Optical lithography

In this thesis, photolithography processes have been realized employing a Maskless Aligner Heidelberg MLA150 (MLA) in the NFL cleanroom at ICFO. Using a 375 nm laser, the MLA is able to expose an arbitrary layout on a photoresist, eliminating the necessity of a mask fabrication, hence the name. Laser writers also operate without a mask, although the MLA is much faster. Moreover, the critical dimension of the employed MLA is 0.6 μm, which is smaller if compared to the typical resolution of laser writers of 1 μm.
The optical layer is exposed on a ≈ 2 μm-thick AZ nLOF 2020 negative resist. The adhesion is guaranteed by a prior TI prime adhesive deposition. Details on fabrication recipes can be found in App. A.
As a preliminary step for any kind of lithography, it is necessary to perform a dose test to find the best operation parameter to obtain structures with the designed dimensions. An example of dose test is presented in Fig. 2.2.

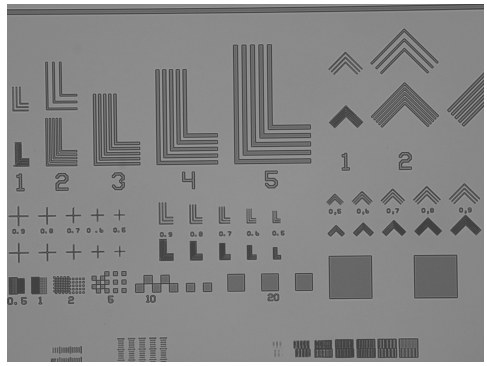

Figure 2.2: MLA dose test structures after Al evaporation.

It is important to note that AZ nLOF 2020 is developed by AZ 726 MIF. This developer etches aluminium, leading to possible degradation of any pre-existent structure. For this reason, an optical layer obtained with the process so far described cannot be patterned after the EBL layer evaporation and the contact layer deposition is necessary.
For this reason, AZ 5214E positive photoresist has been characterized for the contact layer. This resist is developed by AZ Developer, a chemical that does not affect aluminium and can be safely used on pre-existent structures.

2.2.2 Electron beam lithography

As explained in the preamble of this section, to pattern structures smaller than the MLA critical dimension, $< 0.6\,\mu$m, it is necessary to use electron beam lithography (EBL). The EBL used in this thesis is a CRESTEC CABL-AP50E/RD located at NFL cleanroom at ICFO. It is a 50 kV EBL, with 2 nm as the minimum beam diameter. In qubit device production, dose tests have been performed for two write fields: $600\,\mu$m, for large structures as the Josephson junctions leads, and $120\,\mu$m, for the smaller structures such as the Josephson junctions themselves.
In order to obtain well-defined borders of the nanostructures and avoid problems at the junctions due to the lift-off process, a double-resist stack is used, composed of a first layer of PMGI 630 nm-thick and a second layer of CSAR60 240 nm-thick. More details on the fabrication recipe can be found in App. A.
In Fig. 2.3, an example of Josephson junctions patterned with the described EBL process is shown.

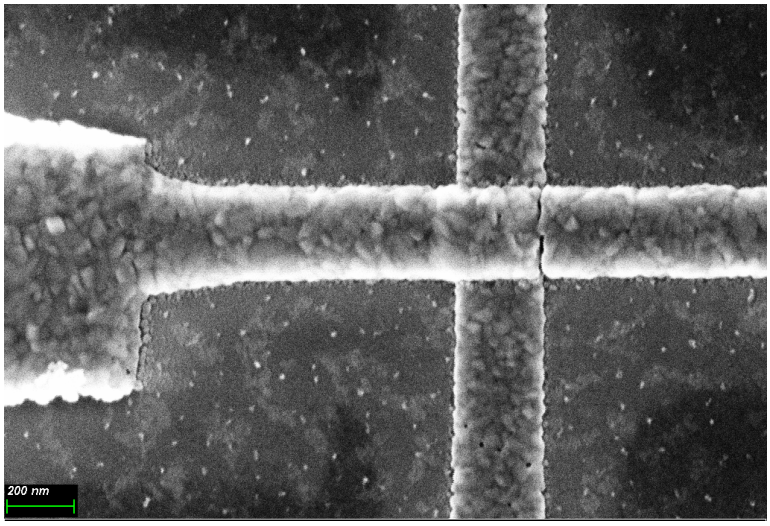

Figure 2.3: SEM image of a Josephson junction patterned with CRESTEC CABL-AP50E/RD to calibrate the oxidation step during the evaporation process.

2.2.3 Metal evaporation

Patterned devices are placed in a Plassys metal evaporator for the metallization process in our clean-room at IFAE. The evaporator, which is automated, is composed by two high-vacuum chambers: a loadlock and a process chamber. The loadlock is equipped with a microwave source, in order to perform surface descumming, and an Ar ionizing gun, to perform Ar milling [53].

The evaporation for the optical layer is performed vertically with no angle. In order to evaporate Josephson junctions in the Manhattan style [54], it is fundamental to characterize the angle evaporation, as well as the oxidation process. The structures in Fig. 2.3 are used to do such calibration.
The evaporation is followed by a lift-off process soaking the chip in 75°C N-Methyl-2-pyrrolidone (NMP), stirring at 200 r.p.m., for two hours. While the lift-off is taking place, an ionizer fan is used to eliminate static electricity, to avoid short-circuited junctions.
Once the device is completed, it is covered with a photoresist and diced at the Post-Processing laboratory (PPL) at ICFO. Then, the device is cleaned and is ready to be characterized.

2.3 Experimental setup

In this section, the experimental setup for qubit characterization at the QCT laboratory at IFAE is presented. In the first part, the sample packaging for the devices described in Ch. 3 and in Ch. 6 is presented. The dilution fridge used to perform all the measurements presented in this thesis is described in the last part of this section.

2.3.1 Sample packaging

Once a chip is fabricated, it is placed on a ceramic printed circuit board (PCB). The two experiments presented in this thesis are performed using two different PCBs: a 6-port PCB, designed by IFAE group, to carry out the measurements presented in Sec. 6.2, and a 12-port PCB, designed by the group of Prof. M. Weides at the University of Glasgow, used to obtain the results in Sec. 3.4. The PCB traces are connected to the chip through Al wirebonds. Each PCB trace is soldered to an SMA connector for the 6-port PCB in Fig. 2.4b, or to an SMP connector for the 12-port PCB in Fig. 2.4a. A thin layer of Apiezon N grease is spread under the chip to enhance the thermal connection between the PCB and the chip.
The PCB is then fixed to a sample box. In order to have good thermal connection and to permit measurements under a magnetic field, the sample boxes are made out of electrolytic Cu. The two sample boxes are designed with a mount for a superconducting coil on the top of the box to perform measurements at different values of the magnetic field.

2.3.2 Dilution fridge

To perform measurements with superconductors, cryogenic systems are needed to reach temperatures lower than the superconducting critical temperature T_c. Historic-

(a) (b)

Figure 2.4: (a) Design of the PCB used to obtain the results in Ch. 3. (b) Design of the PCB used to obtain the results in Ch. 6. In both PCBs, the blue part is the ceramic substrate, while the orange part is Cu. The small holes are internally metallized with Cu, in order to electrically connect the two sides of the PCB and establish a proper grounding, whereas the big holes are for fastening screws.

ally, temperatures below 1 K were reached with evaporation refrigerators, which are able to cool down to 300 mK. Nevertheless, temperatures in the order of few mK are desirable to reduce the effects of the thermal noise on the qubit. Thus, dry and wet dilution refrigerators started to be employed for qubit measurements, since they are able to reach temperatures below 20 mK. The difference between these two types of cooling system resides in the necessity for the wet refrigerators of a pre-cooling step based on liquid helium, whereas dry dilution refrigerators rely on a pulse tube helium compressor. Around 20 mK, the Johnson–Nyquist noise frequency is < 500MHz, thus qubits with higher transition frequencies are weakly affected by it. In this thesis, the measurements have been performed in a Bluefors dry dilution fridge at a base temperature of ~ 20 mK.

In Fig. 2.5, the schematic of the wiring inside the dilution refrigerator used to achieve the results presented in this thesis is shown. In a closed circuit, not represented in Fig. 2.5, a mixture of ^{4}He and ^{3}He is pumped in order to reach the mK regime. Pumping on ^{4}He, the system is cooled down to < 4 K, that is a necessary preliminary step. Then, the mixture of ^{4}He and ^{3}He is pumped to reach < 1 K. Thus, around 870 mK, the two phases separate in a ^{4}He-rich phase, which is called diluted phase, and a ^{3}He-rich phase, which is called concentrated phase. The equilibrium at the mK is ensured by the continuous exchange of ^{3}He between the two phases. This phase separation is achieved in the mixing chamber stage of the fridge (MXC in Fig. 2.5). The exchange of ^{3}He takes place between the MXC stage, in which the concentrated phase is present, and the still plate, where the majority of the diluted phase is present. The two stages are connected by heat exchangers that pre-cool the diluted phase.

The inside of the fridge is under 10^{-9} bar vacuum, in order to thermally isolate

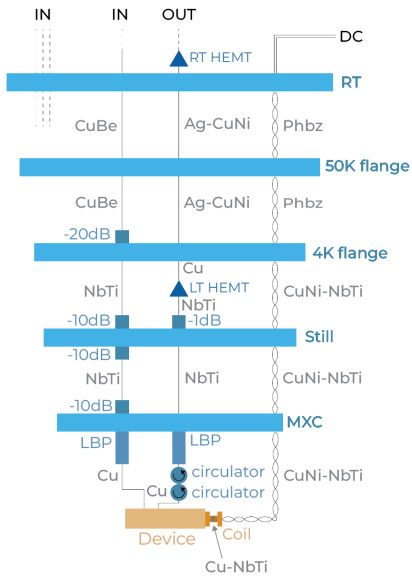

Figure 2.5: Dilution fridge scheme used to perform the measurements presented in this work [49].

the inner parts, including our devices, from the external environment. Moreover, three levels of magnetic shielding are placed around the sample box. A first Pb shield is anchored to the still stage, which both isolates the system from the external magnetic field and from some environmental radioactivity. The other two magnetic shields made of high magnetic permeability material are placed inside and outside the vacuum can shield, which is the outermost layer of the dilution refrigerator.
The sample box is thermally anchored to the MXC stage, since the MXC is the coolest stage of the cryostat. The sample is connected to the external environment through coaxial cables. Due to the different temperature stages, the cables are made of NbTi from the MXC to the 4 K stage and of CuBe from 4 K stage to room temperature stage (RT in Fig. 2.5), to let the lowest heat flow between the plates. The coaxial cables are divided in five input lines and one output line. The input cables pass through several passive attenuators, resulting in a total attenuation of -50 dB, without taking into account the losses due to the cables. The output line passes through a first amplification stage, where a low-temperature high-electron-mobility transistor (LT HEMT in Fig. 2.5) provides 40 dB of amplification. At room temperature, the signal is further amplified by two Pasternack RF amplifiers, each with ~ 17 dB of gain, and a RT HEMT, with ~ 44 dB of gain . All types of lines are filtered with low pass (LBP in Fig. 2.5) filters that eliminate noise with frequency

$>$ 8 GHz. The transmission of a single cable is presented in Fig. 2.6. The dip in the transmission around 6 GHz is due to a faulty connection.

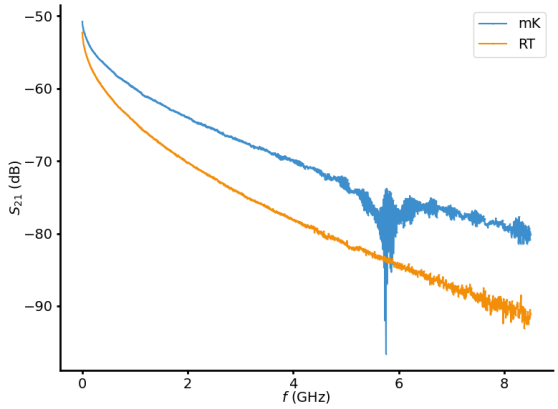

Figure 2.6: Cable transmission at room temperature (orange) and at mK regime (blue). This measurement was performed without amplification stages on an input line connected to the output one.

It is important to point out that circulators are located between the device output and the output lines. These elements avoid the backward injection of noise from the output lines, especially from amplifiers, but they impose a limitation on the setup bandwidth, since they work in the $4-8$ GHz range.
Finally, DC cables connect the MXC stage to RT, for $V-I$ characteristics measurements. Two of these lines are used to drive the superconducting coil, in order to generate a magnetic field on the sample. The coil cables are made of NbTi with CuNi cladding from MXC to 4 K and phosphor bronze from 4 K to RT.
More details on the dilution refrigerator setup can be found in [49].

2.4 Measurement techniques

In this section, several measurement techniques are presented, which will later be used in Ch. 3 and Ch. 6 to perform qubit measurements. The different methods are listed in same order as performed in the experiments. As the chip is finalized, the first step is to validate the quality of the fabrication through estimates of the Josephson junction critical currents at room temperature.
Once the device is cold, a first spectroscopy on the readout resonator is necessary to confirm the presence of qubits. Then, the qubit spectrum is measured, which allows to measure the dispersive shift of the resonator (see Sec. 3.4.2) and the qubit

coherence times (see Sec. 3.4.3 and Sec. 3.4.4).

2.4.1 Room temperature resistance measurements

The cooling down process of a dilution refrigerator lasts ~ 24 h, thus it is important to validate the chip quality at room temperature prior to cooling it down. Recalling the seminal work presented in [55], it is known that the critical current of a Josephson junction can be estimated through the Ambegaokar–Baratoff formula

$$I_c = \frac{\pi\Delta}{2eR_N}\,, \tag{2.1}$$

where Δ is superconducting gap of the material, e is the electron charge and R_N is the resistance of the junction in the normal state.
In order to probe the junctions with low enough current, the chip is placed in a manual probe station with a home-built current supply. To ensure the quality and safety of the measurements, the probe station is provided with a vibration isolating table while the chip is held on the probe station stage through vacuum suction.
Then, the probes are connected to a voltage meter through a circuit that biases junctions at 10 mV, which ensures low bias currents. In Fig. 2.7, a simplified diagram of the circuit is presented.

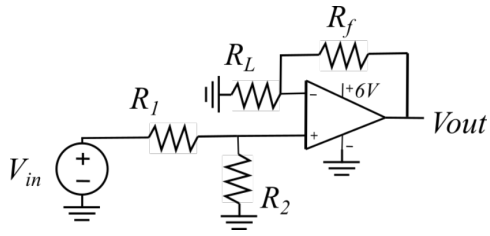

Figure 2.7: Simplified circuit diagram for Josephson junctions resistance measurements. R_L represents the Josephson junction.

In Fig. 2.7, R_L is the Josephson junction, R_f is the scale resistance (1 kΩ, 100 kΩ and 10 MΩ), $R_2 = 50\,\Omega$ and R_1 is a potentiometer to trim the bias voltage. The value of R_L is obtained from the circuit gain.

2.4.2 Frequency domain measurements

Once the system is cooled to the mK range, a first characterization is performed in frequency domain. To carry out this measurement, a vector network analyzer (VNA) is used. This instrument sends a continuous microwave signal and measures the transmitted and reflected signals at the same frequency, the S_{ij} parameters

[33]. The response of the system to a single tone gives information on the readout resonator transmission, which is fundamental to validate the qubit presence. This spectroscopy measurement is performed at low power, near the so-called single photon regime, to avoid higher order transitions in the qubit and resonator response. To reach this power level, a passive attenuation between 40 dB and 60 dB is placed at the output of the VNA.
Once the readout resonator spectroscopy is performed, the qubit spectrum is obtained through a two-tone spectroscopy. In this technique, an rf-tone is combined with the VNA tone through a splitter. While the VNA is probing the resonator frequency on resonance, the rf-tone is swept to excite the qubit. Variations in the resonator transmission returns information on the qubit spectrum when the rf tone matches the qubit frequency.
The VNA used in this thesis is an Agilent E5071B, with a range 300 kHz – 8.5 GHz, while the rf-source is a Rohde&Schwarz SGS100A SGMA, with a range 1 MHz – 12.75 GHz, even though the circuit bandwidth is limited to 8 GHz by the LBP filters and circulators.

2.4.3 Time-domain measurements

Once the qubit spectrum is obtained with the techniques presented in Sec. 2.4.2, it is possible to perform time-domain measurements. These measurements consist in probing the qubit with microwave pulses. For this reason, it is necessary to use an arbitrary waveform generator. In this thesis, the instruments used are two Keysight M3202A PXIe AWG mounted in a M9010A PXIe Chassis. More details on the time-domain measurements setup can be found in [49].
The first step to characterize the qubit is by measuring coherent Rabi oscillations. Without any external stimulus and $k_B T \ll \hbar\omega$, the qubit sits at its ground state. If a pulse at the qubit frequency is sent to the system, the qubit is brought to the excited state with a probability $P_e = 1 - P_g$, depending on the duration and amplitude of the pulse. Varying the amplitude of the pulse, P_e starts to oscillate according to the Rabi formula

$$P_e(A) = \frac{\Omega^2}{\Omega^2 + \Delta^2} \sin^2\left(\frac{\kappa d T A}{2\hbar}\right), \tag{2.2}$$

with Ω the Rabi frequency, $\Delta \equiv \omega_R - \omega_q$ the detuning between the resonator frequency ω_r and the qubit frequency ω_q, A the amplitude of the pulse, T the pulse period, κ the coupling, and d the qubit electric dipole. From this measurement, it is possible to define the π pulse amplitude as the one returning $P_e = 1$ on resonance, i.e. the amplitude that allows the qubit to fully pass from the ground to the excited state. An example of a Rabi oscillation measurement is presented in Fig. 2.8a.

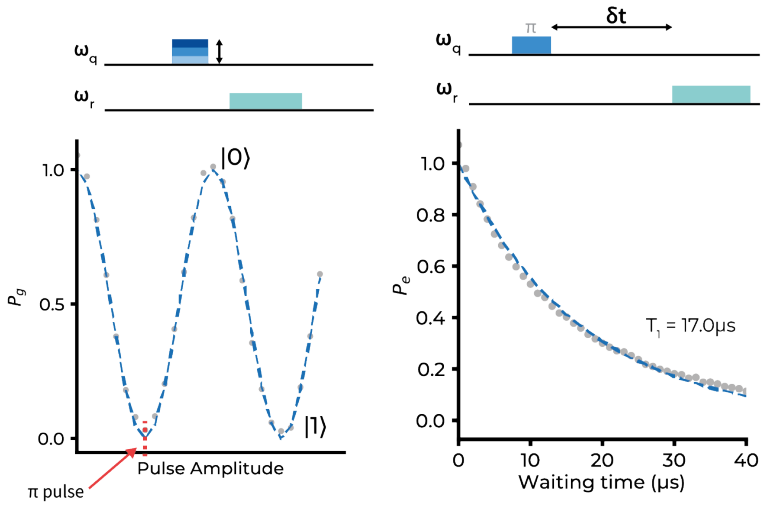

(a) (b)

Figure 2.8: (a) An example of a Rabi oscillation measurement, where the amplitude for a π pulse is indicated [49]. (b) Example of a T_1 measurement, with the π pulse defined through the Rabi oscillation measurement [49].

Once the qubit is excited to $|1\rangle$, the state population P_1 decays exponentially to $|0\rangle$, due to environmental noise. This process is described by the formula

$$P_1(t) = e^{-\Gamma_1 t} = e^{-t/T_1} \ , \tag{2.3}$$

where T_1 (Γ_1) is the energy relaxation time (rate).
T_1 is a fundamental benchmark for quantum computing [56], as any quantum algorithm has to run faster than the energy relaxation time of the qubit, or at least faster than the error correction schemes. A common technique to characterize T_1 consists of sending a π pulse to the qubit and, after a waiting time δt, probing the resonator with a readout pulse. T_1 is obtained by fitting the exponential decay of P_1 as function of δt, as depicted in Fig. 2.8b. Nevertheless, it is found that T_1 fluctuates over time, thus T_1 is to be estimated by the first moment of the histogram distribution of several measurements [56, 57]. Typical values of T_1 for flux qubits ranges from tens to hundreds of μs [44, 45, 46].
However, the environmental effect on the qubit can also be reflected in qubit frequency fluctuations, which are due to dephasing processes, i.e. loss of information on the qubit phase. Assuming an exponential decay, the dephasing decay or total decoherence is defined as

$$\Gamma_2 = \frac{\Gamma_1}{2} + \Gamma_\varphi \ , \tag{2.4}$$

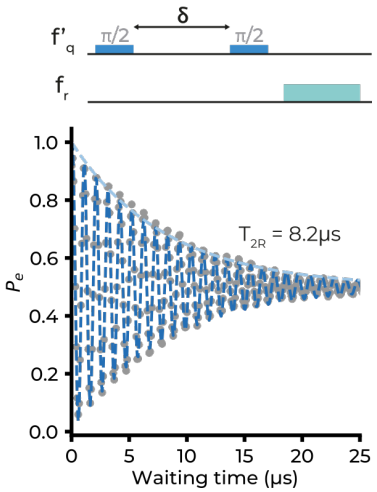

Figure 2.9: An example of a Ramsey measurement with the envelop fitted by an exponatial to obtain T_{2R} is highlighted [49].

where Γ_1 is the energy relaxation decay rate, since it also induces a loss in phase information, and Γ_φ is the pure dephasing decay rate. The corresponding time $T_2 = 1/\Gamma_2$ can be estimated by performing the so-called Ramsey measurement. This technique consists of sending two $\pi/2$ pulses separated by a variable waiting time δt and then probing the resonator with a readout pulse. For short waiting times, the state oscillates given that the $\pi/2$ pulses are slightly off-resonant. Nevertheless, as energy decay and dephasing processes become significant, the final state evolves into an incoherent superposition of the two qubit states. After sufficiently large δt, the qubit state is found to be with no phase information. An example of a Ramsey measurement is depicted in Fig. 2.9. T_{2R}, where the R stands for Ramsey, is estimated by fitting the envelop of the oscillations resulting from the measurement to an exponential. Once T_1 and T_{2R} are obtained, it is possible to measure the pure dephasing time T_φ with Eq. (2.4). Note that, in case of infinite pure dephasing time, T_{2R} is limited by $2T_1$. For flux qubits, typical values of T_{2R} range from $\sim 20\,\mu$s [44, 47] to values close to the the $2T_1$ limit [46], whereas T_φ ranges from few μs [47, 48] to $\sim 20\mu$s [46]. More details on the theory of time-domain measurements can be found in [49].

3

Single flux qubit physics

LUCA COZZOLINO, DAVID LÓPEZ-NÚÑEZ, FABIAN ZWIEHOFF, ELIA BERTOLDO, BARKAY GUTTEL, P. FORN-DÍAZ

In the remaining part of this thesis we will be focusing on flux qubits, already presented in Sec. 1.2.3. This type of qubits is characterized by a persistent current flowing around the loop, and the current direction is used as the qubit computational basis states. In this chapter, we analyse the first generation of flux qubit devices from the QCT group at IFAE, as part of the AVaQus project.
Following Sec. 1.3, the physics of a flux qubit capacitively coupled to a resonator is presented in Sec. 3.1. Using the theoretical derivation of the qubit Hamiltonian, a chip design is presented in Sec. 3.3. In Sec. 3.4, an overview of the fabrication process is presented, and finally the experimental results are discussed. The contents of this section were developed together as part of Dr. López-Núñez's Ph.D. thesis [49].

3.1 Flux qubit Hamiltonian

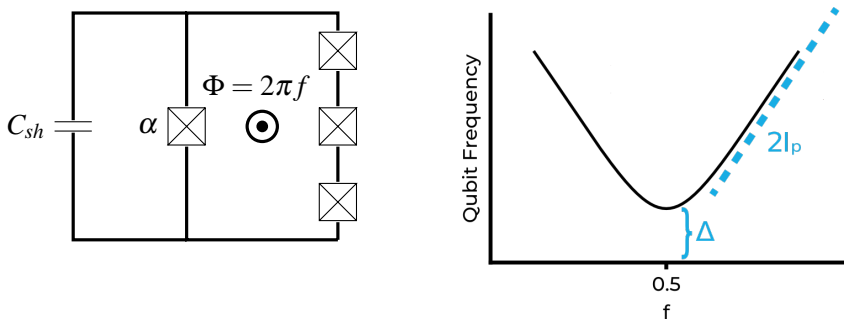

(a) (b)

Figure 3.1: a) A 4-Josephson junction shunted flux qubit circuit diagram. b) Qualitative representation of the spectrum of the qubit from a) [49].

As explained in Sec. 1.2.3, a flux qubit is generally a loop with at least an inductor and a Josephson junction. As a particular case, a persistent current (PC) qubit is formed by three [40] or more Josephson junctions [41] connected in a superconducting loop, one of which is α-times smaller than the other junctions, which are nominally identical. From now on, we are referring to PC qubit as the flux qubit. To enhance the flux qubit performance, in ref. [46] it was proposed to lower the critical current of all junction while keeping a high E_J/E_c ratio, combined with a shunt capacitance in parallel to the α junction. As the critical current is lowered, the qubit is less sensitive to flux noise, leading to better coherence times. On the other hand, adding a shunt capacitance leads to a smaller effect of the charge noise, since the charging energy E_c of the α junction diminishes and more energy is stored in a higher quality dielectric (Si) than the junction (AlO_x). Furthermore, the C_{sh} fabrication is more reliable, allowing a more stable prediction of the qubit transition frequency ω_q. In this section, a 4-Josephson Junction (4JJ) flux qubit is taken into account, with its circuit diagram is depicted in Fig. 3.1a. Following Sec. 1.3, this system is described by

$$\mathscr{H} = \frac{1}{2}\vec{q}^T\mathbf{M}^{-1}\vec{q} - E_J\left[\sum_{i=1}^{3}\cos(\varphi_i) + \alpha\cos\left(\sum_{i=1}^{3}\varphi_i - 2\pi f\right)\right], \tag{3.1}$$

where E_J is the Josephson energy of the big junction (see Sec. 1.1.1), $\varphi_n = 2\pi\phi_n/\Phi_0$ is the normalized n-th junction phase, $\vec{q}$ is the vector of variables conjugated to $\{\varphi_i\}$, $f = \Phi/\Phi_0$, and Φ is the external flux applied to the loop. In Eq. (3.1), the first term represents the kinetic energy term, while the term between

brackets represents the potential energy of the system. In the last cosine term, the fluxoid quantization is applied, i.e. $\varphi_\alpha = 2\pi f - \sum_i^3 \varphi_i$. When $f \to 0.5$, the potential becomes less sensitive to the external flux and, depending on α, the qubit potential can fall in different regimes, as shown in Fig. 3.2. It is clear that the position of the minimum of the potential energy depends on α.

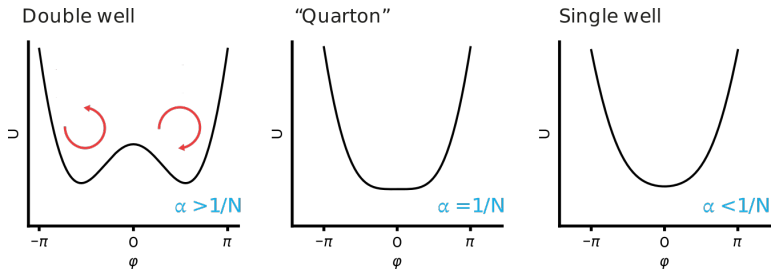

Figure 3.2: Flux qubit potential energy in the different α regimes at the sweetspot, $f = 0.5$. If $\alpha \leq 1/N$, the potential does not show the two local minima that defines the persistent current states [49].

Considering N as the number of the Josephson junctions, if $\alpha > 1/N$, the system is in the double-well regime, where the potential presents two local minima, as shown in Fig. 3.2. In fact, each local minimum defines a quantum state of the system, in which the persistent current through the loop flows clockwise or counter-clockwise, respectively. Due to tunneling across the barrier, both wells hybridize, leading to superpositions of current states as the eigenstates of the system. Thus, the qubit quantum state can be defined on the so-called current basis $\{|\circlearrowright\rangle, |\circlearrowleft\rangle\}$. At $f = 0.5$, the ground state $|g\rangle$ is an equal superposition of the PC states, which means that the average value of the persistent current is null. Furthermore, as the applied external flux moves away from $f = 0.5$, $|g\rangle \sim |\circlearrowright\rangle$, with $f > 0.5$ (or $\sim |\circlearrowleft\rangle$, for $f < 0.5$). For $f \ll 0.5$ (or $f \gg 0.5$), the system falls outside the double-well regime. The specific value of f for the different regimes depends on the persistent current I_p.
The first term of Eq. (3.1) is given by

$$\frac{1}{2}\vec{q}^T \mathbf{M}^{-1}\vec{q} = 4E_C \frac{1}{3\gamma+1}\left[(2\gamma+1)\left(n_1^2+n_2^2+n_3^2\right) - 2\gamma(n_1n_2+n_2n_3+n_3n_1)\right], \tag{3.2}$$

where $E_C = e^2/2C_J$ and $\gamma = (\alpha C_J + C_{sh})/C_J$, with C_J the capacitance of a big Josephson junction.
If the system is reduced to the computational subspace, i.e. it is described only by the first two PC states $\{|\circlearrowright\rangle, |\circlearrowleft\rangle\}$, the Hamiltonian in Eq. (3.1) can be reduced to

[9, 58]

$$\mathscr{H} = -\frac{\hbar\Delta}{2}\sigma_x - \frac{\hbar\varepsilon}{2}\sigma_z\,, \tag{3.3}$$

with the gap Δ as the qubit frequency at $f = 0.5$, and $\varepsilon = 2I_p(f - \frac{1}{2})\Phi_0$ as the magnetic energy bias. Let's point out that, for $f = 0.5$, the Hamiltonian is $\mathscr{H} = -\hbar\Delta\sigma_x/2$. In Fig. 3.1b, Δ and I_p are shown graphically.
If the system is rotated to the energy basis $\{|g\rangle, |e\rangle\}$, Eq. (3.3) reduces to

$$\mathscr{H} = -\frac{\hbar\omega_q}{2}\sigma_z\,, \tag{3.4}$$

where $\omega_q = \sqrt{\Delta^2 + \varepsilon^2}$ is the qubit frequency.
The system in Fig. 3.1a is the fundamental circuit of the work in this thesis. The first step is to study a system composed by a flux qubit capacitively coupled to a linear resonator acting as the qubit state detector, as it is the basic circuit used for quantum computing, analog and digital [46, 59], to characterize flux qubits.

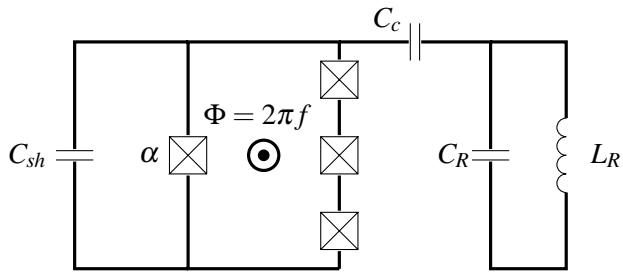

Figure 3.3: Flux qubit-resonator system

3.2 Flux qubit-resonator system

In this section, we analyze the physics of a 4JJ flux qubit capacitively coupled through C_c to a harmonic oscillator, as shown in Fig. 3.3. The system Hamiltonian can be written as [1]:

$$\mathscr{H}_{tot} = \mathscr{H}_q + \mathscr{H}_R + \mathscr{H}_C\,,$$

[1] The full derivation can be found in [49]. Nevertheless, here we report the main results described therein, with several corrections to the original work.

where

$$\begin{aligned}\mathscr{H}_q =& \frac{4E_C}{3}\left[\left(2+\frac{\gamma+\delta}{(\gamma+\delta)(1+3\alpha+3\sigma)+3\gamma\delta}\right)\sum_{i=1}^{3} n_i^2\right.\\ &\left.+\frac{1}{2}\left(-1+\frac{\gamma+\delta}{(\gamma+\delta)(1+3\alpha+3\sigma)+3\gamma\delta}\right)\sum_{i\neq j}^{3} n_i n_j\right]\\ &-E_J\left[\sum_{i=1}^{3}\cos\varphi_i+\alpha\cos\left(\sum_{i=1}^{3}\varphi_i-2\pi f\right)\right]=\\ =& 4E_C\left[\kappa_1\sum_{i=1}^{3} n_i^2+\frac{\kappa_2}{2}\sum_{i\neq j}^{3} n_i n_j\right]\\ &-E_J\left[\sum_{i=1}^{3}\cos\varphi_i+\alpha\cos\left(\sum_{i=1}^{3}\varphi_i-2\pi f\right)\right], \end{aligned} \tag{3.5}$$

$$\mathscr{H}_R = \hbar\omega_R\left(a^\dagger a+\frac{1}{2}\right), \tag{3.6}$$

$$\mathscr{H}_C = \kappa_C\sum_{i=1}^{3} n_i(a^\dagger - a), \tag{3.7}$$

with, following [60],

$$\begin{aligned}&\alpha=\frac{C_\alpha}{C_J}, \qquad \delta=\frac{C_R}{C_J},\\ &\gamma=\frac{C_C}{C_J}, \qquad \sigma=\frac{C_S}{C_J},\\ &\omega_R=\frac{1}{\sqrt{L_R C_R}}\left(\frac{\delta(1+3\alpha+3\gamma+3\sigma)}{(\gamma+\delta)(1+3\alpha+3\sigma)+3\gamma\delta}\right)^{1/2},\\ &E_R'=\hbar\omega_R,\\ &\kappa_C=2i\gamma\sqrt{E_C E_R'}\left\{\frac{1}{[(\gamma+\delta)(1+3\alpha+3\sigma)+3\gamma\delta]\,[3\alpha+3\gamma+3\sigma+1]}\right\}^{1/2},\end{aligned}$$

where the correct forms of ω_R and κ_C, with respect to ref. [49], are given.
The qubit and the resonator Hamiltonians define two Hilbert subspaces, such that a general quantum state of the circuit can be written as $|\Psi\rangle=\sum_{i,n} c_{in}|i,n\rangle$, where $|i\rangle$ is an eigenvector of $\mathscr{H}_q$, while $|n\rangle$ is an eigenvector of $\mathscr{H}_R$. The total Hamiltonian, omitting the hat symbol on the operators, can be written as

$$\mathscr{H}/\hbar = \omega_R\left(a^\dagger a+\frac{1}{2}\right)+\sum_i \omega_i|i\rangle\langle i|+\sum_{i,j} g_{ij}|i\rangle\langle j|\left(a^\dagger-a\right)=\mathscr{H}_0+V, \tag{3.8}$$

where $\hbar\omega_i$ is the qubit energy of state $|i\rangle$ and the coupling coefficient g_{ij} is given by

$$g_{ij} = \langle i| \kappa_C (n_1 + n_2 + n_3) |j\rangle \ . \tag{3.9}$$

This coupling represents the dipolar electric interaction between qubit and resonator and depends on the qubit electric dipole moment [61].
From Eq. (3.8), it is clear that $\mathscr{H}_C$ is a non-diagonal Hamiltonian. Whenever $|g| \ll |\omega_q - \omega_R|$, a perturbative approximation is possible, which reduces the total Hamiltonian to a diagonal Hamiltonian, known as the dispersive Hamiltonian. This perturbative regime is conventionally used when the resonator acts to read out the qubit state in cQED [42, 46]. More details on the derivation of Eqs. (3.1) and (3.8) can be found in [49], even though ω_R and κ_C are here corrected.

3.2.1 Dispersive regime

Usually, the readout process of a qubit is performed when the resonator and the qubit frequencies are well separated, i.e. when the system is in the dispersive regime, $|g| \ll |\omega_q - \omega_R|$. In this regime, it is possible to perform a perturbative approximation of the Hamiltonian in Eq. (3.8) around the parameter $\lambda = g/\Delta$, where $g = g_{01}$, as defined in Eq. (3.9), and $\delta \equiv \omega_q - \omega_R$ [43]. A possible method to achieve the dispersive Hamiltonian is to apply the so-called Schrieffer-Wolff (SW) transformation, which rotates the Hamiltonian to a diagonal form. The whole derivation is presented in App. B and the results are here presented.
The resulting transformed Hamiltonian is

$$\mathscr{H}' = \left(\omega_R - \sum_i \chi_i |i\rangle \langle i| \right) a^\dagger a + \sum_i \frac{\omega_i - \chi_i}{2} |i\rangle \langle i| \tag{3.10}$$

where

$$\chi_i = \sum_j (k_{ij} - k_{ji}) \ , \tag{3.11}$$
$$k_{ij} = \frac{|g_{ij}|^2}{\omega_r - (\omega_j - \omega_i)} \ .$$

Equation (3.10) describes how the resonator frequency is shifted by $\sum_i \chi_i$ due to the qubit energy levels. Note that the dispersive contribution from the counter-rotating terms is also included with the terms where $\omega_j < \omega_i$. Considering the computational basis of the qubit, i.e. $\{|g\rangle, |e\rangle\}$, Eq. (3.8) reduces to

$$\mathscr{H} = \omega_R a^\dagger a - \frac{\omega_q}{2}\sigma_z - ig\left(a^\dagger - a\right)\sigma_y = \tag{3.12}$$

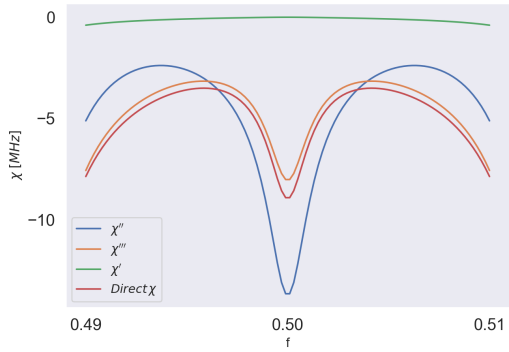

Figure 3.4: The dispersive shift of the readout resonator (in red) is simulated with different approximations of χ. χ' (in green) is the dispersive shift if only the qubit states of computational basis $\{g,e\}$ are considered. χ'' (in blue) is the approximation to the first three qubit energy levels and χ''' (in orange) is the approximation to the first four qubit energy levels. This simulation is performed with the parameters of qubit #0 in Table 3.2 and Table 3.1.

where $g_{eg} = i|g| = -g_{ge}$, $\omega_q = \omega_e - \omega_g$ and $[\sigma_+, \sigma_-] = \sigma_z$. Eq. (3.12) is the quantum Rabi model (QRM) Hamiltonian. Applying the rotating wave approximation (RWA), i.e. neglecting counter-rotating terms (rotating with $\omega_R + \omega_Q$), Eq. (3.13) is obtained [35, 62]

$$\mathscr{H}^{(RWA)} = \omega_R a^\dagger a - \frac{\omega_q}{2}\sigma_z - ig\left(a^\dagger \sigma_- + a\sigma_+\right) . \tag{3.13}$$

In this two-state basis, in the dispersive regime ,the dispersive shift reduces to

$$\chi' = k_{eg} - k_{ge} = |g|^2 \frac{2\omega_R}{\omega_R^2 - \omega_q^2} . \tag{3.14}$$

Equation (3.14) is not a good approximation of the effective dispersive shift, since the contribution of the higher levels of the qubit is in general not negligible. In Fig. 3.4, Eq. (3.14) is represented by the green curve χ'. If compared to the effective dispersive shift, calculated directly as $2\chi = (E_{|e,1\rangle} - E_{|e,0\rangle}) - (E_{|g,1\rangle} - E_{|g,0\rangle})$ (red line in Fig. 3.4), Eq. (3.14) returns an underestimation of the effect of the qubit on the resonator frequency. However, by considering more qubit energy levels in Eq. (3.11), χ converges to the effective dispersive shift. In Fig. 3.4, χ'' and χ''' are calculated taking into account three and four qubit energy levels, respectively. The peak at $f = 0.5$, despite being the point were $\omega_q - \omega_R$ is maximum, is due to a maximum of the qubit's electric dipole [61].

3.3 Chip design

In this section, we describe the device layout used to carry out the characterization of our first generation of flux qubits.

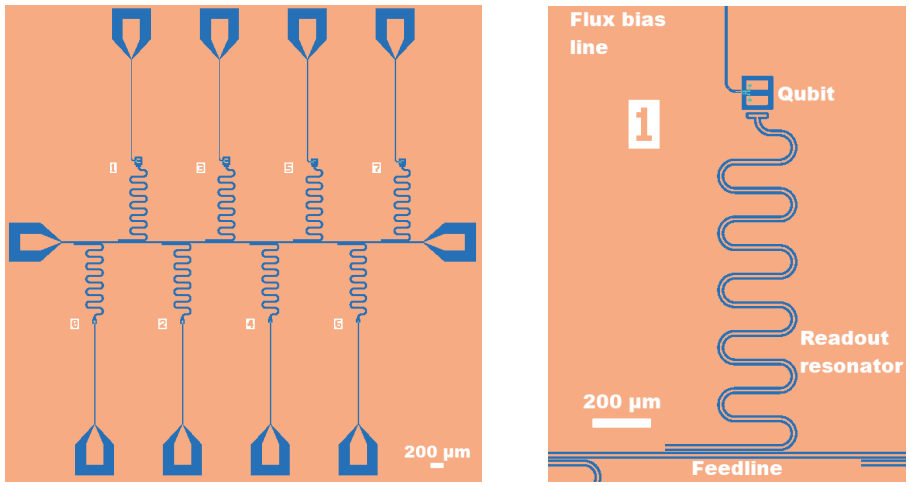

(a) (b)

Figure 3.5: a) Chip design of multiple single flux qubits, numbered $0-7$. b) Zoom in on a single qubit with its CPW resonator and the global feedline [49].

In order to measure qubits as the one depicted in Fig. 3.3, the chip in Fig. 3.5a was used. This device is composed by 8 single flux qubits, each qubit coupled to a dedicated coplanar waveguide resonator and a flux bias line (FBL), as shown in Fig. 3.5b. In the following, the qubit and CPW resonator designs are presented and discussed in Sec. 3.3.1 and Sec. 3.3.2, respectively.

3.3.1 Readout resonator design

Since we require a strong capacitive coupling between the qubit and the CPW resonator, a quarter wave ($\lambda/4$) resonator is used [34]. This kind of CPW resonator is characterized by having a shorted end, which we inductively couple to the feedline, and an open end, capacitively coupled to the qubit. Since the first resonance mode is at quarter wavelength, the electric field has a maximum on the open end [33]. Therefore, the resonator end close to the qubit is designed as a capacitor pad to enhance the coupling capacitance. The designed CPW resonator is presented in Fig. 3.5b.

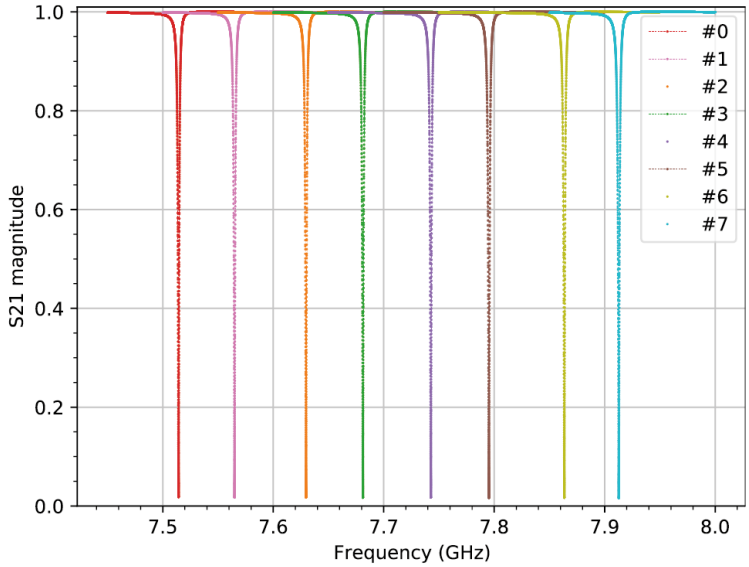

Figure 3.6: Sonnet simulation of the transmission of the designed CPW resonators on the device shown in Fig. 3.5a [49].

Following from [33], the bare frequency of a $\lambda/4$ CPW resonator is defined as

$$f_{\lambda/4} = \frac{c}{\sqrt{\varepsilon_{eff}}} \frac{1}{4l}, \tag{3.15}$$

with $l = \lambda/4$ being the resonator length, $\varepsilon_{eff} = 1/2\,(\varepsilon_1 + \varepsilon_2) \approx 6.255$, with ε_1 and ε_2 the relative dielectric permittivities of air and Si, respectively. As explained in Sec. 2.1, the resonators are simulated with Sonnet software. The simulated transmission of the complete resonator set is presented in Fig. 3.6. The resonances in Fig. 3.6 are designed to be sufficiently separated, i.e. to avoid crosstalk between measurements, given the bandwidth of each resonator and the acquisition electronics. A comprehensive summary of the design parameters is presented in Table 3.1.

3.3.2 Qubit design

The qubits in the device in Fig. 3.5a are divided in four groups of two qubits. Four qubits are designed with a lower frequency at the symmetry point than the other four. Moreover, these two groups are divided into “floating” flux qubits and “grounded” flux qubits, which differ in design. In Fig. 3.7a, a floating flux qubit is depicted, in which the qubit shunt capacitor plates are not referenced to ground. On the other hand, in the grounded flux qubit design, the shunt capacitance is defined between a

#	Length (mm)	f_0 (GHz)	$f_{\lambda/4}$ (GHz)
0	3.835	7.762	7.514
1	3.804	7.824	7.565
2	3.774	7.886	7.630
3	3.745	7.948	7.681
4	3.716	8.010	7.743
5	3.688	8.072	7.795
6	3.659	8.134	7.863
7	3.632	8.196	7.913

Table 3.1: Design parameters of the 8 resonators on device in Fig. 3.5a. $f_{\lambda/4}$ is the theoretical bare resonance, f_0 is the simulated one [49].

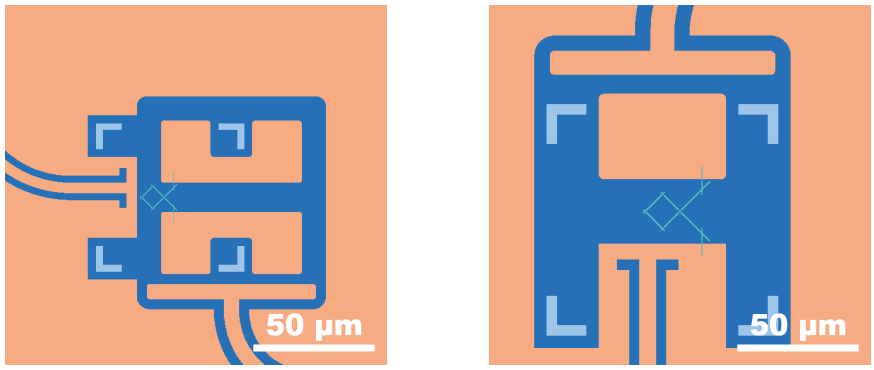

(a) (b)

Figure 3.7: a) Design of a floating flux qubit. b) Design of a grounded flux qubit [49].

reference plate and the ground plane, as shown in Fig. 3.7b.
Although the physical shunt capacitance is the one connected to the α junction, the effective shunt and coupling capacitance, as defined in Sec. 3.2, must be extracted by analyzing the entire capacitance network of the circuit. The optimal parameters are obtained through COMSOL simulations (see Sec. 2.1). A more detailed treatment of the capacitive network analysis is presented in Sec. 6.1.4 for a device involving a flux qubit and a dc-SQUID resonator.
The qubit loops are designed with an area of 81 μm^2, while the the big Josephson junction are designed with $I_c = 109$ nA. The small junctions are designed with $\alpha = 0.55 > 0.33$ (therefore in the double-well regime), with $I_p \approx 41$ nA.
In Table 3.2, the main design qubit parameters are presented.

#	Δ (GHz)	C_{sh} (pF)	C_c (pF)	Type
0	2.2	8.7	4.4	Grounded
1	2.2	8.6	2.9	Floating
2	2.2	8.7	4.4	Grounded
3	2.2	8.6	2.9	Floating
4	1.2	12.9	4.0	Grounded
5	1.2	12.5	2.4	Floating
6	1.2	12.9	4.0	Grounded
7	1.2	12.5	2.4	Floating

Table 3.2: Qubit design parameters, where Δ is the qubit frequency at the symmetry point [49].

3.4 Device characterization

In the following subsections, the experimental results obtained with the chip designed in Sec. 3.3 are presented.
The chip is fabricated on a high-intrinsic Si substrate 500 μm thick. The optical layer pattern was exposed by photolithography, with a Heidelberg MLA150 on negative resist, and later Al was deposited with a Plassys evaporator. More details on this fabrication process are given in Sec. 2.2. In Fig. 3.8a, the detail of a fabricated resonator #2 with its qubit is shown.

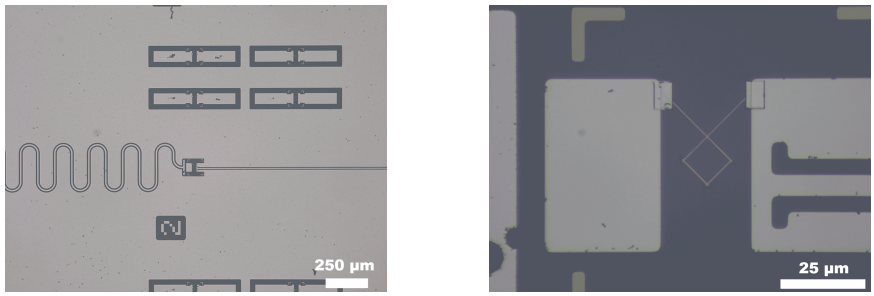

(a) (b)

Figure 3.8: Optical images of resonator #2, (a), and its coupled grounded flux qubit, (b), [49].

The qubit loop patterning and deposition is carried out by the Royal Holloway University of London (RHUL). The Josephson junctions are patterned with Manhattan style [54, 63] using two different evaporation angles. The contacts between the capacitor plates and the qubit loop are guaranteed by evaporating patches, which

are deposited with a standard perpendicular evaporation in a final step. In Fig. 3.8b, the optical image of a grounded qubit is presented.

The sample is placed in a 12-port Cu box. The feedline and the FBLs are connected through SMP connectors to the available fast fridge lines. A superconducting coil is mounted on the box lid in order to generate a magnetic field to the chip. The coil is connected with low resistivity DC lines to a floating current/voltage source. The coil bias is filtered interposing a π-filter between the voltage source and the DC lines. In Fig. 3.9, the sample box with the superconducting coil mounted below the mixing chamber is presented. More details on the setup are given in Sec. 2.3. In the next subsection, the results of the measurements performed with the 8-resonator chip are presented.

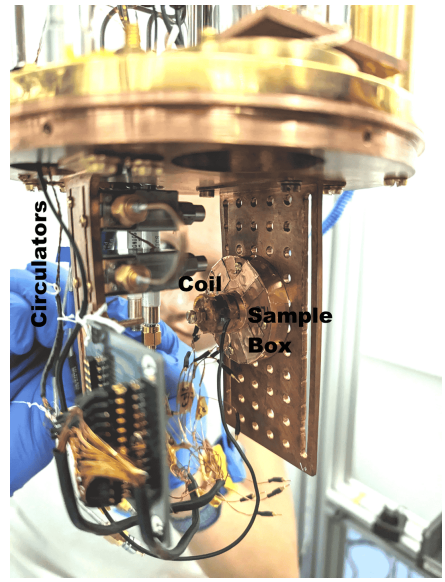

Figure 3.9: The Cu sample box with coil mounted in the fridge mixing chamber stage.

3.4.1 Spectroscopy measurements

The first step in qubit characterization is through resonator spectroscopy. A wide frequency scan performed with a VNA identifies all resonators. This way, the transmission of each resonator is monitored as the applied magnetic field changes, until a so-called avoided level-crossing appears in each resonator. Such an avoided level-crossing is a point where the qubit has the same frequency as the resonator. An example is shown in Fig. 3.10, where two consecutive avoided-level crossings can be seen. Hence, the qubit frequency is below the resonator frequency within the two avoided-level crossings.

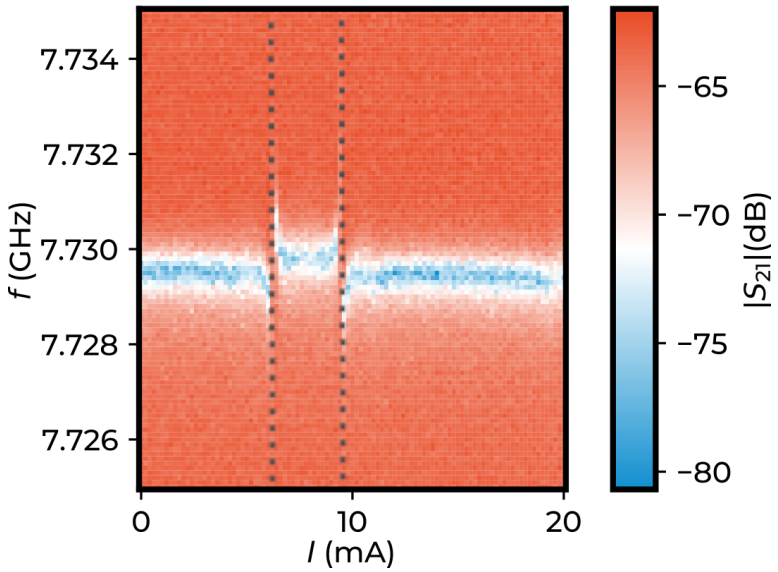

Figure 3.10: Avoided-level crossings detected through resonator spectroscopy [49]. The expected qubit frequency is represented by the dotted lines.

In a second characterization step, two-tone spectroscopy is performed to obtain the spectrum from each qubit. The resulting measurement of a specific floating qubit can be seen in Fig. 3.11, where the qubit transition frequencies are labelled. In fact, it is possible to observe not only the $|0\rangle \rightarrow |1\rangle$ transition but also higher-level transitions. It is interesting to point out the transition $\omega_{12}/2$, which implies a qubit initially in $|1\rangle$, possibly due to thermal population, as it is clear from the inverted shape of the transition with respect to ω_{01} and its positive phase signal. Unfortunately, the qubit frequency cannot be probed at the symmetry point, since its value $\Delta/2\pi \approx 250$ MHz is low enough so that the qubit is thermally populated and the readout cannot resolve the qubit states. Also, the linewidths are too broad to perform coherent dynamics, due to thermal and $1/f$ noise. This gap value is far off what was designed. This was observed in all qubits of this device. A probable explanation is that the ratios between the Josephson junctions, as well as the qubit persistent currents, were off-target due to uncontrolled parameters in the fabrication process. In fact, the persistent current is found to be higher than predicted ($I_p = 58.6$ nA vs. $I_p^{sim} = 41$ nA), as well as the ratio between the small and the big junction areas ($\alpha \approx 0.65$ vs. $\alpha_{des} = 0.55$), all leading to lower qubit gaps.

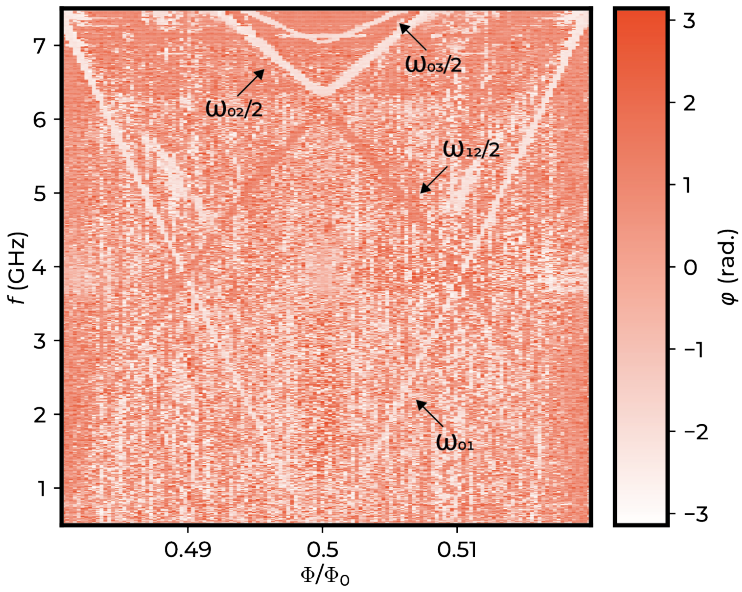

Figure 3.11: Qubit spectrum of a floating flux qubit. The qubit gap is $\Delta/2\pi \approx$ 250 MHz, while $I_p = 58.6$ nA, with $\alpha \approx 0.65$ [49].

3.4.2 Resonator dispersive shift

Once the qubit spectrum is identified, it is possible to quantify the dispersive shift of the resonator. Recalling Eq. (3.10), the dispersive shift is defined as

$$2\chi = (E_{|e,1\rangle} - E_{|e,0\rangle}) - (E_{|g,1\rangle} - E_{|g,0\rangle}) \,.$$

Hence, experimentally, 2χ is the difference in resonator frequency when the qubit is in the ground state and when it is in the excited state. Figure 3.12a presents the measurement to quantify of the dispersive shift, where the CPW resonance is measured with the qubit in the ground state and in the excited state. The latter measurement is obtained by combining the resonator spectroscopy with a tone resonant with the qubit frequency. The difference between the two resonance frequencies returns the dispersive shift χ.

Thus, since the dispersive shift depends on the qubit frequency, the same measurement is repeated for different values of the applied magnetic field. As suggested by Eq. (3.11), the dispersive shift decreases in magnitude as the qubit reaches the symmetry point, as it is observed in Fig. 3.12b, due to the increment of the detuning $\Delta \equiv \omega_r - \omega_q$. Nevertheless, we are expecting a peak in the dispersive shift at the sweet-spot (see Fig. 3.4), due to the dependence of the electric dipole coupling with

the qubit flux [61].
Due to the difficulty to clearly measure the frequencies near the symmetry point, no data have been collected in that range.

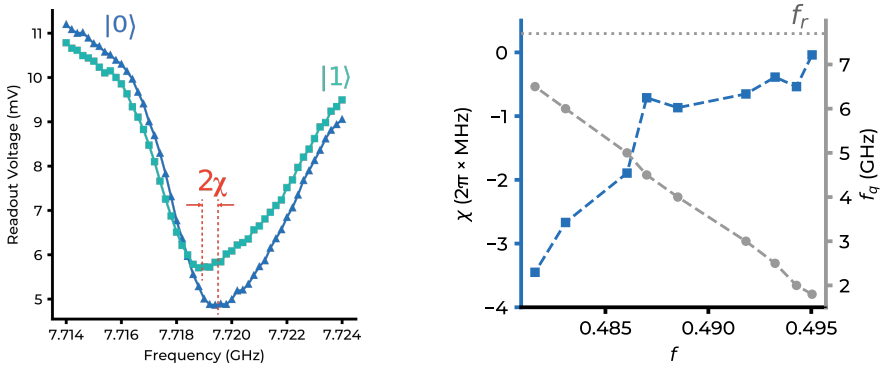

(a) (b)

Figure 3.12: a) Measurement procedure to obtain the dispersive shift at $f = 0.455$. b) Extracted values of χ between the avoided level crossing and the symmetry point [49].

3.4.3 T_1 relaxation time

Here, we present the T_1 energy relaxation time measurements with the spectrum shown in Fig. 3.11. The qubit is excited by a π pulse and, after a time delay δt, a readout pulse is sent to the resonator. As δt increases, the amplitude measured with the digitizer decreases, as shown in Fig. 3.13a. The signal level is already calibrated as qubit population.
In order to investigate how T_1 changes as a function of the applied external flux and taking into account its fluctuations [56, 57], each measurement is performed over 100 times and each repetition consist of a 5000 points average. Due to environmental microscopic fluctuations around the qubit, T_1 changes with time and the extrapolated T_1 values are sorted in histograms, which we fitted as Gaussians [57, 46]. In Fig. 3.13b, the expectation values of the fitted Gaussians are plotted together with the weighted average of the exponential fits as a function of the applied magnetic flux. Clearly, the discrepancies between the two curves are due to the number of repetitions of each measurement. With enough repetitions, the average should coincide with the mean of the Gaussian [64].

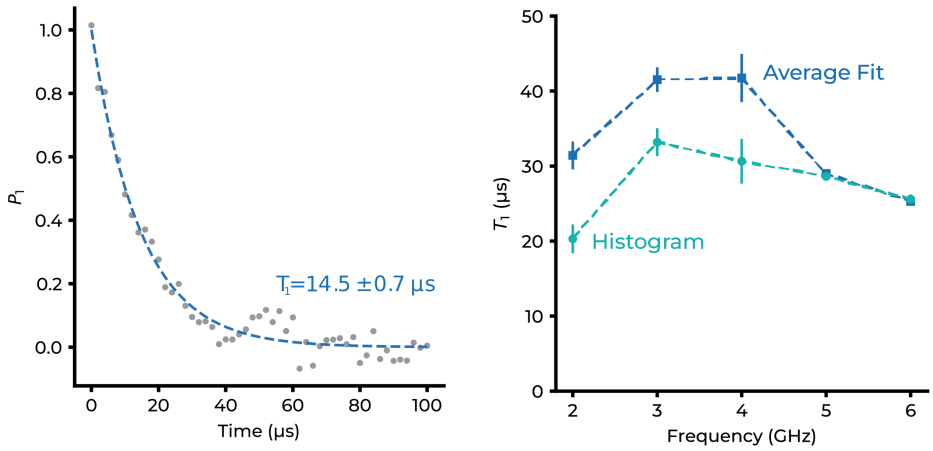

(a) (b)

Figure 3.13: a) Measurement procedure of T_1. b) T_1 behaviour as a function of the applied flux [49].

As the qubit frequency approaches the resonator, T_1 is dominated by the so-called Purcell effect [46], with a decay Γ_P (in the two-state qubit approximation) given by

$$\Gamma_P = \left(\frac{g}{\omega_R - \omega_q}\right)^2 \kappa = \frac{\chi'}{\omega_R - \omega_q}\kappa\,,$$

where κ is the resonator linewidth. With the measured values of χ and $\omega_R - \omega_q$, $T_{1,P} = 1/\Gamma_P \approx 28\ \mu$s, which is consistent with the measured T_1 at $f = 0.47$ in Fig. 3.13b.

As $f \to 0.5$, the qubit frequency enters the regime in which $\hbar\Delta \approx k_B T$ and thermally activated excitation and decay enhance the qubit decay rate. Furthermore, at the symmetry point, the electric dipole of the qubit is at its maximum value, which also maximizes the decay rate $\Gamma_1 = 1/T_1$.

Even though it is not possible to measure the coherence times at the symmetry point, which is the most reported in the literature of flux qubits, the obtained results are encouraging, as T_1 values are comparable with the typical ones for flux qubits [65, 46]. This is not surprising since, following [46], the flux noise scales as $\Gamma_1^\Phi \propto |\langle 1|\,\partial_\Phi \mathscr{H}\,|0\rangle|^2 \propto (\Delta/\omega_q)^2$. Assuming $\Delta/2\pi \approx 300$ MHz, we can extrapolate a value of T_1^Δ at $f = 0.5$ as

$$T_1^* = T_1^\Delta \left(\frac{\omega_q^*}{\Delta}\right) \approx 1.3\ \mu\text{s} \tag{3.16}$$

with $T_1^* = 25.6\ \mu$s and $\omega_q^*/2\pi = 6$ GHz estimated at $f = 0.47$. The result in Eq. (3.16) is far from the highest T_1 values reported, but it is in line with the results in ref. [46] with the state-of-the-art C-shunted flux qubits. Unfortunately, the qubit frequencies at the gaps resulted lower than the expected designed values, leading to difficulties to characterize the qubit at the symmetry point, which is otherwise the most interesting flux value.

3.4.4 T_2 dephasing time

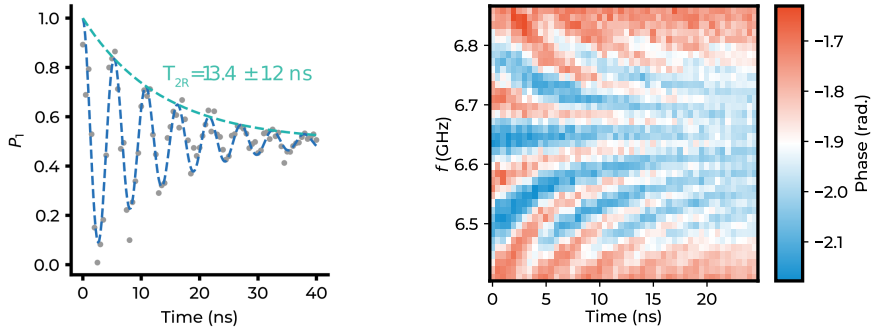

(a) (b)

Figure 3.14: a) T_{2R} measurement at $f_q = 6.4$ GHz. b) Ramsey fringes plot, i.e. Ramsey measurements, as the one in a), repeated varying the qubit pulse frequency [49].

As a last characterization step of the qubit, T_2 measurements are performed to measure dephasing rates. Recalling Eq. (2.4), T_1 and T_φ, both defined from exponential decays, the dephasing time T_2 is defined as

$$\frac{1}{T_2} = \frac{1}{2T_1} + \frac{1}{T_\varphi}\ . \tag{3.17}$$

In the qubit studied, qubit coherence could only be characterized far away from $f = 0.5$, but, due to high- and low-frequency flux noise, T_ϕ was strongly impaired. Even the $1/f$ noise still has a significant amplitude at 6 GHz [65].
Nevertheless, the Ramsey fringes measurement was performed to obtain information by the noise source, as shown in Fig. 3.14b. The actual qubit frequency f_q is found when no Ramsey oscillations are detected. From Ramsey measurements, the qubit linewidth is found to be ≈ 40 MHz at $f = 0.46$.
Very short pulses have been generated to obtain Fig. 3.14a, with a resulting $T_{2R} =$

13.4 ± 1.2 ns, which is low compared with literature values [44, 47, 48].
The main source of noise points to flux noise, although Ramsey fringes would have to be measured at the sweet spot to fully characterize the qubit noise sources. A second source of noise may come from the environmental electric noise in the laboratory, which at the time of performing the measurements had not been eliminated.

3.5 Outlook

In this chapter, the first generation of flux qubits was presented and discussed. The qubit design and its subsequent characterization was performed, with a particular emphasis on the time-domain measurements. Unfortunately, due to uncontrolled parameters in the fabrication process taking place in different cleanrooms, the measured value of qubit gap Δ and I_p were far from the designed values. In particular, Δ was designed to be in the range $1.2 - 2.2$ GHz, whereas the measured gaps are ≈ 250 MHz. Hence, measuring the specturm around the sweet spot proved challenging , due to the qubit large linewidth and thermal excitations between the first two qubit energy levels.
Moreover, I_p is $\approx 43\%$ higher than the designed value, making the qubit more sensitive to flux noise. Likely, this is one of the reason of the low T_{2R} measured and the reason for the low Δ.
Besides, the measurements in this chapter give indications to the production of a new generation of qubits with enhanced properties. It is clear that higher qubit gap frequencies, with lower I_p, would give us the opportunity to study the origin of the noise and to characterize the coherence times at the sweet spot. Moreover, the coupling between the qubit and the resonator needs to be enhanced, increasing the dispersive shift χ, leading to a larger signal.
Since the fabrication process is probably the cause of the deviation from the nominal values, a more controlled fully in-house fabrication process is necessary to obtain measured values close to the targeted ones.
For these reasons, we are working on a similar chip fabricated in a single-step exposition by the University of Glasgow. The chip design has been modified following the indications just presented. The new devices will be made of Nb instead of Al. Nb has a higher critical temperature, leading to a negligible contribution of quasiparticle noise. Moreover, Nb transmons have shown promising results on coherence time measurements [66], though there is still no published results of Nb-based flux qubits, except very primitive ones obtained at MIT in early 2000's [67].
The sample packaging can also be improved to obtain better coherence times as

well. The flip-chip architecture points to the right direction by physically separating control lines and readout circuitry from the qubit chip [68]. This approach should reduce crosstalk from the rest of elements on the chip, thereby increasing the qubit coherence and control.

4

Galvanic couplings in qubit circuits

In the previous chapter, the Hamiltonian of a qubit capacitively coupled to its readout resonator was treated within the dispersive regime. Their interaction led to an energy correction for both qubit and resonator Hamiltonians.
In this chapter, two galvanically coupled systems are studied. Here, the term "galvanically" is used to describe a coupling realized through a physical shared inductor between the coupled systems.
Sec. 4.1 contains the analysis of a qubit galvanically coupled to a resonator, while, in Sec. 4.2, a system of two galvanically coupled qubits is described.
The content of this chapter is preparatory for Ch. 5, where the concept of the persistent current readout is presented. The study of the two extremal cases of galvanic coupling, particularly a linear resonator and a strongly non-linear object, is useful to achieve a better comprehension of what is presented later in this thesis.

4.1 Qubit-resonator system

Flux qubits galvanically coupled to linear resonators have been widely used to study the physics of the interaction between an artificial atom and an electromagnetic field [69, 70, 71, 72]. Particularly, large linear inductors shared between the qubit and the resonator are used to reach a large coupling strength g, such as in the ultrastrong coupling regime, where $g/\omega_R > 0.1$ [62], ω_r being the resonator frequency.
First, let's point out that, different from Ch. 3, in this section a three-Josephson junction qubit is specifically taken into consideration. To be galvanically coupled, the qubit has to share an inductor, corresponding to a portion of its loop, with the

resonator [73, 62]. Such a system is depicted in Fig. 4.1. In the figure, the two systems are coupled through an inductor, namely L_c, and its branch variable, ϕ_4.

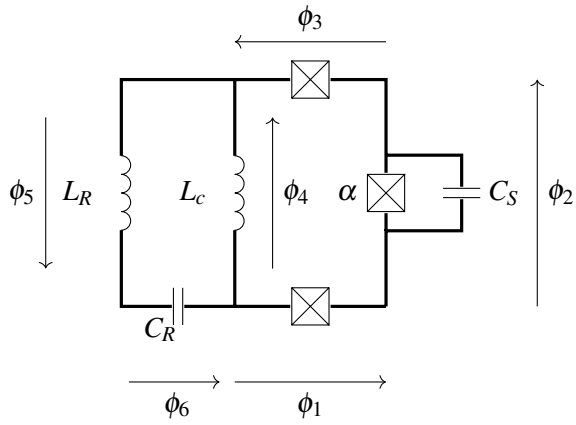

Figure 4.1: A three Josephson junction flux qubit galvanically coupled to a resonator.

Using the circuit tree defined in Fig. 4.1, the total Hamiltonian of the system can be written as follows:

$$\begin{aligned}\hat{\mathscr{H}} = &\left(\frac{2\pi}{\Phi_0}\right)^2 \frac{1}{2C_J}\left[(\hat{p}_1+\hat{p}_4)^2+\frac{1}{\gamma}(\hat{p}_3+\hat{p}_4)^2+\frac{C_J}{C_R}\hat{p}_6^2\right]+\\ &-E_J\cos(\hat{\varphi}_1)-E_J\cos(\hat{\varphi}_3)-\alpha E_J\cos(\hat{\varphi}_4-\hat{\varphi}_1-\hat{\varphi}_3+2\pi f)+\\ &+\frac{1}{2L_c}\left(\frac{\Phi_0}{2\pi}\right)^2\hat{\varphi}_4^2+\left(\frac{\Phi_0}{2\pi}\right)^2\frac{1}{2L_R}(\hat{\varphi}_6+\hat{\varphi}_4)^2\,,\end{aligned} \tag{4.1}$$

where $\varphi_i = 2\pi\phi_i/\Phi_0$, C_J is the capacitance of the big Josephson junctions, L_c is the shared coupling inductance, L_R and C_R are the resonator inductance and capacitance, respectively, $\alpha = I_\alpha/I$ with I_α (I) is the critical current of the small (big) Josephson junction, $\gamma = \alpha + C_S/C_J$ and $2\pi f = \Phi_0$ is the external magnetic field. The inductor L_c form a high-frequency oscillator mode of frequency

$$\omega = \frac{1}{\sqrt{\alpha C_J L_c}}\,,$$

which can be considered in its ground state.
Therefore the inductor variable $\hat{\varphi}_4$ adapts rapidly to the system variations and can be assumed to be in a quasi-steady state, $\langle \dot{\hat{\varphi}} \rangle = 0$, with respect to the rest of variables [74, 75, 73]. This choice allows us to neglect the kinetic energy terms related to coupling inductance (proportional to $\dot{\hat{\varphi}}_4$) in the Eq. (4.1) and rewrite the

Hamiltonian as:

$$\begin{aligned}\hat{\mathscr{H}}' \simeq & \left(\frac{2\pi}{\Phi_0}\right)^2 \frac{1}{2C_J}\left[\hat{p}_1^2 + \frac{1}{\gamma}\hat{p}_3^2 + \frac{C_J}{C_R}\hat{p}_6^2\right] - E_J\cos(\hat{\varphi}_1) \\ & - E_J\cos(\hat{\varphi}_3) - \alpha E_J\cos(\hat{\varphi}_4 - \hat{\varphi}_1 - \hat{\varphi}_3 + 2\pi f) \\ & + \frac{1}{2L_c}\left(\frac{\Phi_0}{2\pi}\right)^2 \hat{\varphi}_4^2 + \left(\frac{\Phi_0}{2\pi}\right)^2 \frac{1}{2L_R}(\hat{\varphi}_6 + \hat{\varphi}_4)^2 \ . \end{aligned} \tag{4.2}$$

Eq. (4.2) can be further simplified if we assume the variable $\hat{\varphi}_4$ to be small enough to expand the cosine terms around it. The most obvious implication of this assumptions is that the energy stored in the coupling inductor has to be much smaller than the energy stored in the resonator inductor, i.e. $L_c \ll L_R$.
The resulting Hamiltonian looks

$$\begin{aligned}\hat{\mathscr{H}}'' \simeq & \left(\frac{2\pi}{\Phi_0}\right)^2 \frac{1}{2C_J}\left[\hat{p}^2 + \frac{1}{\gamma}\hat{p}_3^2 + \frac{C_J}{C_R}\hat{p}_6^2\right] - E_J\cos(\hat{\varphi}_1) - \gamma E_J\cos(\hat{\varphi}_3) \\ & - \alpha E_J\cos(-\hat{\varphi}_1 - \hat{\varphi}_3 + 2\pi f) - \alpha\hat{\varphi}_4 E_J\sin(-\hat{\varphi}_1 - \hat{\varphi}_3 + 2\pi f) \\ & + \frac{1}{2L_c}\left(\frac{\Phi_0}{2\pi}\right)^2 \hat{\varphi}_4^2 + \frac{1}{2L_R}(\hat{\varphi}_6 + \hat{\varphi}_4)^2 \ . \end{aligned} \tag{4.3}$$

The Taylor expansion of the cosine has been stopped at the second order in $\hat{\varphi}_4$.
In Eq. (4.3), the Hamiltonian can be divided into three terms: a qubit, a resonator and a interaction Hamiltonian

$$\begin{aligned}\hat{\mathscr{H}}''_{q'} = & \left(\frac{2\pi}{\Phi_0}\right)^2 \frac{1}{2C_J}\left[\hat{p}^2 + \frac{1}{\gamma}\hat{p}_3^2\right] \\ & - E_J\left[\cos(\hat{\varphi}_1) + \cos(\hat{\varphi}_3) + \alpha\cos(-\hat{\varphi}_1 - \hat{\varphi}_3 + 2\pi f)\right] \ , \end{aligned} \tag{4.4}$$

$$\hat{\mathscr{H}}''_R = \left(\frac{2\pi}{\Phi_0}\right)^2 \frac{1}{2C_R}\hat{p}_6^2 + \frac{1}{2L_R}\left(\frac{\Phi_0}{2\pi}\right)^2 \hat{\varphi}_6^2 \ , \tag{4.5}$$

$$\hat{\mathscr{H}}''_{int} = -\alpha\hat{\varphi}_4 E_J\sin(-\hat{\varphi}_1 - \hat{\varphi}_3 + 2\pi f) + \left(\frac{\Phi_0}{2\pi}\right)^2 \left[\frac{L_R + L_c}{L_c L_R}\frac{\hat{\varphi}_4^2}{2} + \frac{1}{L_R}\hat{\varphi}_6\hat{\varphi}_4\right] . \tag{4.6}$$

As pointed out in [75], since we assumed that $\hat{\varphi}_4$ is in a quasi-steady state in comparison with the other variables of the system, it is convenient to assume the potential defined in Eq. (4.6) to be in its minimum with respect to the coupling

inductance variable $\hat{\varphi}_4$. In other words,

$$\begin{aligned}
&\partial_{\varphi_4}\mathscr{H}''_{int}\big|_{\varphi_4^*} = 0\,,\\
&\left(\frac{\Phi_0}{2\pi}\right)^2\frac{L_R+L_c}{L_cL_R}\varphi_4^* + \left(\frac{\Phi_0}{2\pi}\right)^2\frac{1}{L_R}\varphi_6 - \alpha E_J\sin(-\varphi_1-\varphi_3+2\pi f) = 0\,,\\
&\Rightarrow \varphi_4^* = \left(\frac{2\pi}{\Phi_0}\right)^2\frac{L_RL_c}{L_c+L_R}\alpha E_J\sin(-\varphi_1-\varphi_3+2\pi f) - \frac{L_c}{L_c+L_R}\varphi_6\,. \qquad (4.7)
\end{aligned}$$

This approach is known as the Born-Oppenheimer approximation [75, 74, 76, 73]. As a consequence of the quasi-steady nature of $\hat{\varphi}_4$, it can now be substituted by $\hat{\varphi}_4^*$[1] in Eq. (4.6):

$$\begin{aligned}
\hat{\mathscr{H}}^*_{int} = &-\frac{1}{2}\left(\frac{2\pi}{\Phi_0}\right)^2\frac{L_RL_c}{L_c+L_R}\alpha^2E_J^2\sin^2(-\hat{\varphi}_1-\hat{\varphi}_3+2\pi f)+\\
&-\frac{L_c}{L_c+L_R}\frac{\hat{\varphi}_6^2}{2L_R} + \alpha\hat{\varphi}_6E_J\sin(-\hat{\varphi}_1-\hat{\varphi}_3+2\pi f)\,. \qquad (4.8)
\end{aligned}$$

Recalling what has been said in Ch. 1 and Ch. 3, the Josephson terms can be rewritten in terms of the current operator, $\hat{I}_p = (2\pi/\Phi_0)\alpha E_J\sin(-\hat{\varphi}_1-\hat{\varphi}_3+2\pi f)$

$$\hat{\mathscr{H}}^*_{int} = -\frac{1}{2}\frac{L_RL_c}{L_c+L_R}\hat{I}_p^2 - \left(\frac{\Phi_0}{2\pi}\right)^2\frac{L_c}{L_c+L_R}\frac{\hat{\varphi}_6^2}{2L_R} + \frac{\Phi_0}{2\pi}\hat{\varphi}_6\hat{I}_p\,. \qquad (4.9)$$

Equation (4.8) can be now separated into a term $\propto \hat{I}_p^2$, which renormalizes the qubit, a term $\propto \hat{\varphi}_6^2$, which renormalizes the resonator inductance energy, and a coupling term.

To further simplify Eq. (4.9), we introduce the creation and annihilation operators for the resonator degree of freedom. In this way, the resonator Hamiltonian defined in Eq. (4.6) can be reduced to the usual form of a quantized harmonic oscillator:

$$\begin{cases}
\hat{p}_6 = i\frac{\Phi_0}{2\pi}\sqrt{\frac{\hbar\omega C_R}{2}}\left(\hat{a}^\dagger-\hat{a}\right)\\
\hat{\varphi}_6 = \frac{2\pi}{\Phi_0}\sqrt{\frac{\hbar}{2\omega C_R}}\left(\hat{a}^\dagger+\hat{a}\right)
\end{cases} \qquad (4.10)$$

with $\omega^2 = \frac{1}{L_{tot}C_R}$, where $L_{tot} = L_R + L_c$.

Moreover, let's point out that the momentum operator $\hat{p}_6$ is related to the charge operator $\hat{Q}$ through the following expression

$$\hat{Q} = \frac{2\pi}{\Phi_0}\hat{p}_6\,.$$

[1] $\hat{\varphi}_4^*$ is the operator form of the scalar φ_4^* defined in Eq. (4.7)

This relation allows us to define the root mean square current operator as

$$\hat{I}_r = \frac{\partial \hat{Q}}{\partial t} = \frac{2\pi}{\Phi_0}\frac{\partial \hat{p}_6}{\partial t} = \sqrt{\frac{\hbar\omega}{2L_R}}(\hat{a}^\dagger + \hat{a}) = I_{rms}(\hat{a}^\dagger + \hat{a}) = \frac{1}{L_R}\frac{\Phi_0}{2\pi}\hat{\varphi}_6 \,, \tag{4.11}$$

with $I_{rms} = \sqrt{\frac{\hbar\omega}{2L_R}}$ and where, in the last step, $\hat{a}(t) = \hat{a}(0)e^{-i\omega t}$ and the following Hamiltonian relation have been used

$$\dot{\hat{p}}_6 = \frac{1}{L_R}\left(\frac{\Phi_0}{2\pi}\right)^2 \hat{\varphi}_6 \,.$$

Now, it is possible to redefine the whole interaction Hamiltonian in terms of current operators. In fact, substituting Eqs. (4.10) and (4.11) in Eq. (4.9), we obtain:

$$\hat{\mathscr{H}}_{int} = -\frac{1}{2}\frac{L_R L_c}{L_c + L_R}\hat{I}_p^2 - \frac{1}{2}\frac{L_c L_R}{L_c + L_R}\hat{I}_r^2 + \frac{L_c L_R}{L_c + L_R}\hat{I}_p\hat{I}_r \,. \tag{4.12}$$

Hence, recalling Eq. (4.6), the total Hamiltonian $\hat{\mathscr{H}}_{tot} = \hat{\mathscr{H}}_q + \hat{\mathscr{H}}_R + \hat{\mathscr{H}}_c$ can be written as [73]

$$\begin{aligned}\hat{\mathscr{H}}_q &= \left(\frac{2\pi}{\Phi_0}\right)^2 \frac{1}{2C_J}\left[\hat{p}^2 + \frac{1}{\gamma}\hat{p}_3^2\right] + \\ &\quad - E_J\left[\cos(\hat{\varphi}_1) + \cos(\hat{\varphi}_3) + \alpha\cos(-\hat{\varphi}_1 - \hat{\varphi}_3 + 2\pi f)\right] - \frac{1}{2}\frac{L_R L_c}{L_c + L_R}\hat{I}_p^2 \,,\end{aligned} \tag{4.13}$$

$$\hat{\mathscr{H}}_R = \frac{\hat{Q}^2}{2C_R} + \left(\frac{\Phi_0}{2\pi}\right)^2 \frac{\hat{\varphi}_6^2}{2L_R} - \frac{1}{2}\frac{L_c L_R}{L_c + L_R}\hat{I}_r^2 = \frac{\hat{Q}^2}{2C_R} + \left(\frac{\Phi_0}{2\pi}\right)^2 \frac{\hat{\varphi}_6^2}{2(L_R + L_c)} \,,$$

$$\hat{\mathscr{H}}_c = \frac{L_c L_R}{L_c + L_R}\hat{I}_p\hat{I}_{rms} \,. \tag{4.14}$$

Please note that, if $L_c \to 0$, the system Hamiltonian reduces to two separated Hamiltonians with no interaction. Such a situation would be as if the shared inductor would disappear, leaving the qubit and the resonator circuit isolated. Finally, the coupling Hamiltonian can be written with the usual quantum Rabi model notation [62][2]:

$$\hat{\mathscr{H}}_c = \hbar g(\hat{a}^\dagger + \hat{a})\sigma_z \,,$$

where the coupling strength g is defined as [73]

$$g \equiv \frac{L_c L_R}{\hbar(L_c + L_R)} I_p I_{rms} = \frac{L_{eff} I_p I_{rms}}{\hbar} \,, \tag{4.15}$$

[2]Here, the qubit Hamiltonian is written in the current basis.

which is the classical magnetic energy stored in the effective inductance $L_{eff} = L_c L_R / (L_c + L_R)$. Nevertheless, since we are imposing the case $L_R \gg L_c$, the effective inductance can be reduced to L_c and the coupling strength reduces to [73]

$$g = \frac{L_c I_p I_{rms}}{\hbar} ,$$

which is the semiclassical definition of the qubit-resonator coupling strength usually found in the literature [62, 77]. Therefore, we found that under the condition $L_c \ll L_R$, we can define the qubit-resonator coupling strength g in the classical approximation of the energy stored in an inductor L_c with current $I_p + I_{rms}$ passing through it

$$\mathscr{E} = \frac{1}{2} L_c (I_p + I_{rms})^2 = L_c I_p I_{rms} + \frac{1}{2} L_c I_p^2 + \frac{1}{2} L_c I_{rms}^2 . \tag{4.16}$$

4.2 Qubit-qubit system

While in the previous section the system was composed by a qubit and a linear resonator, now a qubit-qubit system coupled through a linear inductance is taken into account. This kind of system is interesting because it makes us consider a qubit coupled to a non-linear element. The circuit in Fig. 4.2 can be seen as one of the simplest ways to couple two qubits, nevertheless it is not very practical from the quantum computing point of view, since the coupling is fixed by a physical shared inductance L.

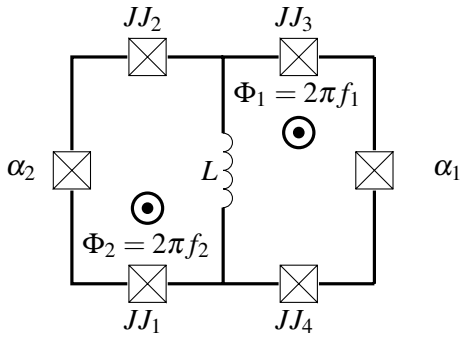

Figure 4.2: Circuit of two three-Josephson junction qubits galvanically coupled through a shared inductance L.

Figure 4.2 shows two three-Josephson junction flux qubits, each one with an applied external flux f_1, f_2, galvanically coupled through a shared inductance L.

The Hamiltonian of this system can be written as follows:

$$\begin{aligned}\hat{\mathscr{H}} = &\left(\frac{\Phi_0}{2\pi}\right)^2 \frac{C_J}{2}\left[\left(\frac{1}{2}+\alpha_1\right)\dot{\hat{\varphi}}_{L+}^2 + \left(\frac{1}{2}+\alpha_2\right)\dot{\hat{\varphi}}_{R+}^2 + \dot{\hat{\varphi}}_{L-}^2 + \dot{\hat{\varphi}}_{R-}^2\right] \\ &- E_J\left[2\cos\frac{\hat{\varphi}_{L+}}{2}\cos\frac{\hat{\varphi}_{L-}}{2} + 2\cos\frac{\hat{\varphi}_{R+}}{2}\cos\frac{\hat{\varphi}_{R-}}{2}\right. \\ &\left.+\alpha_1\cos(2\pi f_1 + \hat{\varphi}_L - \hat{\varphi}_{L+}) + \alpha_2\cos(2\pi f_2 - \hat{\varphi}_L - \hat{\varphi}_{R+})\right] \\ &+ \left(\frac{\Phi_0}{2\pi}\right)^2 \frac{C_J}{2}\left[(\alpha_1+\alpha_2)\dot{\hat{\varphi}}_L^2 + 2\dot{\hat{\varphi}}_L(\dot{\hat{\varphi}}_{L+} + \dot{\hat{\varphi}}_{R+}) + \frac{\hat{\varphi}_L^2}{C_J L}\right],\end{aligned}$$

where

$$\begin{cases}\hat{\varphi}_{L\pm} = \hat{\varphi}_1 \pm \hat{\varphi}_2 \\ \hat{\varphi}_{R\pm} = \hat{\varphi}_3 \pm \hat{\varphi}_4\end{cases}. \tag{4.17}$$

The subscript L (R) stands for left loop (right loop).
For $L \ll L_J$, the shared inductor variable $\hat{\varphi}_L$ has a capacitive and a magnetic energy that together form a high frequency LC resonance. Thus, $\hat{\varphi}_L$ can be considered as a "fast" degree of freedom, which means that rapidly adapts to the system and its average value can be considered constant [75]. Hence, all $\dot{\hat{\varphi}}_L$-terms can be neglected

$$\begin{aligned}\hat{\mathscr{H}} = &\left(\frac{\Phi_0}{2\pi}\right)^2 \frac{C_J}{2}\left[\left(\frac{1}{2}+\alpha_1\right)\dot{\hat{\varphi}}_{L+}^2 + \left(\frac{1}{2}+\alpha_2\right)\dot{\hat{\varphi}}_{R+}^2 + \dot{\hat{\varphi}}_{L-}^2 + \dot{\hat{\varphi}}_{R-}^2\right] + \\ &- E_J\left[2\cos\frac{\hat{\varphi}_{L+}}{2}\cos\frac{\hat{\varphi}_{L-}}{2} + 2\cos\frac{\hat{\varphi}_{R+}}{2}\cos\frac{\hat{\varphi}_{R-}}{2} + \right. \\ &\left.+\alpha_1\cos(2\pi f_1 + \hat{\varphi}_L - \hat{\varphi}_{L+}) + \alpha_2\cos(2\pi f_2 - \hat{\varphi}_L - \hat{\varphi}_{R+})\right] + \\ &+ \left(\frac{\Phi_0}{2\pi}\right)^2 \frac{\hat{\varphi}_L^2}{2L},\end{aligned} \tag{4.18}$$

As in Sec. 4.1, the inductor variable is considered to be in a quasi-steady state [74, 75]. The Hamiltonian in Eq. (4.18) can be separated in

$$\hat{\mathscr{H}}'_{qL} = \left(\frac{\Phi_0}{2\pi}\right)^2 \frac{C_J}{2}\left[\left(\frac{1}{2}+\alpha_1\right)\dot{\hat{\varphi}}_{L+}^2 + \dot{\hat{\varphi}}_{L-}^2\right] - E_J\left[2\cos\frac{\hat{\varphi}_{L+}}{2}\cos\frac{\hat{\varphi}_{L-}}{2}\right],$$

$$\hat{\mathscr{H}}'_{qR} = \left(\frac{\Phi_0}{2\pi}\right)^2 \frac{C_J}{2}\left[\left(\frac{1}{2}+\alpha_2\right)\dot{\hat{\varphi}}_{R+}^2 + \dot{\hat{\varphi}}_{R-}^2\right] - E_J\left[2\cos\frac{\hat{\varphi}_{R+}}{2}\cos\frac{\hat{\varphi}_{R-}}{2}\right],$$

$$\hat{\mathscr{H}}'_{int} = \left(\frac{\Phi_0}{2\pi}\right)^2 \frac{\hat{\varphi}_L^2}{2L} - E_J\left[\alpha_1\cos(2\pi f_1 + \hat{\varphi}_L - \hat{\varphi}_{L+}) + \right. \tag{4.19}$$

$$\left.+\alpha_2\cos(2\pi f_2 - \hat{\varphi}_L - \hat{\varphi}_{R+})\right]. \tag{4.20}$$

Following the same strategy as in Sec. 4.1, it is assumed that $\sqrt{\langle\hat{\varphi}_L^2\rangle} \ll \Phi_0$ and, thus, the cosine terms in the interaction Hamiltonian can be expanded with respect to $\hat{\varphi}_L$. The resulting Hamiltonians look

$$\begin{aligned}\hat{\mathscr{H}}''_{q_L} = &\left(\frac{\Phi_0}{2\pi}\right)^2 \frac{C_J}{2}\left[\left(\frac{1}{2}+\alpha_1\right)\dot{\hat{\varphi}}_{L+}^2 + \dot{\hat{\varphi}}_{L-}^2\right] + \\ &- E_J\left[2\cos\frac{\hat{\varphi}_{L+}}{2}\cos\frac{\hat{\varphi}_{L-}}{2} + \alpha_1\cos(2\pi f_1 - \hat{\varphi}_{L+})\right] ,\end{aligned} \tag{4.21}$$

$$\begin{aligned}\hat{\mathscr{H}}''_{q_R} = &\left(\frac{\Phi_0}{2\pi}\right)^2 \frac{C_J}{2}\left[\left(\frac{1}{2}+\alpha_2\right)\dot{\hat{\varphi}}_{R+}^2 + \dot{\hat{\varphi}}_{R-}^2\right] + \\ &- E_J\left[2\cos\frac{\hat{\varphi}_{R+}}{2}\cos\frac{\hat{\varphi}_{R-}}{2} + \alpha_2\cos(2\pi f_2 - \hat{\varphi}_{R_+})\right] ,\end{aligned} \tag{4.22}$$

$$\hat{\mathscr{H}}''_{int} = \left(\frac{\Phi_0}{2\pi}\right)^2 \frac{\hat{\varphi}_L^2}{2L} - E_J\hat{\varphi}_L\left[\alpha_2\sin(2\pi f_2 - \hat{\varphi}_{R+}) - \alpha_1\sin(2\pi f_1 - \hat{\varphi}_{L+})\right] . \tag{4.23}$$

Following [75], the Born-Oppenheimer approximation is applied to the interaction term. Hence,

$$\begin{aligned}&\partial_{\varphi_L}\hat{\mathscr{H}}_{int}\big|_{\varphi_L^*} = 0 \\ &\left(\frac{\Phi_0}{2\pi}\right)^2 \frac{\varphi_L^*}{L} - E_J\left[\alpha_1\sin(2\pi f_1 - \varphi_{L+}) + \alpha_2\sin(2\pi f_2 - \varphi_{R+})\right] = 0 \\ &\Rightarrow \varphi_L^* = \left(\frac{2\pi}{\Phi_0}\right)^2 E_J\left[\alpha_2\sin(2\pi f_2 - \varphi_{R_+}) - \alpha_1\sin(2\pi f_1 - \varphi_{L_+})\right] .\end{aligned} \tag{4.24}$$

Since we are assuming $L \ll L_J$, i.e. φ_L quickly adapts to the system variations, $\hat{\varphi}_L$ can be substituted by the solution φ_L^* defined in Eq. (4.24). In this way, the Hamiltonians in Eq. (4.23) can be redefined as

$$\begin{aligned}\hat{\mathscr{H}}_{q_L} = &\left(\frac{\Phi_0}{2\pi}\right)^2 \frac{C_J}{2}\left[\left(\frac{1}{2}+\alpha_1\right)\dot{\hat{\varphi}}_{L+}^2 + \dot{\hat{\varphi}}_{L-}^2\right] - E_J\left[+2\cos\frac{\hat{\varphi}_{L+}}{2}\cos\frac{\hat{\varphi}_{L-}}{2}\right. \\ &\left. +\alpha_1\cos(2\pi f_1 - \hat{\varphi}_{L+}) - \left(\frac{2\pi}{\Phi_0}\right)^2 LE_J\alpha_1^2\sin^2(2\pi f_1 - \hat{\varphi}_{L+})\right] , \\ \hat{\mathscr{H}}_{q_R} = &\left(\frac{\Phi_0}{2\pi}\right)^2 \frac{C_J}{2}\left[\left(\frac{1}{2}+\alpha_2\right)\dot{\hat{\varphi}}_{R+}^2 + \dot{\hat{\varphi}}_{R-}^2\right] - E_J\left[2\cos\frac{\hat{\varphi}_{R+}}{2}\cos\frac{\varphi_{R-}}{2}\right. \\ &\left. +\alpha_2\cos(2\pi f_2 - \hat{\varphi}_{R_+}) - \left(\frac{2\pi}{\Phi_0}\right)^2 LE_J\alpha_2^2\sin^2(2\pi f_2 - \hat{\varphi}_{R+})\right] , \\ \hat{\mathscr{H}}_C = &\left(\frac{2\pi}{\Phi_0}\right)^2 LE_J^2\alpha_1\alpha_2\sin(2\pi f_1 - \hat{\varphi}_{L+})\sin(2\pi f_2 - \hat{\varphi}_{R+}) .\end{aligned}$$

Let's note that, in the limit $L \to 0$, there is no coupling and the two qubit Hamiltonians are exactly the ones of two uncoupled three-junction flux qubits.
Here again, the previous results can be written in terms of current operators:

$$\begin{aligned}\hat{\mathscr{H}}_{q_L} =& \left(\frac{\Phi_0}{2\pi}\right)^2 \frac{C_J}{2}\left[\left(\frac{1}{2}+\alpha_1\right)\dot{\hat{\varphi}}_{L+}^2 + \dot{\hat{\varphi}}_{L-}^2\right] - E_J\left[+2\cos\frac{\hat{\varphi}_{L+}}{2}\cos\frac{\hat{\varphi}_{L-}}{2}+\right.\\ &\left.+\alpha_1\cos(2\pi f_1 - \hat{\varphi}_{L+})\right] - L\hat{I}_{p_L}^2\,, \qquad (4.25)\\ \hat{\mathscr{H}}_{q_R} =& \left(\frac{\Phi_0}{2\pi}\right)^2 \frac{C_J}{2}\left[\left(\frac{1}{2}+\alpha_2\right)\dot{\hat{\varphi}}_{R+}^2 + \dot{\hat{\varphi}}_{R-}^2\right] - E_J\left[2\cos\frac{\hat{\varphi}_{R+}}{2}\cos\frac{\hat{\varphi}_{R-}}{2}+\right.\\ &\left.+\alpha_2\cos(2\pi f_2 - \hat{\varphi}_{R+})\right] - L\hat{I}_{p_R}^2\,,\\ \hat{\mathscr{H}}_C =& L\hat{I}_{p_L}\hat{I}_{p_R}\,. \qquad (4.26)\end{aligned}$$

In the two-state approximation, $\hat{I}_{p_L} = I_p^L\hat{\sigma}_z^L$ ($\hat{I}_{p_R} = I_p^R\hat{\sigma}_z^R$) is the persistent current operator in the left (right) loop, written in the respective qubit current base. Finally, the coupling strength can be defined as

$$g = \frac{LI_{p_L}I_{p_R}}{\hbar}\,, \qquad (4.27)$$

which is the classical expression of the magnetic energy in an inductor with current $I_P^L + I_P^R$. A similar result can be found in [78], where the two qubits are coupled through mutual inductance.
Therefore, we have found that, under the assumption of $L \ll L_J$, it is possible to express the coupling term of the qubit-qubit Hamiltonian system with its classical approximation.

5

Persistent current readout: Theory

In Ch. 4, the interaction between a flux qubit coupled through a shared inductor L to other circuits was analysed. It was shown that, under low coupling strength conditions, the interaction can be expressed in the classical approximation ($LI_{qubit}I_{circuit}$). These results are used in this chapter to present the persistent current readout (PCR) of a flux qubit. Such a novel readout circuit is particularly intended for quantum annealing, where the qubit Hamiltonian has to be projected on the persistent current state basis (see Ch. 1). In Sec. 5.1, the readout circuit is presented in a semiclassical and phenomenological fashion to shed light on the differences between the existing PCR circuits. Then, in Sec. 5.2, the circuit quantization of the persistent current readout is presented and, in Sec. 5.3, the quantum optics model is derived and discussed.

5.1 The persistent current readout

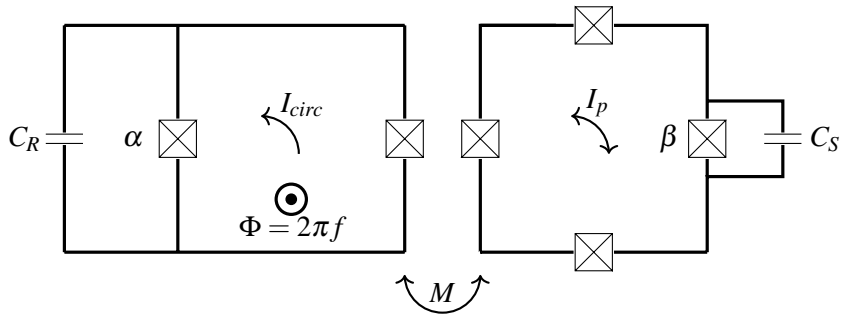

Figure 5.1: Circuit diagram of a four-junction flux qubit mutually coupled to a capacitively shunted asymmetric dc-SQUID.

The main principle of the persistent current readout (PCR) developed in this thesis is to employ a resonator where a portion of its inductance is replaced by an asymmetric dc-SQUID (see Sec. 1.2.2), inductively coupled to a flux qubit. Through changes of the resonance frequency, the SQUID resonator detects the persistent current state of the qubit. With respect to the circuits discussed in Ch. 4, there is no physical inductor shared between the two circuits: the resonator, which is a capacitively shunted dc-SQUID, is coupled to the qubit via mutual geometric inductance M (see Fig. 5.1).

Since the first proposal of the persistent current (PC) qubit [40], dc-SQUIDs have been the preferred dectors to measure the PC qubit states. In the first experimental demonstration of this kind of qubit [79], a dc-SQUID was coupled to the flux qubit by mutual inductance. A ramp of current was applied to the dc-SQUID in order to measure its switching current I_{sw}, which was a function of the total magnetic flux through it. A similar approach is presented in [80], where a dc-SQUID was shunted by a capacitance to optimize the I_{sw} detection. By contrast, in [81], a C-shunted dc-SQUID was used to detect the persistent current qubit state by driving it with an AC current and measuring the AC voltage response of the SQUID. However, this readout system needed a first characterization of the switching current. All these initial flux qubit experiments were based on the switching current distribution, which typically has an intrinsic amplitude larger than or comparable to the variation induced by two PC qubit states. For this reason, these techniques need robust statistics to accurately detect the qubit state and are strongly affected by circuitry noise [81].
In [82, 83], a dc-SQUID-based resonator was used to detect the current state of a

flux qubit by employing the bifurcation readout technique. This technique, which had equivalent implementations in hybrid charge-flux qubits [84, 85], consists of strongly driving the dc-SQUID resonator to its non-linear regime with a high-power microwave drive close to the resonance frequency of the SQUID. Under specific power conditions, the resonator show hysteric behaviour and can fall into two different oscillation states (l and h), with different amplitudes and phases of oscillation. The dc-SQUID drive amplitude and frequency have to be tuned so that each oscillation phase is connected to a qubit PC state. Although this readout does not depend on I_{sw} and the fidelity of this technique was high, the qubit coherence was impaired by the low resonator frequency used and the biasing circuit noise. In addition, high-amplitude driving may result in beating effects and quasiparticle generation.

Finally, in [59, 47], a first example of a persistent current readout for quantum annealing was designed as a CPW resonator with an rf-SQUID as a termination. As noted in [59], this readout circuit has the disadvantage of always being coupled to the qubit and thus the noise coming from the readout circuit induces a reduction in the qubit coherence times. As a solution, a tunable coupler was added between the flux qubit and the rf-SQUID. Despite showing a successful decoupling of the qubit, the coupler leads to an increase in the number of lines needed to operate the system, thus increasing the cost of the scalability of this type of readout .

In this thesis, the implementation of an unbiased dc-SQUID resolves many limitations of the previous instances. By employing a dc-SQUID-based resonator, decoupling from the qubit is possible by setting the dc-SQUID in its flux-insensitive flux bias point (i.e. $\Phi = 0$). On the other hand, the dc-SQUID on-chip circuitry contains no dissipative elements that could affect the qubit coherence, it needs no I_{sw} calibration (as in [81, 83, 80]), and it is operated without high-power driving (as in [82]).

The PCR method we propose is based on the circuit of the device shown in Fig. 5.1. In this system, due to mutual inductance M, a current circulating in the qubit loop I_p generates an external magnetic flux to the SQUID, $\Delta\Phi = MI_p$. A variation in the qubit persistent current ΔI_p causes a change in the effective inductance of the SQUID, ΔL, leading to a change in the dc-SQUID resonator frequency, $\Delta\omega$, where ω is defined as

$$\omega = \frac{1}{\sqrt{LC_R}},$$

with L the dc-SQUID inductance and C_R its shunt capacitance. Note that, here, L does not take into account the geometric inductance of the dc-SQUID. In Ch. 6, the actual dc-SQUID inductance is considered $L_{tot} = L_g + L$.

The change of frequency can be detected following the usual dispersive readout methods from cQED. To understand the mechanism behind this particular readout system, we have to first focus on the dc-SQUID itself. As reported in [36], a dc-SQUID can be regarded as a non-linear inductor. In the implementation of the PCR developed in this work, the dc-SQUID has no direct current bias other than any possible current noise from the measurement circuitry, which can be considered much smaller than the critical current of the SQUID junctions at the operational flux bias point.
Let's consider the dc-SQUID as a single junction obeying the second Josephson equation [36]:

$$V = \frac{\hbar}{2e}\frac{\partial \varphi_e}{\partial t}\,, \tag{5.1}$$

where φ_e is phase difference across the dc-SQUID, as presented in Sec. 1.2.2. On the other hand, such a circuit element can be regarded as an inductor, which has the well-known relation between the voltage at its ends and the current flowing through it, $V = L\frac{dI}{dt}$.
Recalling Eq. (1.17), the bias and circulating currents in a dc-SQUID are defined as

$$\begin{cases} I_b = I_0 \sin\gamma_1 + \alpha I_0 \sin\gamma_2 \\ I_{circ} = \frac{I_0 \sin\gamma_1 - \alpha I_0 \sin\gamma_2}{2} \end{cases}, \tag{5.2}$$

where α quantifies the asymmetry of the dc-SQUID junctions and I_0 is the junction critical current. Thus, introducing the semi-difference and semi-sum phases,

$$\begin{cases} \varphi_i = \frac{\gamma_l - \gamma_r}{2} \\ \varphi_e = \frac{\gamma_l + \gamma_r}{2} \end{cases}, \tag{5.3}$$

it is straightforward to obtain the following relation by combining Eq. (5.1) and Eq. (5.14)

$$\frac{\Phi_0}{2\pi}\frac{\partial \varphi_e}{\partial t} = L\left[2\cos\varphi_i \cos\varphi_e - (1-\alpha)\cos(\varphi_e - \varphi_i)\right]\frac{\partial \varphi_e}{\partial t}\,,$$

which brings the form of L

$$L = \frac{\Phi_0}{2\pi I_0\left[2\cos\varphi_i\cos\varphi_e - (1-\alpha)\cos(\varphi_e - \varphi_i)\right]}\,.$$

Using trigonometric relations, it is possible to reduce the previous formula to

$$L = \frac{\Phi_0}{2\pi I_c(\varphi_i)\cos(\beta(\varphi_i) + \varphi_e)}\,, \tag{5.4}$$

where

$$\beta(\varphi_i) = \tan^{-1}\left[\frac{1-\alpha}{1+\alpha}\tan\varphi_i\right], \quad I_c(\varphi_i) = I_0\sqrt{1+\alpha^2+2\alpha\cos(2\varphi_i)}\,.$$

Furthermore, Eq. (5.4) can be rewritten as [36]

$$L = \frac{\Phi_0}{2\pi\sqrt{I_c^2(\varphi_i) - I_b^2}}\,. \tag{5.5}$$

Since we are in the limit of a negligible bias current I_b, the inductance defined in Equation (5.5) can always be considered positive. Thus, a capacitively shunted dc-SQUID can be considered as a non-linear *LC* resonator, whose inductance is defined by Eq. (5.4) and Eq. (5.5).
For a more intuitive presentation of the main characteristics of such a resonator, let us consider a symmetric dc-SQUID ($\alpha = 1$). In this case, Eq. (5.4) is reduced to

$$L = \frac{\Phi_0}{4\pi I_0 \cos\varphi_i \cos\varphi_e}\,. \tag{5.6}$$

As shown in Sec. 1.2.2, φ_i is associated with the phase difference between the two SQUID junctions. Following refs. [28, 35, 36]

$$\varphi_i = \frac{\pi}{\Phi_0}MI_p + \pi f = \frac{\bar{\varphi}_q}{2} + \pi f\,, \tag{5.7}$$

where $2\pi f = \Phi_{ext}/\Phi_0$ is the normalized applied flux to the dc-SQUID and $\bar{\varphi}_q = \pm\, 2\pi MI_p/\Phi_0$ is the normalized flux generated by the persistent current flowing through the qubit loop. Let us point out that, in the case of a global magnetic field, the applied flux on the dc-SQUID is not equal to the flux applied on the qubit. The two fluxes respect the relation

$$\frac{f}{A_{SQ}} = \frac{f_q}{A_q}\,, \tag{5.8}$$

where A_{SQ}, A_q and f_q are the area of the SQUID, the qubit loop area, and the qubit flux, respectively.
As it is clear from Eq. (5.6) and Eq. (5.7), if the applied flux is fixed, the resonance frequency depends only on the qubit persistent current state. Hence, a dc-SQUID-based resonator can be used to directly measure the persistent current direction, i.e. the qubit state in the current basis.
From Eq. (5.6), the frequency shift of the dc-SQUID resonator for a fixed external flux f can be calculated as

$$\Delta\omega_\pm = \left(\frac{1}{\sqrt{L_- C}} - \frac{1}{\sqrt{L_+ C}}\right) \simeq \omega_0\bar{\varphi}_q\tan(\pi f)\,, \tag{5.9}$$

where

$$L_{\pm} = \frac{\Phi_0}{4\pi I_0 \cos\left(\pi f \pm \frac{\pi}{\Phi_0} M I_p\right) \cos\varphi_e} , \tag{5.10}$$

and

$$\begin{aligned} \omega_0 &= \left(\frac{\Phi_0 C_R}{4\pi I_0 \cos(\pi f)\cos\varphi_e}\right)^{-1/2} \simeq \left(\frac{\Phi_0 C_R}{4\pi I_0 \cos(\pi f)\cos\varphi_{DC}}\right)^{-1/2} \\ &\equiv \frac{1}{\sqrt{L_0 C_R}} , \end{aligned} \tag{5.11}$$

where we are approximating $\cos\varphi_e = \cos(\varphi_{SQ} + \varphi_{DC}) \simeq \cos\varphi_{DC} + \varphi_{SQ}\sin\varphi_{DC} \approx \cos\varphi_{DC}$, with φ_{SQ} the dc-SQUID phase and φ_{DC} the phase generated by the bias current, which is assumed low, i.e. $\varphi_{DC}/\Phi_0 \ll 1$. In Eq. (5.11), L_0 is defined as

$$L_0 \equiv \frac{\Phi_0}{4\pi I_0 \cos(\pi f)\cos\varphi_{DC}} . \tag{5.12}$$

Let's point out that for $f = 0$ (i.e. no external flux injected in the dc-SQUID), $\Delta\omega_{\pm} = 0$, as the dc-SQUID is to first order flux insensitive at that point.
In summary, it is demonstrated that, under the assumption of negligible bias current, a shunted dc-SQUID can be considered as a resonator with a flux-dependent non-linear inductor. It is important to point out that this result is achieved in a semiclassical framework, as the SQUID is not quantized.

5.1.1 SQUID noise mitigation

So far, the effect on the qubit from external current passing through the dc-SQUID on the qubit has not been discussed. In the same way in which the circulating current in the qubit injects a magnetic flux into the dc-SQUID loop, any circulating current through the SQUID would induce a flux in the qubit, causing a back-action, which can be a source of decoherence due to noise coming from the SQUID measuring circuitry.
In order to cancel the back-action effect from external bias noisy currents, note that the two branches of the SQUID have a mutual-inductance asymmetry with respect to the qubit, i.e. the two branches couple differently to the qubit. Hence, it is desirable to have the sum of the two fluxes lead to zero flux injection to the qubit

$$M_r I_r + M_l I_l = 0 , \tag{5.13}$$

where M_r (M_l) is the mutual inductance between the right (left) branch of the SQUID and the qubit loop, and I_r (I_l) is the current flowing through branch l (r). From Sec. 1.2.2,

$$\begin{cases} I_r = I_0 \sin\gamma_r \\ I_l = I_0 \sin\gamma_l \end{cases},$$

where γ_i is the phase across junction $i = l, r$. From Kirchhoff's equations, two other quantities can be introduced:

$$\begin{cases} I_b = I_l + I_r \\ J = \frac{I_l - I_r}{2} \end{cases} \Longrightarrow \begin{cases} I_l = \frac{1}{2} I_b + J \\ I_r = \frac{1}{2} I_b - J \end{cases}, \tag{5.14}$$

where I_b is the bias current applied to the SQUID and J is the circulating current of the SQUID.
Substituting Eq. (5.14) in Eq. (5.13), the following relation is obtained

$$\frac{M_r + M_l}{2} I_b + (M_l - M_r) J = 0 \Longrightarrow I_b + aJ = 0\,, \tag{5.15}$$

where $a = 2\frac{M_l - M_r}{M_l + M_r}$. Please, note that in the case of a dc-SQUID symmetrically surrounding the qubit, as in [35], the two mutual inductances will be equal, $M_r = M_l$, thus Eq. (5.15) is reduced to $I_b = 0$.
Introducing the semi-sum (φ_e) and the semi-difference (φ_i) of the phases, Eq. (5.15) can be rewritten as:

$$\cos\varphi_i \sin\varphi_e + a\cos\varphi_e \sin\varphi_i = 0 \Rightarrow \tan\varphi_i = -\frac{1}{a}\tan\varphi_e\,, \tag{5.16}$$

where φ_i depends on the external flux through the SQUID (see Eq. (5.7)), and hence it can be externally adjusted. In Sec. 1.2.2, it was shown that φ_e can be adjusted with I_b. In the circuit presented Sec. 5.1, there is no possible way to change I_b. When the condition in Eq. (5.16) is satisfied, in the limit of a small bias current, i.e. $I_b \approx 0$, there is no back-action on the qubit when the dc-SQUID is at $f = 0$, since $J = 0$, as it is clear from Eq. (5.15). Alternatively, a bias current can be injected by employing the circuit in Fig. 5.2. In this modified SQUID circuit, the circulating current in the extra loop with a large inductance L_b represents the bias current of the dc-SQUID loop. Thus, it is possible to adjust I_b by changing the flux f_b. Moreover, if $L_b \gg L_J$, the presence of the parallel inductance does not affect the SQUID resonance frequency. This approach was already implemented with phase qubits [86, 87, 39], but it is not taken into consideration in this thesis.

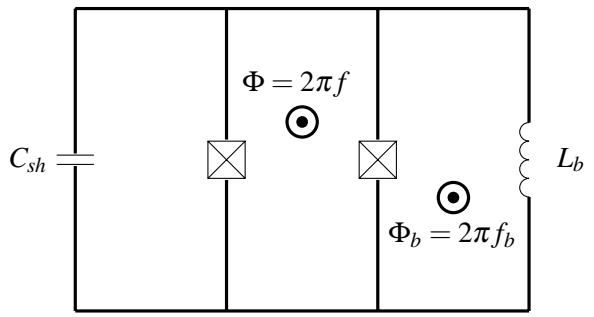

Figure 5.2: Dc-SQUID capacitively and inductively shunted. Tuning the flux f_b in the inductance loop, it is possible to tone the dc-SQUID bias current I_b.

In order to mitigate the effect of the back-action of the dc-SQUID, φ_i can be adjusted by an additional external flux threading the dc-SQUID. As will be detailed in Sec. 6.1, this is possible by the presence of a dedicated flux bias line coupled to the dc-SQUID.
In conclusion, it is demonstrated that it is possible to uncouple the qubit external flux from the dc-SQUID circulating current. In this way, the qubit Hamiltonian would be exactly the one described in Eq. (3.1) and Eq. (3.3) of an isolated qubit, aside from a small renormalization of the qubit parameters, since there is no SQUID flux interfering with the qubit while the measurement is not taking place. In addition, a Purcell filter can be added to mitigate the noise to the SQUID resonator further [88].

5.2 Circuit quantization of the PCR

The analysis performed so far was made in a semi-classical framework. In this section, the Hamiltonian of the whole qubit-SQUID system is derived. As shown in Sec. 4.1 and Sec. 4.2, when the coupling inductance is small compared to the uncoupled system energies, the total Hamiltonian can be written as the sum of three terms: a coupling term, a qubit term, and a SQUID term. Since the qubit Hamiltonian was already described in Ch. 3, the first part of this section is dedicated to the circuit quantization of an asymmetric dc-SQUID. Then, the total circuit Hamiltonian is presented and discussed.

5.2.1 Asymmetric dc-SQUID quantization

Following form Sec. 4.1 and Sec. 4.2, in this section we will introduce several approximations to simplify the complexity of the total Hamiltonian, in order to

discuss the effect of the interaction between the qubit and our readout resonator. To be as general as possible, we consider an asymmetric dc-SQUID, as in Fig. 5.1. The quantized Hamiltonian of this circuit can be written as [35, 89]

$$\begin{aligned}\hat{\mathscr{H}}_{SQ} = &\left(\frac{2\pi}{\Phi_0}\right)^2 \frac{1}{8\gamma C_J}\left[(\gamma+1)(\hat{p}_e^2+\hat{p}_i^2)-(1-\gamma)\hat{p}_e\hat{p}_i\right] \\ &-2E_J\cos\hat{\varphi}_e\cos\hat{\varphi}_i + E_J(1-\alpha)\cos(\hat{\varphi}_e-\hat{\varphi}_i) \quad ,\end{aligned} \tag{5.17}$$

where

$$\gamma = \frac{C_R+\alpha C_J}{C_J} \quad \text{and} \quad \begin{cases}\hat{\varphi}_e = \frac{\hat{\varphi}_1+\hat{\varphi}_2}{2} \\ \hat{\varphi}_i = \frac{\hat{\varphi}_1-\hat{\varphi}_2}{2}\end{cases} \quad , \tag{5.18}$$

with C_S the capacitance of the SQUID shunt, C_J and $E_J = \Phi_0 I_1/2\pi$ the capacitance and Josephson energy of a junction, and the asymmetry $\alpha = I_1/I_2 < 1$, with I_1 and I_2 the critical currents of the dc-SQUID Josephson junctions. For $\alpha = 1$, Eq. (5.17) represents the Hamiltonian of a capacitively shunted symmetric dc-SQUID. The operators $\hat{p}_i, \hat{p}_e$ are conjugated to $\hat{\varphi}_i, \hat{\varphi}_e$, i.e. $[\hat{\varphi}_j, \hat{p}_k] = i\delta_{jk}$.
In order to introduce the effect of the qubit, as presented in [35], the external and internal phase variables can be re-expressed as

$$\begin{cases}\hat{\varphi}_e = \hat{\varphi}_{SQ} + \varphi_{DC} \\ \hat{\varphi}_i = \frac{\hat{\varphi}_q}{2} + \pi f\end{cases} \quad , \tag{5.19}$$

where $\hat{\varphi}_q$ is the operator form of the scalar $\bar{\varphi}_q$ (defined in Eq. (5.7)), φ_{DC} is the phase generated by the SQUID bias current, $2\pi f = \Phi/\Phi_0$ is the frustration, and $\hat{\varphi}_{SQ}$ is the phase operator describing the quantum fluctuations of the SQUID resonant mode [35, 36]. Substituting Eq. (5.19) in Eq. (5.17), the total Hamiltonian becomes

$$\begin{aligned}\hat{\mathscr{H}}_{SQ} = &\left(\frac{2\pi}{\Phi_0}\right)^2 \frac{1}{8\gamma C_J}\left[(\gamma+1)(\hat{p}_{SQ}^2+\hat{p}_q^2)-(1-\gamma)\hat{p}_{SQ}\hat{p}_q\right] \\ &-2E_J\cos(\hat{\varphi}_{SQ}+\varphi_{DC})\cos(\hat{\varphi}_q+\pi f) \\ &+E_J(1-\alpha)\cos(\hat{\varphi}_{SQ}+\varphi_{DC}-\hat{\varphi}_q-\pi f) \quad .\end{aligned} \tag{5.20}$$

where $\hat{p}_i$ is the conjugate variable of $\hat{\varphi}_i$.
Now, some approximations must be made. As in Sec. 4.1 and Sec. 4.2, the $\hat{p}_q^2$-term is a renormalization of the qubit Hamiltonian (see Eq. (4.13) and Eq. (4.25)), while the $\hat{p}_q\hat{p}_{SQ}$ is a coupling term between the qubit and the SQUID induced by the capacitances of the two systems, which can be neglected given the small geometric coupling capacitance in this kind of circuits [90]. Therefore, the Hamiltonian now

looks like:

$$\hat{\mathscr{H}}_{SQ} \simeq \left(\frac{2\pi}{\Phi_0}\right)^2 \frac{\gamma+1}{8\gamma C_J}\hat{p}_{SQ}^2 + \hat{\mathscr{H}}_q^{(ren)} - 2E_J\cos(\hat{\varphi}_{SQ}+\varphi_{DC})\cos(\hat{\varphi}_q+\pi f) + \\ + E_J(1-\alpha)\cos(\hat{\varphi}_{SQ}+\varphi_{DC}-\hat{\varphi}_q-\pi f) \quad . \tag{5.21}$$

where the qubit Hamiltonian renormalization term $\hat{\mathscr{H}}_q^{(ren)}$ is

$$\hat{\mathscr{H}}_q^{(ren)} = \left(\frac{2\pi}{\Phi_0}\right)^2 \frac{\gamma+1}{8\gamma C_J}\hat{p}_q^2 . \tag{5.22}$$

$\hat{\mathscr{H}}_q^{(ren)}$ renormalizes the qubit kinetic energy term, leading to a modification of the qubit properties (Δ and I_p).
Equation (5.21) can be further simplified. Since C_R must be large enough to avoid a too high SQUID resonance frequency, we have $E_J \gg E_c$ for the dc-SQUID. Following [11, 91, 35], this means that the SQUID quantum fluctuations of the phase operator $\hat{\varphi}_{SQ}$ are small, i.e. $\frac{1}{\Phi_0}\sqrt{\langle\hat{\varphi}_{SQ}^2\rangle} = \frac{1}{\Phi_0}\sqrt{\frac{\hbar}{2}\sqrt{\frac{L}{C_S}}} \ll 1$, with L the dc-SQUID inductance[1]. Moreover, since the typical values of M and I_p are, respectively, in the $1-10$ pH and $10-100$ nA range, $\langle\hat{\varphi}_q\rangle \ll \Phi_0$. For these reasons, it is possible to expand the cosine product in the Taylor series in Eq. (5.21).
Retaining terms up to the second order in $\hat{\varphi}_q$ and $\hat{\varphi}_{SQ}$, the approximated Hamiltonian looks like

$$\hat{\mathscr{H}}_{SQ} \simeq \left(\frac{2\pi}{\Phi_0}\right)^2 \frac{\gamma+1}{8\gamma C_J}\hat{p}_{SQ}^2 + \hat{\mathscr{H}}_q^{(ren)} \\ + E_J[F_s\hat{\varphi}_{SQ} + F_q\hat{\varphi}_q + F_{sq}\hat{\varphi}_q\hat{\varphi}_{SQ} + \frac{1}{2}F_{s^2}\hat{\varphi}_{SQ}^2 - F_{s^2q}\hat{\varphi}_{SQ}^2\hat{\varphi}_q] , \tag{5.23}$$

where the following scalar functions are introduced

$$F_s = 2\cos\pi f\sin\varphi_{DC} + (1-\alpha)\sin(\pi f - \varphi_{DC}) , \tag{5.24}$$
$$F_q = 2\sin\pi f\cos\varphi_{DC} - (1-\alpha)\sin(\pi f - \varphi_{DC}) , \tag{5.25}$$
$$F_{sq} = (1-\alpha)\cos(\pi f - \varphi_{DC}) - 2\sin\pi f\sin\varphi_{DC} , \tag{5.26}$$
$$F_{s^2} = 2\cos\pi f\cos\varphi_{DC} - (1-\alpha)\cos(\pi f - \varphi_{DC}) , \tag{5.27}$$
$$F_{s^2q} = (1-\alpha)\cos\pi f\sin\varphi_{DC} + (1+\alpha)\sin\pi f\cos\varphi_{DC} . \tag{5.28}$$

[1] L is defined in Eq. (5.5). Since it has been derived in a semiclassical framework in the symmetric case, L_{SQ} will be defined in Eq. (5.34) as the effective dc-SQUID inductance and will substitute L in our approximations.

Note that, in the case of a symmetric dc-SQUID with a low bias current, i.e. $\alpha = 1$ and $\varphi_{DC} \to 0$, Eqs. (5.24) to (5.28) are reduced to

$$F_s = 0\,, \tag{5.29}$$
$$F_q = 2\sin\pi f\cos\varphi_{DC}\,, \tag{5.30}$$
$$F_{sq} = 0\,, \tag{5.31}$$
$$F_{s^2} = \cos\pi f\cos\varphi_{DC}\,, \tag{5.32}$$
$$F_{s^2q} = 2\sin\pi f\cos\varphi_{DC}\,. \tag{5.33}$$

Furthermore, the term $\propto \varphi_{SQ}^2$ in Eq. (5.23) can be rewritten as

$$\frac{1}{2}E_J F_{s^2}\hat{\varphi}_{SQ}^2 = \frac{\Phi_0 I_1}{4\pi}F_{s^2}\hat{\varphi}_{SQ}^2 \equiv \left(\frac{\Phi_0}{2\pi}\right)^2\frac{\hat{\varphi}_{SQ}^2}{2L_{SQ}}\,,$$

where we defined the effective SQUID inductance

$$L_{SQ} = \frac{\Phi_0}{2\pi I_1 F_{s^2}}\,. \tag{5.34}$$

After some trigonometry, Eq. (5.27) can be written as

$$I_1 F_{s^2} = I_c(\pi f)\cos(\beta(\pi f) + \varphi_{DC})\,,$$

where

$$\beta(\pi f) = \tan^{-1}\left[\frac{1-\alpha}{1+\alpha}\tan\pi f\right], \quad I_c(\pi f) = I_1\sqrt{1+\alpha^2+2\alpha\cos(2\pi f)}\,.$$

Hence, Eq. (5.34) is a special case of Eq. (5.4), in which there is no flux injection to the SQUID ($\bar{\varphi}_q = 0$) and $\varphi_e = \varphi_{DC}$, i.e. $\langle\hat{\varphi}_{SQ}\rangle \ll \varphi_{DC}$. Hence, following Eq. (5.5), we can define the effective SQUID inductance to be positive, $L_{SQ} \geq 0$.
Going back to the Hamiltonian in Eq. (5.23), it is possible to recognize the Hamiltonian of a quantum harmonic oscillator

$$\hat{\mathscr{H}}_R = \left(\frac{2\pi}{\Phi_0}\right)^2\frac{1}{2C_{SQ}}\hat{p}_{SQ}^2 + \left(\frac{\Phi_0}{2\pi}\right)^2\frac{\hat{\varphi}_{SQ}^2}{2L_{SQ}} \quad ,$$

where

$$C_{SQ} = \frac{4\gamma C_J}{\gamma+1} \quad .$$

The term proportional to $\hat{\varphi}_{SQ}$ in Eq. (5.23) can be added as a displacement in the potential of the SQUID $(\hat{\varphi}_{SQ} - \varphi_{SQ}^0)^2$. A similar argument follows for $\hat{\varphi}_q$ for the qubit.

At this point, it is possible to introduce the creation and annihilation operators of a C-shunted dc-SQUID treated as a harmonic oscillator

$$\begin{cases} \hat{\varphi}_{SQ} = \frac{\Phi_0}{2\pi}\sqrt{\frac{\hbar L_{SQ}\omega_{SQ}}{2}}\left(\hat{a}^\dagger + \hat{a}\right) \\ \hat{p}_{SQ} = i\frac{2\pi}{\Phi_0}\sqrt{\frac{\hbar C_{SQ}\omega_{SQ}}{2}}\left(\hat{a}^\dagger - \hat{a}\right) \end{cases} \quad \text{with} \quad \omega_{SQ} = \frac{1}{\sqrt{L_{SQ}C_{SQ}}}\,, \tag{5.35}$$

and, as in Eq. (4.11), the current operator of the SQUID can be defined as

$$\begin{aligned} \hat{I}_r \equiv \frac{\partial \hat{Q}}{\partial t} = \frac{2\pi}{\Phi_0}\frac{\partial \hat{p}_{SQ}}{\partial t} = \sqrt{\frac{\hbar\omega}{2L_{SQ}}}(\hat{a}^\dagger + \hat{a}) = \\ = I_{rms}(\hat{a}^\dagger + \hat{a}) = \frac{1}{L_{SQ}}\frac{\Phi_0}{2\pi}\hat{\varphi}_{SQ}\,, \end{aligned} \tag{5.36}$$

which implies

$$\hat{\varphi}_{SQ} = \frac{2\pi L_{SQ}}{\Phi_0}\hat{I}_r\,. \tag{5.37}$$

Now, substituting Eqs. (5.35) and (5.37) and $\hat{\varphi}_q = \frac{2\pi}{\Phi_0}M\hat{I}_p$ in Eq. (5.23), the approximated Hamiltonian looks like

$$\begin{aligned} \hat{\mathscr{H}}_{SQ} \simeq \hbar\omega_{SQ}\left(a^\dagger a + \frac{1}{2}\right) + \hat{\mathscr{H}}_q^{(ren)} \\ + \frac{1}{2}\left(F_{sq}\lambda L_{SQ}\hat{I}_r\hat{I}_p - \frac{2\pi}{\Phi_0}F_{s^2q}\lambda\hat{I}_r^2\hat{I}_p\right)\,, \end{aligned} \tag{5.38}$$

where $\lambda = \frac{2\pi M I_1}{\Phi_0} = \frac{M}{L_J}$. This Hamiltonian contains two interaction terms to the qubit, one proportional to the resonator current, the other one to the current squared. Hence, in this section, it has been shown that the shunted dc-SQUID Hamiltonian can be described as a resonator Hamiltonian with an interaction term, in which the qubit degree of freedom plays an essential role.

5.2.2 Persistent current readout quantization

Following [35], the Hamiltonian of the whole system in Fig. 5.1 can be written as the sum of the qubit Hamiltonian, as defined in Sec. 3.1, and the SQUID Hamiltonian expressed in Eq. (5.38):

$$\hat{\mathscr{H}} = \hat{\mathscr{H}}_q + \hat{\mathscr{H}}_{SQ}\,. \tag{5.39}$$

In Eq. (5.38), it is possible to recognize a pure resonator term and two interaction terms. Thus, the whole Hamiltonian can be expressed as

$$\hat{\mathscr{H}} = \hat{\mathscr{H}}_q' + \hat{\mathscr{H}}_R + \hat{\mathscr{H}}_c, \tag{5.40}$$

where $\hat{\mathscr{H}}_q' = \hat{\mathscr{H}}_q + \hat{\mathscr{H}}_q^{(ren)}$ is the renormalized qubit Hamiltonian and

$$\hat{\mathscr{H}}_R = \hbar\omega_{SQ}\left(\hat{a}^\dagger\hat{a} + \frac{1}{2}\right), \tag{5.41}$$

$$\hat{\mathscr{H}}_c = \frac{1}{2}\left(F_{sq}\lambda L_{SQ}\hat{I}_r\hat{I}_p - \frac{2\pi}{\Phi_0}F_{s^2q}\lambda\hat{I}_r^2\hat{I}_p\right). \tag{5.42}$$

Now, the interacting part is clearly understood as a coupling term that hybridizes the qubit and the dc-SQUID resonator states. Moreover, it is interesting to notice differences and similarities between Eq. (5.42) and the results presented in Ch. 4. Using the definition of λ and Eq. (5.34), it is easy to rewrite:

$$\frac{1}{2}\lambda L_{SQ}F_{sq} = M\frac{L_{SQ}}{2L_J}F_{sq} = M\frac{(1-\alpha)\cos(\pi f - \varphi_{DC}) - 2\sin\pi f\sin\varphi_{DC}}{2\cos\pi f\cos\varphi_{DC} - (1-\alpha)\cos(\pi f - \varphi_{DC})} \equiv M_{eff}\,. \tag{5.43}$$

Hence, the first term can be identified as a dipolar interaction term [92, 93].

$$\hat{\mathscr{H}}_c^{(1)} \equiv M_{eff}\hat{I}_r\hat{I}_p\,,$$

where M_{eff} is an effective mutual inductance, similarly to Eq. (4.15). Let us point out that, for $\alpha = 1$ and $\varphi_{DC} = 0$, $M_{eff} = 0$ and, consequently, $\hat{\mathscr{H}}_c^{(1)} = 0$.
The $\hat{I}_r^2$ term of Eq. (5.42) cannot be neglected: as expressed in Eq. (5.32), $F_{sq} = 0$ in the case of a symmetric dc-SQUID with no bias current, which implies that the coupling Hamiltonian is reduced to $\propto \hat{I}_r^2\hat{I}_p$.
Therefore, the total Hamiltonian in Eq. (5.39) is reduced to Eq. (5.40), with $\hat{\mathscr{H}}_R$ and $\hat{\mathscr{H}}_c$ defined in Eq. (5.41) and Eq. (5.42), respectively, under the assumption of no flux injected into the qubit by the external current biasing the dc-SQUID.

5.3 Quantum optics of the persistent current readout

Finally, we have all the elements to understand the effects of the interactions in Eq. (5.42) on the spectrum of the coupled qubit-SQUID system. Let us approximate the qubit as a two-state system. Following [62], the two-level approximation of the current operator in the energy basis can be written as

$$\hat{I}_p = I_p\left(\frac{\varepsilon}{\omega_q}\hat{\sigma}_z - \frac{\Delta}{\omega_q}\hat{\sigma}_x\right) \quad ,$$

where, recalling from Ch. 1 and Ch. 3, $\hbar\Delta$ is the energy gap between the first two states of the qubit at $f = 0.5$, $\hbar\varepsilon = 2I_p(\Phi_f - \Phi_0/2)$ and $\omega_q = \sqrt{\Delta^2 + \varepsilon^2}$. Let's

consider a flux qubit operated at the symmetry point, i.e. $\varepsilon = 0$. The current operator is reduced to

$$\hat{I}_p = -I_p \hat{\sigma}_x \, .$$

Now it is possible to write Eq. (5.40) in terms of Pauli matrices and annihilation and creation operators[2]:

$$\mathscr{H}^{2s}/\hbar = \omega_{SQ} a^\dagger a + \frac{\omega_q}{2}\sigma_z - g_1(a^\dagger + a)\sigma_x - g_2(a^\dagger + a)^2\sigma_x \, , \tag{5.44}$$

where

$$\begin{aligned} g_1 &= \frac{M_{eff} I_p I_{rms}}{\hbar} = \frac{M I_p I_{rms}}{\hbar} \frac{(1-\alpha)\cos(\pi f - \varphi_{DC}) - 2\sin\pi f \sin\varphi_{DC}}{2\cos\pi f \cos\varphi_{DC} - (1-\alpha)\cos(\pi f - \varphi_{DC})} \, , \\ g_2 &= -\frac{1}{\hbar} F_{s^2 q} M \frac{L_{SQ}^2}{L_J} \frac{\pi}{\Phi_0} I_{rms}^2 I_p = -\frac{\pi}{\hbar \Phi_0} M_{eff}^{(2)} L_{SQ} I_{rms}^2 I_p = \\ &= -\frac{\pi}{\hbar \Phi_0} M L_{SQ} I_{rms}^2 I_p \frac{(1-\alpha)\cos\pi f \sin\varphi_{DC} + (1+\alpha)\sin\pi f \cos\varphi_{DC}}{2\cos\pi f \cos\varphi_{DC} - (1-\alpha)\cos(\pi f - \varphi_{DC})} \end{aligned} \, ,$$

with $M_{eff}^{(2)} = F_{s^2 q} M \frac{L_{SQ}}{L_J} = M \frac{F_{s^2 q}}{F_{s^2}}$. If the dc-SQUID is operated at its flux-insenstive points ($f = 0, 0.5$), with no bias current ($\varphi_{DC} = 0$)) the coupling strengths $g_1, g_2 = 0$. For a symmetric dc-SQUID ($\alpha = 1$), $g_1, g_2 = 0$ also for $f = 0$. In other words, under these conditions, the qubit and the dc-SQUID resonator are decoupled.
Moreover, if an unbiased symmetric dc-SQUID is considered (i.e. $\alpha = 1$ and $\varphi_{DC} = 0$)

$$g_1 = 0 \tag{5.45}$$

$$g_2 = -\frac{\pi}{\hbar \Phi_0} M L_{SQ} I_{rms}^2 I_p \tan\pi f = -\frac{\bar{\varphi}_q \omega_{SQ}}{2} \tan\pi f = -\frac{\Delta\omega_\pm}{2} \, , \tag{5.46}$$

where $\Delta\omega_\pm$ was already defined in Eq. (5.9), with $C_R \equiv C_{SQ}$.
Introducing the ladder operators $[\sigma_+, \sigma_-] = \sigma_z$, and expanding $(a^\dagger + a)^2$, Eq. (5.44) reads

$$\begin{aligned} \mathscr{H}^{2s}/\hbar = \omega_{SQ} a^\dagger a + \frac{\omega_q}{2}\sigma_z - g_1(a^\dagger + a)(\sigma_- + \sigma_+) \\ - g_2\left[(a^{\dagger 2} + a^2)(\sigma_- + \sigma_+) + (2a^\dagger a + 1)(\sigma_- + \sigma_+)\right] \, , \end{aligned} \tag{5.47}$$

which is a quantum Rabi model (QRM)-like Hamiltonian of the system in Fig. 5.1 [94].
This result can be further simplified by the rotating wave approximation (RWA) [35],

[2]For clarity, from now on, the hat on operators is omitted.

which is valid when $g_1/\omega_{SQ} \ll 1$ and $g_2/\omega_{SQ} \ll 1$, where we neglect the counter-rotating terms, (i.e. rotating with $2\omega_{SQ}+\omega_q$), and the terms proportional to $a^\dagger a(\sigma_- + \sigma_-)$, (i.e. rotating with ω_q). The final form of the approximated Hamiltonian of the whole system is, then,

$$\mathscr{H}^{2s}/\hbar \simeq \omega_{SQ} a^\dagger a + \frac{\omega_q}{2}\sigma_z - g_1(\sigma_- a^\dagger + \sigma_+ a) - g_2(\sigma_- a^{\dagger 2} + \sigma_+ a^2)\,. \tag{5.48}$$

With the form of the Hamiltonian as in Eq. (5.48), it is clear that the qubit-SQUID coupling is formed by single- and two-photon interaction terms. The Hamiltonian in Eq. (5.48) describes a two-photon Jaynes-Cummings (TPJC) model [95]. A similar solution can be found in [35], where a symmetric SQUID is used instead.
Therefore, in Eq. (5.48), we can clearly see the effect of the interaction between the qubit and the readout circuit, from a quantum optics point of view.

5.3.1 Dispersive shift in the persistent current readout

With Eq. (5.48), the effect of the qubit state on the frequency of the resonator can be calculated. The dispersive Hamiltonian for a qubit capacitively coupled to a readout resonator was found in Eq. (3.10). Clearly, that result cannot be used here due to the different nature of the qubit-resonator interaction. Still, we can apply the same approximations as in Sec. 3.2 to reach a similar result.
For simplicity, let's start by analyzing the case of an unbiased symmetric dc-SQUID, i.e. $g_1 = 0$. Since in our experiment $|g_2| \ll |\omega_{SQ} - \omega_q|$, it is possible to transform Eq. (5.48) to express the TPJC Hamiltonian in the dispersive regime.
In order to calculate the dispersive 2-photon Hamiltonian, we use the Schrieffer-Wolff (SW) transformation. The detailed calculation is presented in App. C.
The resulting Hamiltonian is

$$\mathscr{H}_{eff}/\hbar = \left[\omega'_{SQ} - \chi\left(a^\dagger a + 1\right)\sigma_z\right] a^\dagger a + \frac{\omega_q^{'}}{2}\sigma_z\,, \tag{5.49}$$

where

$$\omega'_{SQ} = \omega_{SQ} - 2\chi\,, \qquad \omega'_q = \omega_q - 2\chi\,,$$
$$\chi = \frac{g_2^2}{2\omega_{SQ} - \omega_q} = \frac{\Delta\omega_\pm^2}{4(2\omega_{SQ} - \omega_q)}\,.$$

In Eq. (5.49) it is stated that the SQUID-resonator frequency is shifted by $\chi[\sigma_z(a^\dagger a + 1) + 2]$. At the same time, the qubit frequency is shifted by $\chi[a^\dagger a(a^\dagger a + 1) + 2]$. It is interesting to note that, while there is a linear term in $(a^\dagger a)$, which returns an ac-Stark effect contribution to the resonator frequency, the $(a^\dagger a)^2$ term is a cross-Kerr term with the same order of approximation as the linear term. Equation (5.49)

defines the dispersive TPJC Hamiltonian, which conserves the number of the total excitation, $C = n + \sigma_z + 1$ [96]. For a general multi-photon Jaynes-Cummings Hamiltonian, the total excitation number is $C = n + (m/2)(\sigma_z + 1)$, where m is the number of photons mediating the interaction. Physically, this means that two resonator photons are required to induce a transition in the qubit state. Hence, the Hamiltonian can be represented as a block-diagonal matrix

$$\mathscr{H}_{eff}/\hbar = \begin{pmatrix} \boxed{E_0} & & & & & \\ & \boxed{E_1} & & & & \\ & & \boxed{\begin{matrix} E_2^- & 0 \\ 0 & E_2^+ \end{matrix}} & & 0 & \\ & & & \boxed{\begin{matrix} E_3^- & 0 \\ 0 & E_3^+ \end{matrix}} & & \\ & 0 & & & \ddots & \end{pmatrix}, \tag{5.50}$$

where each block defines a Hilbert subspace $\mathscr{H}^{(\mathscr{N})}$ with basis $\{|\mathscr{N}, g\rangle, |\mathscr{N}-2, e\rangle\}$, where $\mathscr{N}$ is the number of total excitations

$$\langle \mathscr{N}, g|C|\mathscr{N}, g\rangle = \mathscr{N} = \langle \mathscr{N}-2, e|C|\mathscr{N}-2, e\rangle \ . \tag{5.51}$$

The eigenvalues of each subspace $\mathscr{H}^{(n)}$ can be expressed as

$$\begin{cases} E_0 & = -\frac{\omega_q - 2\chi}{2} \\ E_1 & = \omega_{SQ} - \frac{\omega_q - 2\chi}{2} \\ E_{\mathscr{N}}^{\pm} & = \omega_{SQ}(\mathscr{N}-1) + \chi \pm \left[\omega_{SQ} - \frac{\omega_q}{2} + \chi(\mathscr{N}^2 - \mathscr{N})\right] \end{cases}, \tag{5.52}$$

where $\mathscr{H}_{eff}|\mathscr{N}, g\rangle = E_{\mathscr{N}}^{+}|\mathscr{N}, g\rangle$ and $\mathscr{H}_{eff}|\mathscr{N}-2, e\rangle = E_{\mathscr{N}}^{-}|\mathscr{N}-2, e\rangle$. Note that $\mathscr{H}^{(0)}$ and $\mathscr{H}^{(1)}$ are one-dimensional subspaces with basis $\{|0, g\rangle\}$ and $\{|1, g\rangle\}$. This result follows from the assumption that only the TPJC interaction plays a role in the effective Hamiltonian. Under this assumption, the resonator has to lose two photons from $|n, g\rangle$ to excite the qubit to $|n-2, e\rangle$, where n is now the number of photons in the resonator. As a consequence, it is not possible to excite the qubit if there are $n < 2$ photons in the resonator.

A graphical representation of the energy levels of the system is depicted in Fig. 5.3. Furthermore, defining the general system state as $|\Psi\rangle = |n, g/e\rangle$, it can be shown that the resonator frequency shift $\Delta\omega_{disp}$ is

$$\Delta\omega_{dips} = \omega_{SQ}^{(e)} - \omega_{SQ}^{(g)} = (E_{|1,e\rangle} - E_{|0,e\rangle}) - (E_{|1,g\rangle} - E_{|0,g\rangle}) = 4\chi \tag{5.53}$$

This shift must not be mistaken for the frequency shift presented in Eq. (5.9), as it is the shift of the energy states. In fact, so far in this section, the energy basis of

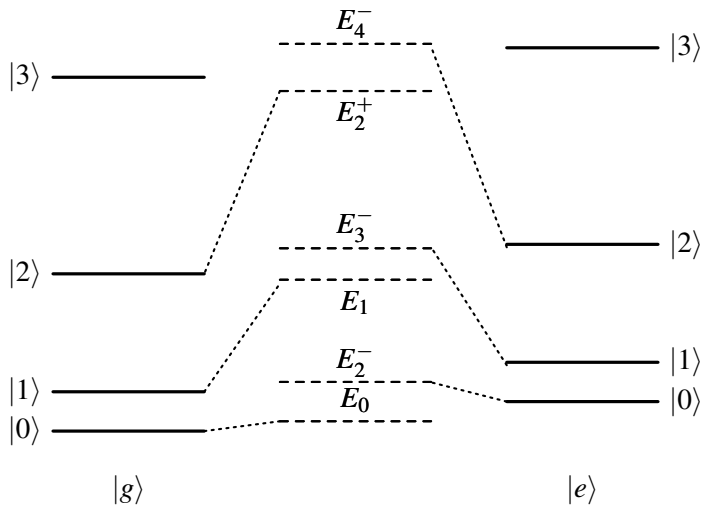

Figure 5.3: Energy levels of the qubit-PCR system in the symmetric unbiased case. Solid lines represent the bare energy levels (i.e. uncoupled system). Dashed lines in the center represent the dressed energy levels (i.e. coupled system). The dashed lines are labelled with the energies as defined in Eq. (5.50).

the qubit is always used, whereas the resonator frequency shift defined in Eq. (5.9) depends on the direction of the current flowing through the qubit. In order to obtain the shift due to the current change, Eq. (5.49) should be rotated to the current basis. In the current basis

$$\sigma_z^{(energy)} = \frac{\varepsilon}{\omega_q}\sigma_z^{(current)} + \frac{\Delta}{\omega_q}\sigma_x^{(current)} . \tag{5.54}$$

The rotated Hamiltonian is

$$\mathscr{H}_{eff}^{(current)}/\hbar = \left[\omega'_{SQ} - \chi\left(a^\dagger a + 1\right)\left(\frac{\varepsilon}{\omega_q}\sigma_z^{(current)} + \frac{\Delta}{\omega_q}\sigma_x^{(current)}\right)\right] a^\dagger a \tag{5.55}$$

$$+ \frac{\omega_q^{'}}{2}\left(\frac{\varepsilon}{\omega_q}\sigma_z^{(current)} + \frac{\Delta}{\omega_q}\sigma_x^{(current)}\right) , \tag{5.56}$$

where $\sigma_z^{(current)} = |\circlearrowright\rangle\langle\circlearrowright| - |\circlearrowleft\rangle\langle\circlearrowleft|$ and $\sigma_x^{(current)} = |\circlearrowright\rangle\langle\circlearrowleft| + |\circlearrowleft\rangle\langle\circlearrowright|$. Thus, the frequency shift can be calculated

$$\omega_{SQ}^{(\circlearrowright)} - \omega_{SQ}^{(\circlearrowleft)} = (E_{|1,\circlearrowright\rangle} - E_{|0,\circlearrowright\rangle}) - (E_{|1,\circlearrowleft\rangle} - E_{|0,\circlearrowleft\rangle}) = 4\chi\frac{\varepsilon}{\omega_q} . \tag{5.57}$$

If the system is far from the symmetry point ($\omega_q \to \varepsilon$), Eq. (5.57) reduces to $4\chi = \frac{\Delta\omega_{\pm}^2}{2\omega_r - \omega_q}$, as in Eq. (5.53) at the symmetry point. From Eq. (5.57), the dc-SQUID resonance frequency is not affected by the qubit at its symmetry point. However, we are considering the system in the RWA, whereas the neglected terms in Eq. (5.47) and in Eq. (5.23) could lead to small modifications of Eq. (5.57), resulting in $\chi \neq 0$ at $f = 0.5$.
Considering an asymmetric dc-SQUID, i.e. $g_1 \neq 0$, it is possible to calculate the dispersive Hamiltonian with the same procedure used for the unbiased symmetric dc-SQUID case. The effective total Hamiltonian is, in this case,

$$\mathscr{H}_{eff}^{(tot)}/\hbar = \left[\omega'_{SQ} - \chi^{(1)}\sigma_z - \chi^{(2)}\left(a^\dagger a + 1\right)\sigma_z\right] a^\dagger a + \frac{\omega'_q - \chi^{(1)}}{2}\sigma_z\,, \tag{5.58}$$

where

$$\chi^{(1)} = \frac{g_1^2}{\omega_{SQ} - \omega_q}\,, \tag{5.59}$$

$$\chi^{(2)} = \frac{g_2^2}{2\omega_{SQ} - \omega_q}\,. \tag{5.60}$$

It is important to notice that, from Eq. (5.43) with $I_b \sim 0$, $g_1 \ll g_2$. Even though the effect of the system on the energy levels is small, it has a strong impact from the symmetry point of view. In fact, due to the presence of the JC terms, Eq. (5.58) shows no continuous symmetries; thus it is not possible to divide the total Hilbert space in subspaces, but the eigenstates can still be found numerically.
Consequently, it is demonstrated that the total Hamiltonian can be described as the sum of the qubit Hamiltonian, a resonator Hamiltonian and a qubit-resonator coupling Hamiltonian. Furthermore, it is shown that, under the approximation of low coupling, a dispersive Hamiltonian can be defined and, from that, the dispersive shift on the resonator is found. Moreover, the resonator frequency shift depending on the qubit state is derived from both a semi-classical and a quantum mechanical point of view. The PCR is shown to be decoupled from the flux qubit by tuning the applied external field in the SQUID. This feature is very useful in quantum annealing routines, as it decouples the qubit from the readout noise. In the end, differences between the Hamiltonians based on a symmetric and an asymmetric dc-SQUID resonator are shown and discussed.

6

Persistent current readout: Experiments

LUCA COZZOLINO, ELIA BERTOLDO, P. FORN-DÍAZ

Building on the results presented in Ch. 5, the first experimental results obtained on the persistent current readout (PCR) were presented in this chapter. In Sec. 6.1, the chip design is introduced, in which, as discussed in Sec. 5.1, the considerations regarding the dc-SQUID resonator and its back-action on the qubit are taken into account. Then, in Sec. 6.2, the characteristics of the fabricated chip are presented, including a discussion regarding the differences with respect to the device design. In Sec. 6.3, we present the CPW spectroscopy measurements, whereas in Sec. 6.4, the focus is on the SQUID resonator signal. In Sec. 6.5, we discuss the effects of the qubit presence on the dc-SQUID resonator transmission and the proof of concept of the PCR.

Several chips have been fabricated along the duration of this thesis. The results presented in this chapter have been obtained on a chip fabricated by QuantumWare, thanks to the support of Qilimanjaro Quantum Tech.

The details about the design software, the fabrication processes, the experimental setup, and the measurement techniques are presented in Ch. 2.

6.1 Chip design

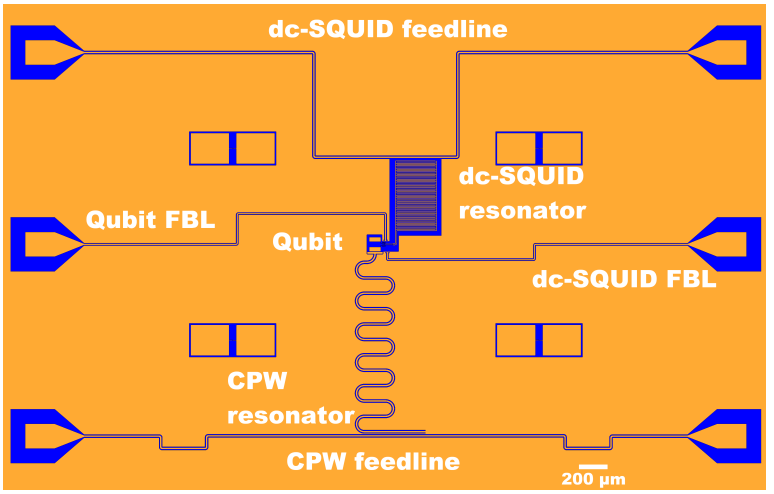

Figure 6.1: Entire chip design circuit to implement the PCR: a coplanar waveguide (CPW) resonator and a dc-SQUID resonator, both coupled to the same qubit.. In the top part, a feedline is capacitively coupled to the dc-SQUID resonator finger capacitor. In the bottom part, a CPW resonator is inductively coupled to its feedline. In the central part, two FBLs are coupled via mutual inductance to the qubit and dc-SQUID loops.

In this section, we detail the chip layout to implement the first generation of PCR. In order to demonstrate the results presented in Ch. 5 and compare them to the conventional dispersive readout method, two experiments are placed on the same chip using two dedicated feedlines, as shown in Fig. 6.1. In Fig. 6.2a, we show the dc-SQUID resonator, which is capacitively coupled to the top feedline of the device and inductively coupled to the qubit, in order to perform PCR measurements. In Fig. 6.2b, we show the coplanar waveguide (CPW) resonator capacitively coupled to the qubit to perform conventional dispersive readout measurements, as those presented in Sec. 3.4.
Since the same qubit is probed by both readout methods, the results can be compared and analyzed. Any difference in the operation of the readout methods is interesting for future applications, such as quantum annealing (Sec. 1.4).
It is important to state that this device is designed with a Nb optical layer and Al-based Josephson junctions, while the device in Sec. 3.4 was fully made of Al.
In order to analyze the device functionality, the main parts of the chip are separately discussed in the following subsections.

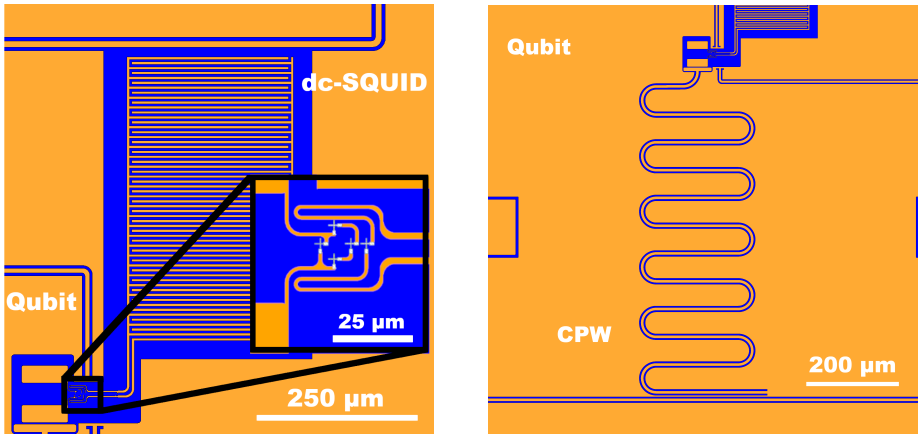

(a) (b)

Figure 6.2: Designs of the two different experiments for PCR benchmarking. (a) The PCR readout circuit with a zoom in on the qubit and dc-SQUID loops. (b) The CPW resonator readout circuit.

6.1.1 dc-SQUID resonator

As presented in Fig. 6.2a, the dc-SQUID resonator is composed by a dc-SQUID shunted by an interdigitated finger capacitor. In this first generation, the dc-SQUID is designed with symmetric Josephson junctions with critical current $I_c = 180\,\text{nA}$. For clarity, the effective circuit diagram of the dc-SQUID resonator is depicted in Fig. 6.3.

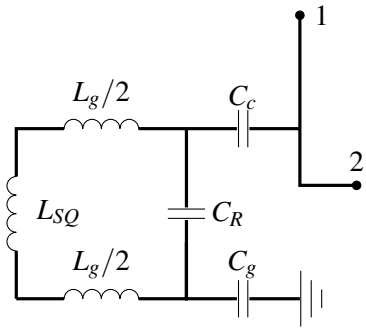

Figure 6.3: Effective circuit diagram of the dc-SQUID resonator. L_g is the total inductance of the branches, while L_{SQ} is the dc-SQUID inductance. C_g is the capacitance to the ground, whereas C_c is the capacitance to the feedline for S_{21} measurements.

The total inductance of the dc-SQUID resonator is given by the sum of the dc-SQUID inductance L_{SQ} and the geometric inductance L_g from the connecting arms to the finger capacitor. Hence, the resonance frequency is given by

$$\omega_{SQ} = \frac{1}{\sqrt{C_R(L_g + L_{SQ})}} \,. \tag{6.1}$$

The geometric inductance of the dc-SQUID resonator is simulated with FastHenry and it is found to be $L_g = 0.118\,\text{nH}$. Using the design value of I_c and taking into account Eq. (5.6), the SQUID inductance is calculated to be $L_{SQ} = 1.418\,\text{nH}$ at $f_{SQ} = 0$. These values impose a constrain on the capacitance C_R value, since it has to be designed to yield a resonance frequency within the bandwidth of the experimental setup ($4-8$ GHz). Using COMSOL, the finger capacitor is designed with $C_R = 0.72\,\text{pF}$, resulting in a maximum frequency of $\omega_{SQ}/2\pi = 5.755$ GHz at $f_{SQ} = 0$.

Another key parameter for the qubit's persistent current state detection is the mutual inductance M between the dc-SQUID and the qubit loop. Taking into account the junction dimensions, the dc-SQUID loop is placed in proximity to the qubit with a minimum distance of 1.5 μm, leading to $M = 10\,\text{pH}$.

In order to quantify the PCR efficiency, we define the frequency difference of the dc-SQUID resonator given by the two qubit persistent current states, $\Delta\omega_{SQ} = |\omega_{SQ}^{\circlearrowleft} - \omega_{SQ}^{\circlearrowright}|$. In Fig. 6.4, the simulated behaviour of the average dc-SQUID resonance frequency $\bar{\omega}_{SQ}/2\pi = (\omega_+ + \omega_-)/4\pi = \bar{\nu}_{SQ}$ and the difference in the dc-SQUID frequencies due to the two qubit states $\Delta\omega/2\pi = |\omega_+ - \omega_-|/2\pi = \Delta\nu_{SQ}$ are shown with respect to f_{SQ}. We find that the dc-SQUID resonator measurable frequency is in the range of $4-5.755$ GHz with f within -0.36 to 0.36.

Recalling Eq. (5.8), the flux in the qubit loop is proportional to the flux in the dc-SQUID, thus it is key to design the dc-SQUID loop area A_{SQ} with the correct proportion with respect to the qubit loop area A_q. For this reason, the design of the qubit and the dc-SQUID loop areas must satisfy the following: to have the average dc-SQUID frequency $\bar{\nu}_{SQ}$ within the setup bandwidth, the frequency shift $\Delta\nu_{SQ}$ large enough to distinguish the two qubit states, and the qubit to be in its sweet-spot. Since $\Phi_{SQ}/A_{SQ} = B = \Phi_q/A_q$, with Φ_{SQ} (Φ_Q) the magnetic flux in the dc-SQUID (qubit) loop, we impose

$$\frac{f_q}{A_q} = \frac{f_{SQ}}{A_{SQ}} \longrightarrow A_{SQ} = A_q \frac{f_{SQ}^*}{f_q^*} = 5.4 A_q$$

where $f_q^* = 0.5$ and $f_{SQ}^* = 2.7$ (see Sec. 5.1). To understand the reasons why the dc-SQUID working point is chosen to be 2.7, some considerations have to be made. From Fig. 6.4, it is clear that the sensitivity of the dc-SQUID is higher as

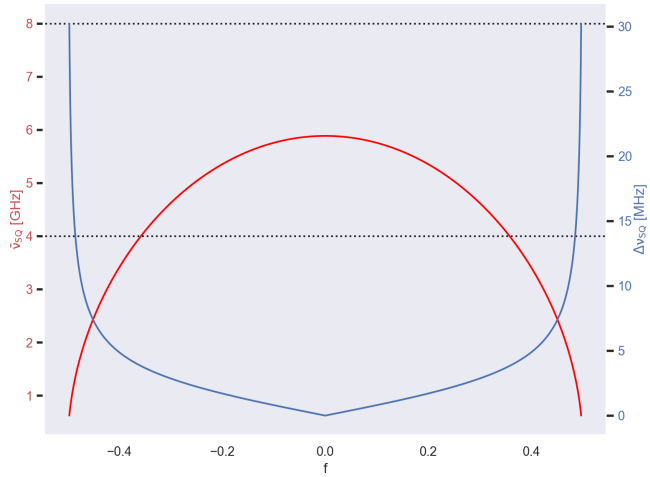

Figure 6.4: Simulated behaviour of $\bar{\nu}_{SQ}$ (in red) and $\Delta\nu_{SQ}$ (in blue) with respect to f_{SQ}. In this plot, $M = 10\,\text{pH}$ and $I_p = 100\,\text{nA}$ are assumed. The dotted lines represent the setup bandwidth limits.

$f_{SQ} \to \pm 0.5$, since $\Delta\omega \to \infty$. However, $\omega_{SQ} \to 0$ at $f \to 0.5$, i.e. the dc-SQUID resonance frequency falls outside of the setup bandwidth. Moreover, since we are interested in studying the dc-SQUID resonator response around the qubit sweet spot, the SQUID resonance frequency needs to be higher than 4 GHz to perform a flux sweep around the qubit working flux. Choosing a too large slope of $\Delta\omega_{SQ}$ vs. f is not convenient as the sensitivity to flux noise would increase. For these reasons, the working point of the dc-SQUID is chosen to be $f^*_{SQ} = n \pm 0.3$. Later, for fabrication convenience, n is chosen to be 3, thus $f^*_{SQ} = 3 - 0.3 = 2.7$. In Fig. 6.5, the first 4 periods of the dc-SQUID resonance and the working point of the dc-SQUID resonator where the qubit is at the sweetspot are shown. Figure 6.5 indicates the dc-SQUID resonator frequency $\bar{\nu}^*_{SQ} = 4.622\,\text{GHz}$ at the working point. At the same flux bias, the frequency shift due to the qubit state is calculated to be $\Delta\nu^*_{SQ} = 2.86\,\text{MHz}$, which is measurable with conventional cQED methods.

6.1.2 Coplanar waveguide resonator readout

As mentioned in the introduction of this section, a linear CPW resonator is placed in the lower part of the device to perform the conventional cQED dispersive readout measurements.
To compare the different readout properties of the two methods, the two resonators are designed with similar resonance frequencies at the operating SQUID flux. As

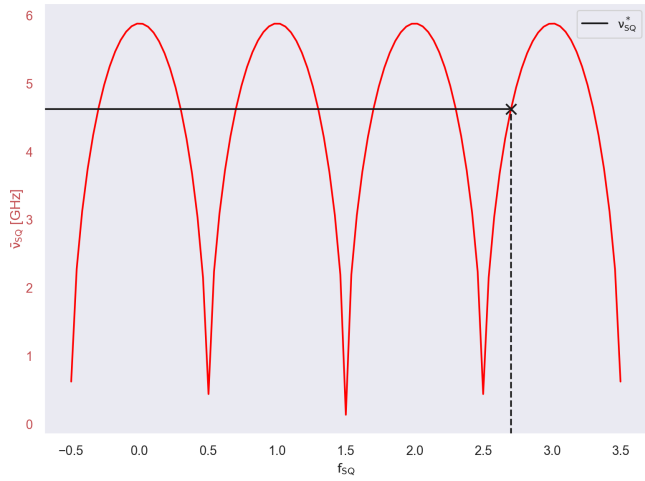

Figure 6.5: Four periods of the average frequency of the dc-SQUID resonator. The dashed lines indicate the working point, $f = 2.7$, $\bar{\nu}^*_{SQ} = 4.622$ GHz, where the qubit is expected to be in its symmetry point.

for the single-qubit experiment presented in Ch. 3, the CPW resonator is chosen to be a quarter-wave resonator, to capacitively couple to the qubit. Thus, recalling Eq. (3.15), the resonance frequency is given by

$$\nu_{CPW} = \frac{c}{\sqrt{\varepsilon_{eff}}} \frac{1}{4l} , \tag{6.2}$$

the length $l = 5265.81\,\mu$m is chosen to yield a frequency close to $\nu^*_{SQ} = 4.622$ GHz. As in Sec. 3.3, the chip is designed on Si, therefore $\varepsilon_{eff} \approx 6.255$. Starting from the design in Fig. 3.5b, the length is adjusted by increasing the segments between the windings and the calculated frequency is $\nu_{CPW} = 4.748$ GHz. In Fig. 6.2b, the final design of the CPW is presented. Then, the CPW resonator is simulated in Sonnet, under the assumption of a lossless metal without taking into account the effect of the kinetic inductance. This choice was made assuming the kinetic inductance contribution to be negligible, due to the thickness (200 nm) of the device. The simulated transmission is characterized by a resonance frequency $\nu_{sim} = 5.559$ GHz and an internal quality factor $Q = f/\Delta f \approx 6700$, in a first approximation. This value is different from the estimate in Eq. (6.2), since it returns the loaded resonator frequency. The value of ν_{CPW} is higher than the dc-SQUID resonance at the working point. Nevertheless, ν_{SQ} has to be fixed thanks to a local magnetic field, generated by a dedicated FBL, to perform qubit spectroscopy. Hence, it can be fixed close to ν_{CPW}, in order to compare results of the two readout methods at the same frequency.

6.1.3 Flux qubit circuit

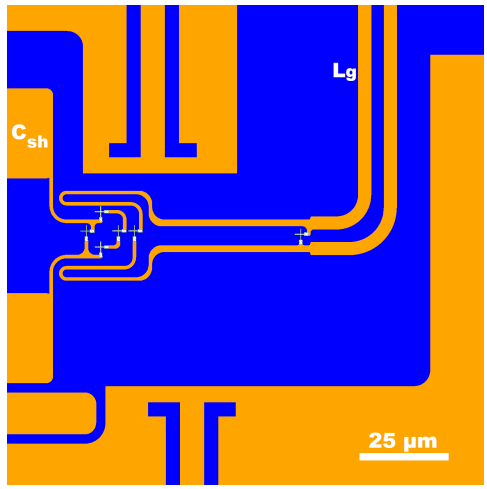

Figure 6.6: Qubit and dc-SQUID loops. The qubit α junction is directly connected to the shunt capacitance. The dc-SQUID loop surrounds part of the qubit loop and is connected to the dc-SQUID shunt capacitance through a geometrical inductance L_g.

As in Sec. 3.4, the qubit is designed as a four-junction flux qubit with a shunt capacitor. As shown in Fig. 6.6, the qubit loop is surrounded by the dc-SQUID, which is $1.5\,\mu$m at its closest point to the qubit.
The big qubit Josephson junctions are designed with critical current $I_c = 180$ nA, while the small Josephson junction is designed to have $\alpha = 0.55$, thus the critical current is $I_\alpha = 100$ nA.
The qubit shunt capacitor is designed to lead to a qubit frequency lower than CPW resonance $\nu_{CPW} = 5.559$ GHz.
Following the discussion in Sec. 3.4, in order to simulate the qubit spectrum, we have to calculate the effective shunt and coupling capacitance, given the complete capacitance network, shown in Fig. 6.7a. Although the circuit in Fig. 6.1 is more complex than the one described in Sec. 3.4, the same approach to the capacitors network is applied and presented in Sec. 6.1.4. Once the capacitances are designed, a COMSOL simulation is performed to obtain the capacitance matrix, which is used to calculate the effective shunt and coupling capacitances. Then, the qubit spectrum is simulated. By iterating this process, the parameters for the capacitance designs are obtained. The qubit spectrum with the final parameters is presented in Fig. 6.11.

6.1.4 Capacitance network

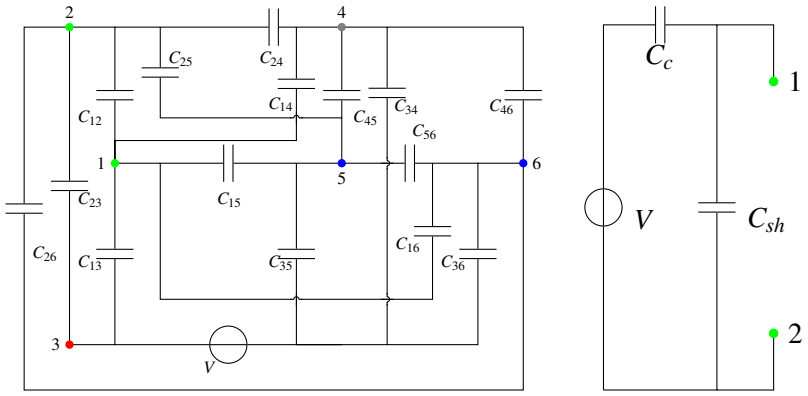

Figure 6.7: Capacitor circuits diagram. In (a), the whole system is described as a capacitor network with the voltage V on the CPW (node 3). In (b), the desirable circuit diagram is depicted.

As shown in Fig. 6.6, the qubit loop is directly shunted by a parallel-plate capacitor. Nevertheless, as was shown in Sec. 3.3, it is the entire capacitance network that determines the qubit response. By analysing such a network, it is possible to obtain an effective shunt capacitance C_{sh} and an effective coupling capacitance C_c, as defined and shown in Figure 6.7b. In other words, in order to simulate the qubit response it is necessary to reduce the circuit in Fig. 6.7a to the diagram in Fig. 6.7b, in which C_{sh} and C_c are the only effective capacitances involved.
The first step to reduce the capacitor network is to define its nodes, which are the plates of the qubit shunt capacitor (1,2, in green), the CPW resonator conductor (3, in red), the surrounding ground plane (4, in gray) and the two finger branches of the SQUID shunt capacitor (5,6, in blue). Thus, the capacitor network from the chip in Fig. 6.1 is described by the circuit diagram in Fig. 6.7a, in which all nodes are connected to each other by a capacitor C_{ij}, where i and j are the node labels. It is important to point out that, for the capacitance network analysis, the voltage is placed in node 3, which means that we are measuring through the CPW resonator. In the case of measuring through the SQUID-resonator, the voltage should be placed between ports 5 and 6. Nevertheless, due to the inductive nature of the coupling between the qubit and the dc-SQUID, the coupling capacitance would be negligible. It can be shown that, in the case of measuring through the dc-SQUID resonator, $C_{sh} = C_{Th}$.
For clarity, in Fig. 6.8 the circuit in Fig. 6.7a is represented as a hexagon in which

all the vertices are connected and the voltage is neglected.

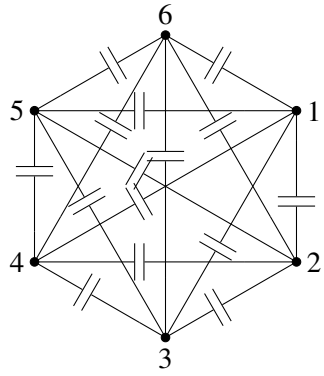

Figure 6.8: The circuit diagram in Fig. 6.1 is here rearranged in a hexagon shape.

It is possible to reduce the complexity of this diagram by applying the star-mesh transformation [97, 98], which allows to delete a node by redefining the remaining capacitances. Here, in Fig. 6.9, this technique is applied to node 6.

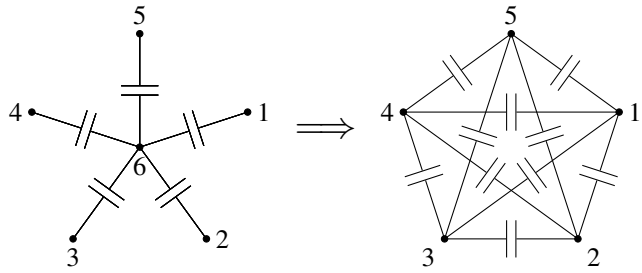

Figure 6.9: Star-mesh transformation applied to node 6 .

After the transformation, each remaining node, from 1 to 5, is connected by two capacitances in parallel: C_{ij} and C'_{ij}, with $i, j = 1 \dots 5$. The new capacitance C'_{ij} is defined as follows

$$Z'_{ij} = Z_{i6} Z_{j6} \sum_{k}^{5} \frac{1}{Z_{k6}} \Longrightarrow C'_{ij} = \frac{C_{i6} C_{j6}}{\sum_k C_{k6}} \,. \tag{6.3}$$

In this way, the circuit diagram in Fig. 6.8 can be reduced to a fully connected pentacle, with the capacitance between nodes i and j defined as $C''_{ij} = C_{ij} + C'_{ij}$. This process can be iterated to reduce the entire capacitor network to a single capacitance between nodes 1 and 2, which is the Thévenin capacitance C_{Th}.
By applying the Kirchhoff law to the circuit in Fig. 6.7a, it is possible to define the Thévenin voltage V_{Th}. Thus, Fig. 6.7a is reduced to the circuit diagram in Fig. 6.10.

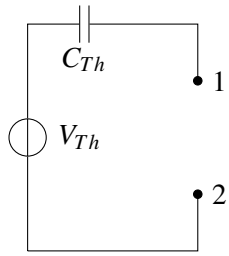

Figure 6.10: Thévenin reduction of the circuit in Fig. 6.7a.

Since we are interested in finding the qubit shunt and the coupling capacitance, it is necessary to find a relation between the Thévenin reduction in Fig. 6.10 and the desired circuit in Fig. 6.7b. Hence, applying the Thévenin theorem to Fig. 6.7b, we find the relations

$$C_{Th} = C_{sh} + C_c \ , \qquad V_{Th} = \frac{C_c}{C_{sh} + C_c} V \ ,$$

where V is the voltage in Fig. 6.7b.
With these results, it is possible to extrapolate the capacitances and design the chip with the optimal parameters for readout. The final design parameters for the qubit are presented in Table 6.1 and the expected spectrum is depicted in Fig. 6.13.

C_{sh}	4.0 fF
C_c	0.3 fF
$\Delta/2\pi$	4.878 GHz
I_p	69.94 nA

Table 6.1: Qubit design values.

As said above, if the readout is performed through the dc-SQUID resonator, the coupling capacitance is negligible ($C_c \approx 10$ aF) and $C_{sh} = C_{th} = 4.3$ fF.

6.1.5 Flux biasing and test structures

As discussed in Sec. 5.1.1, it is necessary to design a flux bias line (FBL) to locally apply a magnetic field to the SQUID in order to mitigate the dc-SQUID back-action to the qubit. Moreover, the presence of a FBL for the dc-SQUID can help in performing more precise measurements. In fact, if a global magnetic field is applied, a local field on the SQUID-resonator can fix its frequency while performing a sweep of the qubit frequency with the global flux. For these reasons, two FBLs are placed in the center of the chip and reach the hole in the ground plane in which we placed

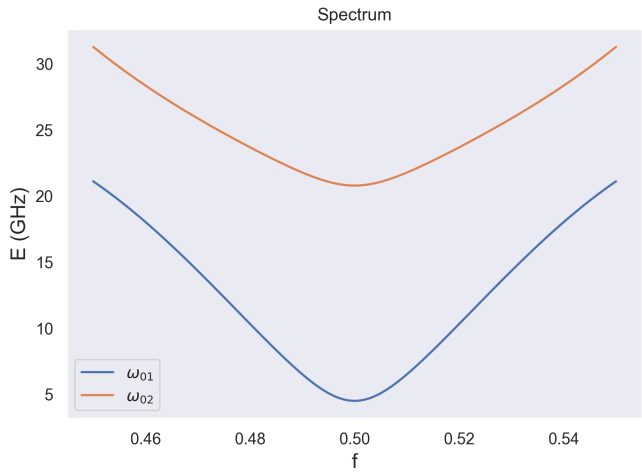

Figure 6.11: The simulated qubit spectrum with parameters presented in Table 6.1, where $\Delta/2\pi = 4.878$ GHz.

the qubit and the dc-SQUID loops. The FBLs are designed as shorted 50 Ω CPWs that work as flux antennas.
Finally, test structures are placed on the chip, consisting of single Josephson junctions, with the dimensions of the qubit α-junction, connected on both sides to a lead. These junctions are used for the room temperature (RT) estimate of the junction critical current. These structures are fundamental to validate the chip before installing it in the cryostat.

6.2 Device description

In this section, we present the experimental results obtained from the device presented in Sec. 6.1. Details on the measurement techniques and the experimental setup are presented in Ch. 2.
The chip in Fig. 6.12 is a Si substrate with a Nb optical layer of nominal thickness 200 nm, while the Josephson junctions are $Al/AlO_x/Al$ junctions. A magnification of the qubit and the dc-SQUID loops is showed in Fig. 6.12b.
To obtain a prediction of the dc-SQUID resonance frequency range and the qubit gap, the critical current is estimated at room temperature, probing the test structures present on the chip. The results showed that the average critical current of the small junctions was $41 \pm 9\%$ higher than the designed value. Since we have no direct information on the critical current of the qubit big junctions, it is necessary to calculate the current density J_c^{meas} to provide an estimate. Thus, using ImageJ [99],

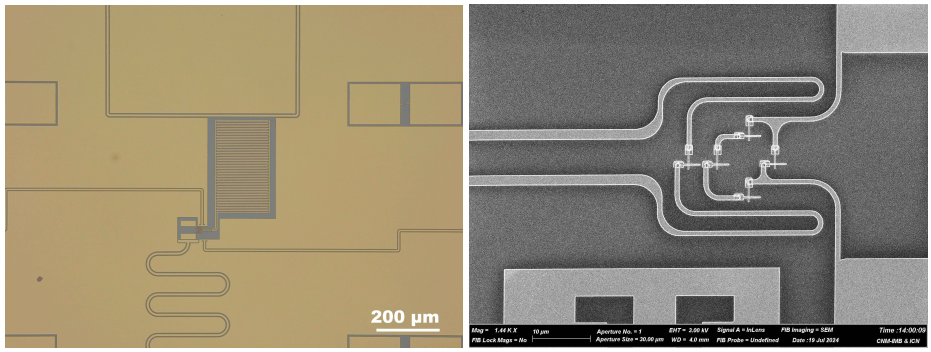

(a) (b)

Figure 6.12: In (a), the microscopic image of the device is presented. In (b), the SEM image of the dc-SQUID and qubit loop. The brighter details are the Al Josephson junctions.

the effective dimensions of the junctions are measured from SEM images.
The critical current I_c^{meas} for the big junction is calculated as $I_c^{meas} = A^{meas} J_c^{meas}$, with the current density $J_c^{meas} = 3.13 \pm 0.23\ \mu\text{A}/\mu\text{m}^2$ obtained from the test Josephson junctions, whereas the designed value was $J_c^{exp} = 2.3\ \mu\text{A}/\mu\text{m}^2$. The characteristics of the Josephson junctions are summarized in Table 6.2.

Junction	$A^{exp}\,(\mu\text{m}^2)$	$A^{meas}\,(\mu\text{m}^2)$	$I_c^{exp}\,(\text{nA})$	$I_c^{meas}\,(\text{nA})$
Big junction	0.0784	0.0764 ± 0.0009	160	$239 \pm 18^*$
Small junction	0.0437	0.0450 ± 0.0015	100	141 ± 9

Table 6.2: Expected and measured values of the characteristics of the Josephson junctions. The symbol "*" stands for extrapolated value, i.e. not measured.

Hence, it is possible to simulate the expected qubit spectrum with the parameters defined in Table 6.2. The result is presented in Fig. 6.13, returning the values reported in Table 6.3. Since $\alpha = 0.59$ instead of $\alpha_{des} = 0.55$, the estimated qubit persistent current turned out higher than the designed value, namely $I_p = 120.53$ nA, leading to a qubit frequency $\Delta/2\pi = 3.01$ GHz lower than the designed value. Nevertheless, the predicted qubit frequency, which is under the CPW resonator frequency, allows to perform the conventional readout measurements. In addition, the higher qubit persistent current leads to a larger shift in the PCR frequency, implying a better resolution in the qubit state detection.

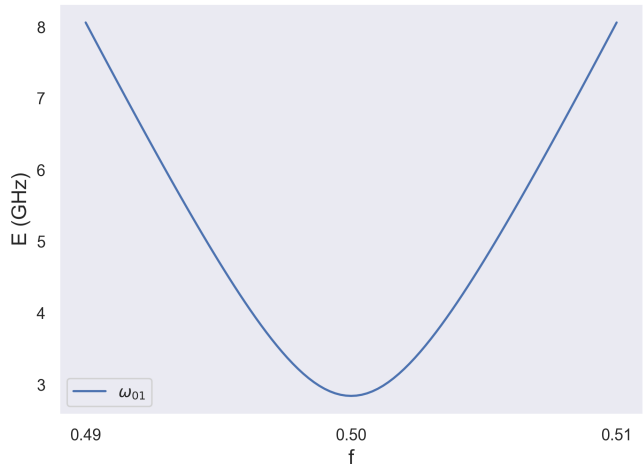

Figure 6.13: Qubit spectrum expected from the RT estimate of I_c.

α	0.59
$\Delta/2\pi$	3.01 GHz
I_p	120.53 nA

Table 6.3: Qubit parameters extracted from the room temperature estimation of I_c, with $\Delta/2\pi = 3.01$ GHz and $I_p = 120.53$ nA

Similarly, the expected response of the dc-SQUID resonator is calculated and presented in Fig. 6.14. With the measured values of I_c presented in Table 6.2, at the working point, the frequency of the dc-SQUID resonator is $\nu_{SQ} = 4.628$ GHz, whereas the expected dc-SQUID frequency difference between the two qubit states of $\Delta\nu_{SQ} = 3.27$ MHz. Although the predicted $\bar{\nu}_{SQ}$ is higher than the designed value, it is still within the setup bandwidth. Conversely, the expected frequency of the dc-SQUID resonator is higher than the ν_{CPW}. Eventually, the predicted $\Delta\nu$ is larger, leading to a better resolution of the qubit state detection.

6.2.1 Sample packaging

As explained in Sec. 2.3, the chip is mounted in a Cu sample box, placed in a Bluefors SD dilution fridge and connected to the external environment through coaxial cables.
Mounted on the top of the sample box, a superconducting coil generates a global magnetic field on the chip. The coil is driven through a voltage/current source with a π-filter that is interposed between the source and the sample.

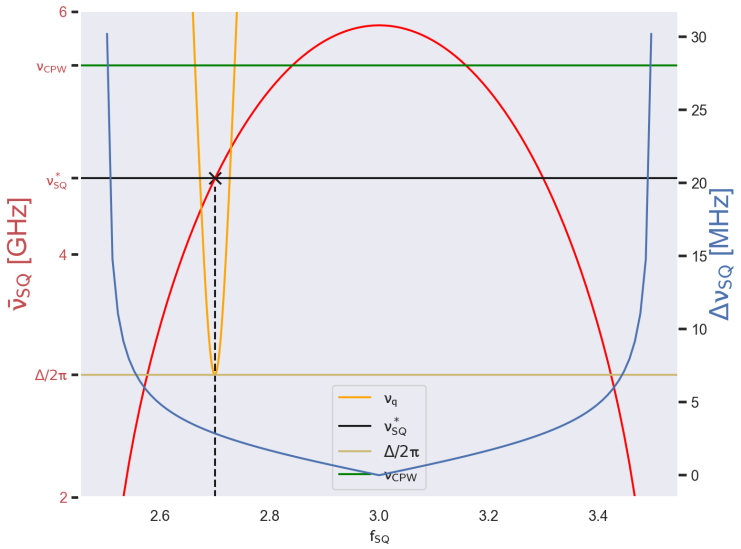

Figure 6.14: Expected dc-SQUID response at the working point with the measured critical current in Table 6.2. In orange, the qubit frequency ν_q is shown as a function of f_{SQ}.

6.3 CPW resonator transmission

Since the CPW resonance frequency is independent of the magnetic field, it is, in principle, a more direct way to identify the qubit presence by seeing avoided-level crossings between the resonator and the qubit, as in Sec. 3.4. Hence, the qubit can be first characterized through the CPW resonator by performing the usual dispersive measurement presented in Sec. 3.4, and then, in a second stage, through the PCR.
As a first step to characterize the qubit, it is fundamental to find and optimize the CPW resonance. Once the resonance is found and the transmission signal is optimized, it is possible to perform a sweep of the global magnetic flux to detect the evidence of the qubit presence, i.e. the avoided-level crossing.
Following such a procedure, a VNA scan through the CPW resonator feedline is performed. In Fig. 6.15a the transmission of the CPW resonator is shown with zero applied magnetic field. The resonance frequency is measured to be $\nu_{CPW} = 5.118\,\text{GHz}$, thus there is a large difference of $\approx 400\,\text{MHz}$ between the measured CPW frequency and the simulated value.
In order to find the qubit-induced avoided-level crossings, as in Sec. 3.4, the resonator transmission measurement is repeated for different values of the driving current applied to the superconducting coil. This measurement is shown in Fig. 6.15b. Here,

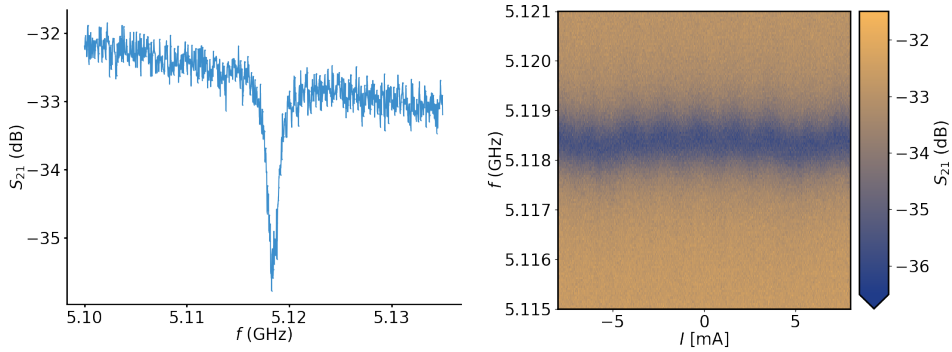

(a) (b)

Figure 6.15: In (a), the CPW resonator transmission at zero field. In (b), the CPW resonator transmission as function of the applied coil current. Given the low signal level from the resonator, the system is underdamped.

the CPW resonator transmission is measured in the interval -8 to 8 mA with a fixed step of 20 μA. Unlike Fig. 3.10, in Fig. 6.15b there is no sign of avoided-level crossings, but a weak modulation of the transmission with the flux can be clearly discerned. The small oscillations in Fig. 6.15b seem to have a 2 mA period. As discussed in Sec. 6.5, the dc-SQUID period is also ~ 2 mA, thus the oscillations in the CPW resonance could be caused by a direct coupling of the the two readout resonators. In Fig. 6.16, the correspondence between the oscillations in the CPW transmission and the dc-SQUID transmission is shown.

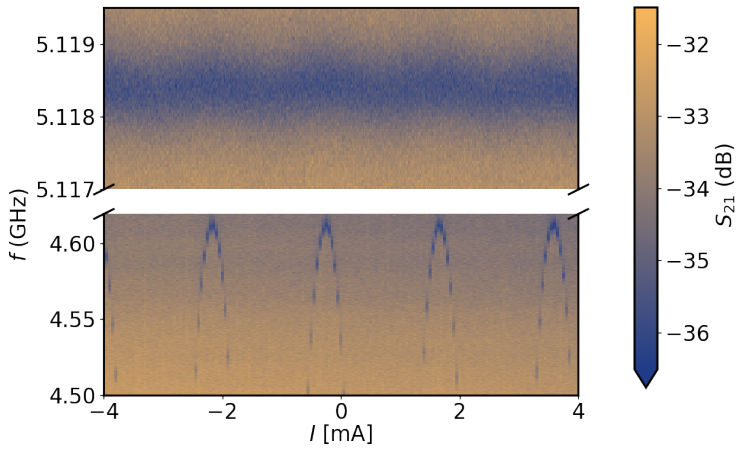

Figure 6.16: Correspondence between the CPW transmission oscillations (upper plot) and the dc-SQUID transmission (lower plot).

Even though the absence of avoided-level crossing seems to be a clear evidence of no qubit presence below the resonator frequency, it is also true that the CPW resonator is underdamped, as seen in Fig. 6.15a and, therefore, giving a very poor signal to detect any qubit response. A possible explanation for such a different Q factor from the expected value can be related to the impedance mismatch due to the wrong spacing in the CPW design, which is the same for the Al resonator designed in Sec. 3.3, whereas the fabricated chip is made of Nb. Another effect of this design error is noticeable in the resonance frequency difference between the expected values and the measured ν_{CPW}. Under these circumstances, it is not possible to obtain any information about the qubit from the CPW resonator.

6.4 dc-SQUID resonator

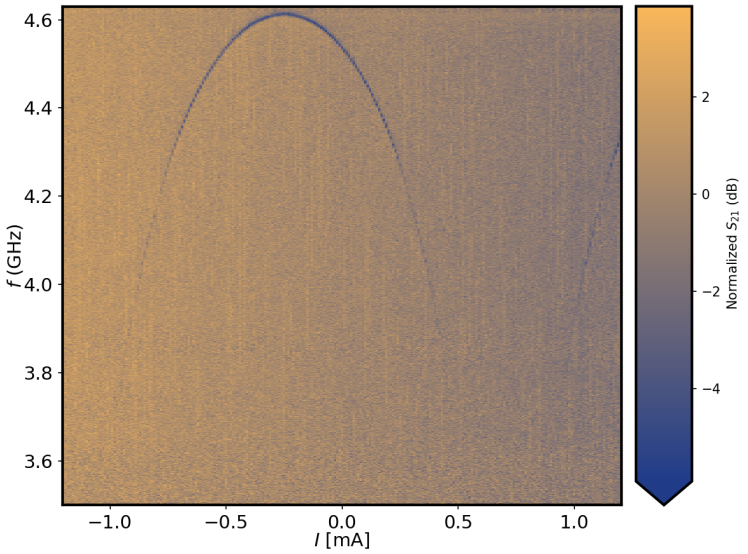

Figure 6.17: dc-SQUID transmission between −1 mA and 1 mA

The same procedure described in Sec. 6.3 is performed on the dc-SQUID transmission line. In Fig. 6.17, the variation of the dc-SQUID frequency with respect to the applied magnetic field is shown. The first to notice is that the maximum frequency, $\nu_{SQ}^{max} = 4.61$ GHz, is more than 1 GHz lower than the designed value, and almost 2 GHz below the frequency expected from the test junction measurements. A possible explanation to this discrepancy is that the effective dc-SQUID shunting capacitance is larger than the estimated value, possibly due to the contribution of extra thickness in the Nb device. Another possibility is the contribution of the capa-

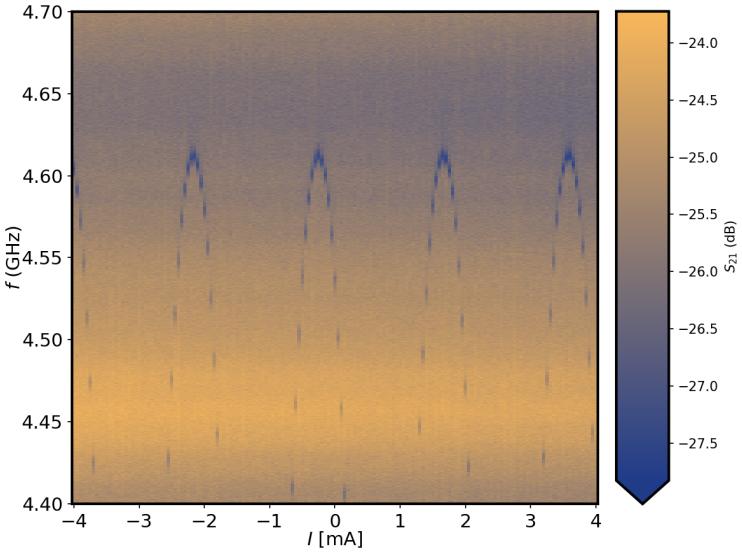

Figure 6.18: dc-SQUID transmission between −4 mA and 4 mA

citance network to the effective dc-SQUID shunting capacitance C_{SQ}. It is possible that the whole capacitance network leads to a larger effective C_{SQ}. This possibility was firstly discarded during the design process due to the large difference between the finger capacitor C_{SQ}, which is ~ 1 pF, and the rest of capacitances, in the order of few fF. A thicker film than expected may lead to a bigger contribution from the network. For this reason, the extra thickness contribution is the most probable cause of the low dc-SQUID frequency.

Even though the resonance frequency is expected to go down to zero at $f_{SQ} = 0.5$, as shown in Fig. 6.4, in Fig. 6.17 it is not possible to clearly measure the transmission of the dc-SQUID resonator below ≈ 4 GHz due to limitations in our experimental setup. As the frequency approaches the circulator cut-off frequency 4 GHz, the SNR diminishes until the resonator transmission is indistinguishable from the background noise. There is also a possible effect of dissipation from the juncitons. As the effective dc-SQUID I_c becomes smaller as $f_{SQ} \to 0.5$, the resonator internal quality factor decreases, and so does the signal, as the resonator becomes progressively more underdamped.

As in the case of the CPW resonator, the same measurement presented in Fig. 6.17 is performed on a larger current span, in order to find any avoided level-crossing. In Fig. 6.18, we present a measurement of the dc-SQUID resonator transmission for different values of the driving current applied to the superconducting coil. Clearly, the measurement does not show any avoided-level crossing. In Sec. 6.1, it

is stated that the areas of the loops are designed to have $f_q^* = 0.5$ while $f_{SQ}^* = 2.7$. Thus, a possible explanation for the lack of avoided-level crossings is that the dc-SQUID resonance frequency is below the setup cut-off frequency at f_{SQ}^*, since the dc-SQUID has a lower maximum frequency. Moreover, the qubit is believed to display a minimum frequency $\nu_q = 2.895$ GHz lower than the simulated value, $\nu_q^{sim} = 4.581$ GHz, and a higher persistent current, $I_p = 102.97$ nA, due to the untargeted areas and current density of the Josephson junctions. This reinforces the possibility that any avoided level-crossing takes place below the cut-off frequency. Furthermore, trapped magnetic fluxes in proximity of the two loops can move differently the qubit and the dc-SQUID responses to the external magnetic field, thus additionally moving the operational point. In principle, the working point can be re-adjusted using a local magnetic field generated by a DC current through one of the two FBLs. Nevertheless, the field generated by the FBL was insufficient to move the qubit symmetry point in correspondence to $\nu_{SQ} > 4$ GHz. Moreover, if there are errors in the capacitance simulation, as suggested by the dc-SQUID measured resonance frequency, it is possible that the effective shunt capacitance of the qubit is lower than the simulated value, leading to a higher qubit frequency, where it may not cross the dc-SQUID resonator.
Although there is no sign of the qubit presence in spectroscopic measurements conducted so far, an indirect way to detect it is discussed in the next section.

6.5 Qubit signal

Following Sec. 5.1, on either side of the qubit symmetry point, the dc-SQUID resonator feels two different values of the qubit flux depending on the qubit persistent current

$$\Phi_I^{\pm} = \Phi_{SQ} \pm M I_p \ .$$

Hence, the qubit persistent current state can be detected by detecting a change in the periodicity of the dc-SQUID.
Such a period can be determined by measuring the dc-SQUID transmission at a fixed value ν'_{SQ} while sweeping the external magnetic flux f_{SQ}. When the SQUID frequency coincides with the measured frequency, $\nu_{SQ} = \nu'_{SQ}$, the dc-SQUID transmission has a dip, otherwise it is at the transmission baseline. In this way, dips in transmission return the flux positions for which $\nu_{SQ} = \nu'_{SQ}$. Given the cosine-like SQUID frequency response as function of flux, every flux period will show two dips when scanning the flux while monitoring the transmission of a weak probe at a fixed frequency below the SQUID maximum frequency. If within one period the qubit crosses the symmetry point, the qubit will generate a sudden change of flux

of $\pm 2MI_p$, the sign will be given by the geometry of the circuit. Let's assume the distance between two consecutive values of the SQUID frequency from consecutive periods to be T. If the qubit crosses the symmetry point between these two consecutive resonances, the period will change by $T \pm 2MI_p$. Fig. 6.19 shows a schematic of the case where the qubit crosses the sweet spot where $f_{SQ} = 0.5$ and the change in periodicity is assumed to be $-2MI_p$. The dashed line represents the fixed value ν'_{SQ}.
From now on, we are going to refer to this measurement as "period measurement".

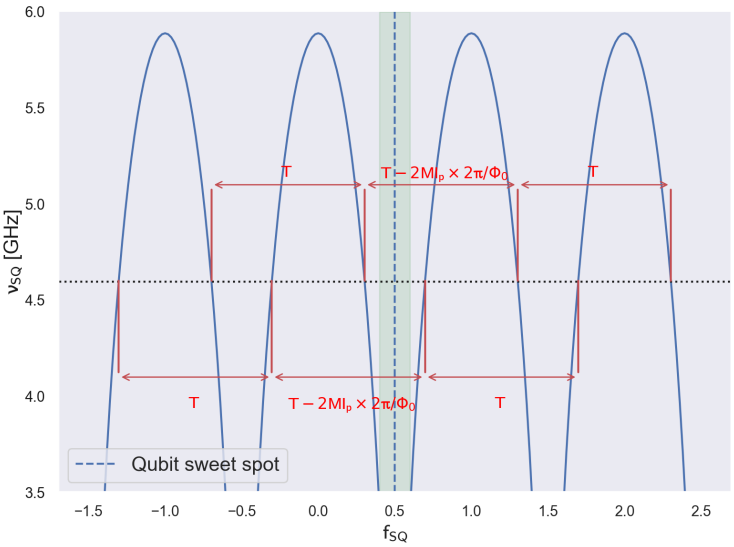

Figure 6.19: Periodicity of a dc-SQUID resonator transmission at a fixed frequency. The qubit symmetry point is assumed within the green band.

Figure 6.19 shows a measurement of the periodicity of the dc-SQUID resonances. Any dc-SQUID frequency could be used to perform a period measurement. Nevertheless, since we want to use the periodicity to detect the qubit, recalling Sec. 5.1 and Fig. 6.4, the maximum SQUID frequency cannot be used since the dc-SQUID resonator is uncoupled from the qubit. Also, we want a good SNR, thus we have to choose $\nu_{SQ} > 4.2$ GHz, which is the visible range in Fig. 6.17. For these reasons, the measurement in Fig. 6.20 is performed by fixing the frequency at 4.595 GHz.
In Fig. 6.20, the distances between alternate minima are annotated. We can divide the periods into two values: $T_-^{(volt)} = 204.6 \pm 0.8$ mV and $T_+^{(volt)} = 206.2 \pm 0.7$ mV. Here, the uncertainty of these averages is taken as $\sigma_{\bar{x}} = \frac{2\Delta x}{\sqrt{N}}$, where N is the total number of periods of each group and Δx is the deterministic uncertainty of the peak position, calculated as the average of the half width at half maximum (HWHM) of

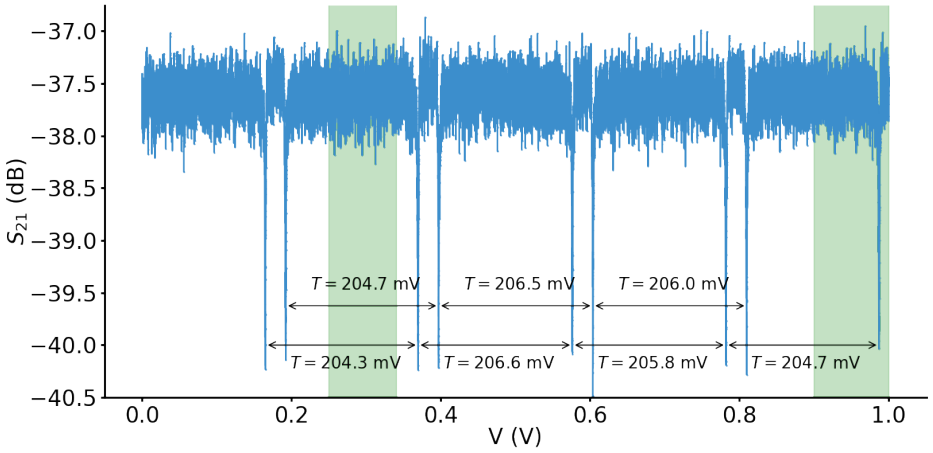

Figure 6.20: Period measurement between 0 V and 1 V. In the figure, the period T_+ and T_- are displayed. The qubit symmetry points are within the green bands.

the deeps. The two estimates are separated within the uncertainties, thus it can be stated that there are two different periods. Based on the locations where the period changes, the qubit symmetry point is expected to be in the green bands in Fig. 6.20. The estimate of the position of the qubit symmetry point cannot be more accurate, since with this measurement we can only observe the effect of the qubit presence between non consecutive dips.
Therefore, we can certify the qubit existence with the period measurement, even though we cannot determine its resonance frequency nor the exact position of the sweet spot. This result constitutes a proof of concept of the PCR. Yet the full demonstration remains to be completed in future devices with better adjusted parameters.

6.6 Outlook

The transmission spectra of the CPW and the dc-SQUID resonator have been presented. Since the CPW turned out to be underdamped due to a design flaw on the Nb chip, as shown in Fig. 6.15a, it is not possible to see any qubit evidence in frequency domain.
The next device generation is already been designed with a larger coupling surface between the CPW and the qubit shunt capacitor, and a proper coupling of the CPW resonator to the dedicated transmission line, so that $Q_{ext} \gg Q_{int}$. The new design proposed for the CPW is presented in Fig. 6.21.

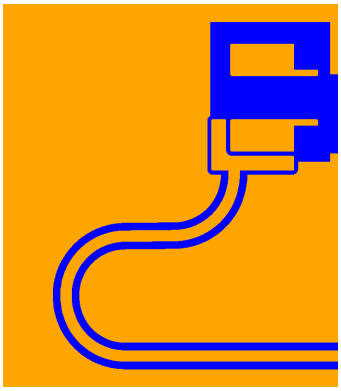

Figure 6.21: New CPW design for an enhanced coupling between the resonator and the qubit.

Furthermore, the presence of oscillations in the CPW spectrum provides evidence about the coupling between the linear resonator and the dc-SQUID. The interaction between the two readout system could impact the readout quality of both resonators. For this reason, it is fundamental to understand the origin of the possible coupling between the CPW and the dc-SQUID resonators, and minimize it.
Despite the design flaws and the off-target I_c values, the dc-SQUID behaves as expected: a resonator with a flux-dependent resonance frequency. Nevertheless, there is no avoided-level crossing and it is not possible to perform qubit spectroscopy, as was performed in Sec. 3.4 with a linear resonator. Still, the existence of two different values for the periodicity of the dc-SQUID resonance frequency is measured at a given flux range, indicating the presence of the qubit. This result constitutes a good starting point for the next generation of devices. Even if the present measurements do not permit the qubit to be characterized and to study the properties of this new readout method, the results shown prove the variation of the dc-SQUID resonance frequency depending on the qubit state, which is the main concept of the PCR.
For future iterations of the device, FBLs have to be designed with higher mutual inductance with the dc-SQUID and qubit loops. In this way, it is possible to move the working point along the dc-SQUID spectrum. This possibility is fundamental to decouple the dc-SQUID resonator from the qubit, a key element to scale this readout to a large-scale quantum processor.

7

Conclusions and further perspectives

The main aim of this thesis is to present a novel readout method for quantum annealing.
First, the flux qubit physics is described both for isolated qubit and the qubit-resonator system. In particular, the dispersive Hamiltonian of a qubit capacitively coupled to a readout resonator is shown. Starting from this result, a 8-flux qubit chip was designed and fabricated. The experimental results presented are encouraging, as $T_1 > 40\ \mu$s is demonstrated, despite the low estimation of T_1 at the qubit sweet spot and the decoherence time measured ($T_2 = 13$ ns) away from the sweet spot. In addition, the difficulties to perform quantum control measurements at low frequencies did not allow us to obtain information about the noise mechanisms and how this affects the coherence time of the qubit, thus more tests are needed. More iterations have to be made to reach the desired results. For this reason, a Nb-based generation is in fabrication process.
Moreover, different coupled systems were investigated in this thesis. Specifically, the cases of both a qubit galvanically coupled to a resonator and to another qubit were described. A good understanding of these interactions gives indications for new flux qubit and readout systems designs.
The results obtained on the galvanic coupling lead us to ideate a novel persistent current readout circuit. Such a circuit is composed of a dc-SQUID based resonator, with an inductance that depends on the qubit persistent current state. This persistent current readout (PCR) is analyzed both in the semiclassical and in the quantum framework. The Hamiltonian description of the PCR leaded to the definition of a dispersive-like Hamiltonian, which is presented and discussed. As an interesting result, the interactions between a flux qubit and a dc-SQUID based resonator can

be approximated to a two-photon Jaynes-Cummings mechanism, opening new intriguing scenarios for the study of the light-matter interaction. Moreover, the employment of a dc-SQUID returns the possibility to decouple the qubit from the readout circuitry, leading to an enhancement of coherence times, making the PCR particularly feasible for quantum annealing.
In order to test the advantages of the new system, a device design based on a single-qubit coupled inductively to the PCR and capacitively to the CPW is presented. Unfortunately, due to errors in the fabrication process, the measured parameters were away from the designed values, leading to the impossibility to compare the two readout methods and to characterize the qubit. Besides that, the variation of the dc-SQUID resonator period demonstrates the qubit presence, constituting the proof of concept of the readout mechanism proposed.
An interesting step forward to improve the results obtained so far could be to implement the PCR in a flip-chip architecture. By separating the dc-SQUID resonator circuitry from the flux qubit, it would be possible to minimize the dc-SQUID back-action and to separate the flux controls of the two loops, leading to a mitigation in crosstalk. These results should increase the coherence times of the flux qubit.
Moreover, the dc-SQUID resonator can be redesigned, including a shunt inductor to the dc-SQUID, in order to control I_b by adjusting the flux in the extra loop. In this way, it would be possible to mitigate the back-action of the dc-SQUID on qubit. Furthermore, it would be interesting to place a Purcell filter between the PCR resonator and the feedline. The Purcell filter screening, together with the possibility to decouple the PCR from the qubit, could lead to coherence times good enough to perform simple single-qubit annealing routines.
Nevertheless, the addition of a Purcell filter would increase the dimensions of the chip, which are already limited by the necessity of a large interdigitated finger capacitor. To overcome this limitation, the possibility to replace the finger capacitors with parallel plate capacitances, as the ones in ref. [100], should be taken into account to design multi-qubit chips for quantum annealing.

A

Fabrication recipe

A.1 Optical lithography recipes

- Ti prime: 2000 r.p.m. for 30 s
- Bake: 2 min at 120°C
- AZ nLOF 2020: 4000 r.p.m. for 1 min
- Pre-exposure bake: 1 min at 110°C
- Exposition: 840 $\mathrm{mJ/cm^2}$ with -2 defocus
- Post-exposure bake: 1 min at 110°C
- Development: 1 min in AZ 726 MIF + 10 s in DI water
- N_2 blow dry

A.2 Electron beam lithography recipe

- PMGI: 1000 r.p.m. for 1 min
- Bake: 5 min at 190°C
- CSAR62: 3000 r.p.m. for 1 min
- Bake: 1 min at 150°C

- Exposition 120 μm write field: 100 pA with 0.08 μs
- Exposition 600 μm write field: 2 nA with 1.5 μs
- CSAR62 development: 1 min in CSAR62 developer (AR 600-546) + 30 s CSAR62 stopper (AR 600-60) + 30 s in DI water + 30 s in IPA
- N_2 blow dry
- PMGI development: 55 s in PMGI developer (1:3.5 MR-351:H_2O) + 30 s in DI water + 30 s in IPA
- N_2 blow dry

B

Schrieffer-Wolff approximation

The system can be described by the following Hamiltonian:

$$\begin{aligned} \mathscr{H}_{tot} &= \mathscr{H}_0 + V \ , \\ \mathscr{H}_0 &= \omega_r a^\dagger a + \sum_k \omega_k \left|k\right\rangle \left\langle k\right| \ , \\ V &= \sum_{i,j} g_{ij} \left|i\right\rangle \left\langle j\right| (a^\dagger - a) \ . \end{aligned} \tag{B.1}$$

(B.2)

It is known that to obtain a dispersive Hamiltonian, one has to perturbatively expand in g Equation (B.1) with the Schrieffer-Wolff (SW) transformation:

$$\mathscr{H}' = U \mathscr{H} U^\dagger = e^S \mathscr{H} e^{-S} \ ,$$

with S is anti-hermitian, thus the SW is an unitary transformation [1]. Using the Baker-Campbell-Hausdorff formula:

$$\begin{aligned} \mathscr{H}' &= \mathscr{H} + [S, \mathscr{H}_{tot}] + \frac{1}{2}[S,[S,\mathscr{H}_{tot}]] + \dots \\ &= \mathscr{H}_0 + \{V + [S, \mathscr{H}_0]\} + \{[S,V] + \frac{1}{2}[S,[S,V]]\} + \dots \ , \end{aligned} \tag{B.3}$$

[1] Note that since S is anti-hermitian

$$U = e^S \longrightarrow U^\dagger = e^{S^\dagger} = e^{-S}$$

thus, using the Glauber's formula

$$UU^\dagger = e^S e^{-S} = e^{S+(-S)} e^{\frac{1}{2}[S,-S]} = 1$$

where it has been ordered them in terms of g. $\mathscr{H}_0$ is the diagonal part of $\mathscr{H}$ and $\mathscr{H}_v$ the off-diagonal.
Under this transformation, we are requesting that in the new Hamiltonian the off-diagonal terms have to be null to the first order. In operators terms:

$$[S, \mathscr{H}_0] = -V \,, \tag{B.4}$$

that can be put in Equation (B.3):

$$\mathscr{H}' = \mathscr{H}_0 + \frac{1}{2}[S, V] \,. \tag{B.5}$$

The generator S of such transformation can be find within few steps, as explained in [101].
First of all, we calculate the commutator η [2], defined as

$$\eta = [\mathscr{H}_0, \mathscr{H}_v] \,,$$

that in our case is

$$\begin{aligned}
\eta = [\mathscr{H}_0, V] &= \omega_r \sum_{i,j} g_{ij} \left([a^\dagger a, a^\dagger] - [a^\dagger a, a] \right) + \sum_{i,j,k} \omega_k g_{ij} \left(|k\rangle \langle k|i\rangle \langle j| - |i\rangle \langle j|k\rangle \langle k| \right) = \\
&= \omega_r \sum_{i,j} g_{ij} \left(a^\dagger + a \right) + \sum_{i,j} \left(\omega_i g_{ij} |i\rangle \langle j| - \omega_j g_{ij} |i\rangle \langle j| \right) \left(a^\dagger - a \right) = \\
&= \sum_{i,j} \left[g_{ij} \left(\omega_r + \omega_i - \omega_j \right) |i\rangle \langle j| \right] a^\dagger + \sum_{i,j} \left[g_{ij} \left(\omega_r - \omega_i + \omega_j \right) |i\rangle \langle j| \right] a \,.
\end{aligned} \tag{B.6}$$

From this result we can define S as a linear combiantion of the operators in Equation (C.4)

$$S = \sum_{i,j} A_{ij} |i\rangle \langle j| a^\dagger + \sum_{i,j} B_{ij} |i\rangle \langle j| a \,.$$

[2] This will ensure us an anti-hermitian operator, since it is a commutator of hermitian operator

$$[A, B]^\dagger = (AB - BA)^\dagger = (AB)^\dagger - (BA)^\dagger = B^\dagger A^\dagger - A^\dagger B^\dagger = BA - AB = -[A, B]$$

Thus,

$$
\begin{aligned}
[S,\mathscr{H}_0] &= \sum_{i,j}\Bigg[\omega_r A_{ij}[a^\dagger,a^\dagger a]\,|i\rangle\langle j| + \omega_r B_{ij}[a,a^\dagger a]\,|i\rangle\langle j| + \sum_k \omega_k A_{ij}\left(|i\rangle\langle j|k\rangle\langle k| - |k\rangle\langle k|i\rangle\langle j|\right)a^\dagger + \\
&\quad - \sum_k \omega_k B_{ij}\left(|i\rangle\langle j|k\rangle\langle k| - |k\rangle\langle k|i\rangle\langle j|\right)a\Bigg] = \\
&= \sum_{i,j}\left[-\omega_r A_{ij}\,|i\rangle\langle j|\,a^\dagger + \omega_r B_{ij}\,|i\rangle\langle j|\,a + A_{ij}\left(\omega_j-\omega_i\right)|i\rangle\langle j|\,a^\dagger - B_{ij}\left(\omega_j-\omega_i\right)|i\rangle\langle j|\,a\right] = \\
&= \sum_{i,j}\left[A_{ij}\left(\omega_j-\omega_i-\omega_r\right)|i\rangle\langle j|\,a^\dagger - B_{ij}\left(\omega_j-\omega_i-\omega_r\right)|i\rangle\langle j|\,a\right] = \\
&= -\sum_{i,j} g_{ij}\,|i\rangle\langle j|\left(a^\dagger - a\right). \qquad \text{(B.7)}
\end{aligned}
$$

From Equation (B.7), it can be obtained

$$A = -B = \frac{g_{ij}}{\omega_r+\omega_i-\omega_j} = c_{ij}$$

Putting this result together, it can be obtained

$$
\begin{aligned}
[S,V] &= \sum_{i,j}\sum_{k,l} c_{ij}g_{kl}\left[\left(|i\rangle\langle j|k\rangle\langle l| - |k\rangle\langle l|i\rangle\langle j|\right)\right]\left(a^{\dagger^2} + a^2 - aa^\dagger - a^\dagger a\right) = \\
&= -2\sum_{i,j} c_{ij}g_{ji}\left(|i\rangle\langle i| - |j\rangle\langle j|\right)\left(a^\dagger a + \frac{1}{2}\right) = \qquad \text{(B.8)} \\
&= -2\left(\sum_{i,j} k_{ij}\,|i\rangle\langle i| - \sum_{i,j} k_{ij}\,|j\rangle\langle j|\right)\left(a^\dagger a + \frac{1}{2}\right) = \\
&= -2\sum_{i,j}\left(k_{ij}-k_{ji}\right)|i\rangle\langle i|\left(a^\dagger a + \frac{1}{2}\right) = \\
&= -2\sum_i \chi_i\,|i\rangle\langle i|\left(a^\dagger a + \frac{1}{2}\right),
\end{aligned}
$$

where terms $a^{\dagger^2}$ and a^2 have been neglected and

$$
\begin{aligned}
k_{ij} = c_{ij}g_{ji} = c_{ij}g_{ij}^* &= \frac{|g_{ij}|^2}{\omega_r+\omega_i-\omega_j}, \\
\chi_i &= \sum_j\left(k_{ij}-k_{ji}\right).
\end{aligned}
$$

Thus, the total Hamiltonian is

$$\mathscr{H}' = \left(\omega_r - \sum_i \chi_i\,|i\rangle\langle i|\right)a^\dagger a + \sum_i \frac{\omega_i-\chi_i}{2}\,|i\rangle\langle i|.$$

C

Schrieffer-Wolff approximation for PCR

For simplicity, let's start analyzing the case of an unbiased symmetric dc-SQUID, i.e. $g_1 = 0$. Since $|g_2| \ll \omega_{SQ}, \omega_q$, it is possible to find another form to express the TPJC Hamiltian in the dispersive regime, i.e. $|g_2| < \omega_r, \omega_q, |\omega_r \pm \omega_q|$.
In order to calculate the dispersive Hamiltonian, we use the Schrieffer-Wolff (SW) transformation:

$$\mathscr{H}' = U\mathscr{H}U^\dagger = e^S \mathscr{H} e^{-S} , \tag{C.1}$$

with S anti-Hermitian. As a consequence, it is well known that

$$U = e^S \longrightarrow U^\dagger = e^{S^\dagger} = e^{-S} ,$$

and thus, applying the Glauber's formula[1] [102], we have

$$UU^\dagger = e^S e^{-S} = e^{S+(-S)} e^{\frac{1}{2}[S,-S]} = 1 .$$

This condition ensures the SW transformation to be unitary.
Moving back to Eq. (C.1), it possible to employ the Baker-Campbell-Hausdorff (BCH) formula:

$$\mathscr{H}' = \mathscr{H} + [S,\mathscr{H}] + \frac{1}{2}[S,[S,\mathscr{H}]] + \dots \quad .$$

[1] Glauber's formula defines the product of two operators as

$$e^A e^B = e^{A+B} e^{\frac{1}{2}[A,B]} .$$

Since we want to reduce the Hamiltonian in Eq. (5.48) to a diagonal Hamiltonian, we can impose

$$[S, \mathscr{H}_0] = -\mathscr{H}_{TP} \,, \tag{C.2}$$

where $\mathscr{H}_0$ is the diagonal part of the TPJC Hamiltonian, whereas $\mathscr{H}_{TP}$ is the off-diagonal part, i.e. the interacting term. From now on, $\hbar = 1$ is used.
In this way, the BCH formula is reduced to

$$\mathscr{H}_{eff} = \mathscr{H}_0 + \frac{1}{2}[S, \mathscr{H}_{TP}] \,. \tag{C.3}$$

In order to calculate the dispersive Hamiltonian, the first step is to find S.
Following [101], since it has to be anti-Hermitian, let's define the commutator

$$\eta = [\mathscr{H}_0, \mathscr{H}_{TP}] \,,$$

which in our case is

$$\begin{aligned} \eta &= -\omega_{SQ} g_2 \left([a^\dagger a, a^2]\sigma_+ + [a^\dagger a, a^{\dagger 2}]\sigma_- \right) - \omega_q g_2 \left(a^2\sigma_+ - a^{\dagger 2}\sigma_- \right) = \\ &= g_2(\omega_q - 2\omega_{SQ}) a^2\sigma_+ - g_2(\omega_q - 2\omega_{SQ}) a^{\dagger 2}\sigma_- \,. \end{aligned} \tag{C.4}$$

Hence, S is

$$S = A a^{\dagger 2}\sigma_- + B a^2 \sigma_+ \,.$$

Thus, imposing Eq. (C.2):

$$\begin{aligned} [S, \mathscr{H}_0] &= -A\,(\omega_q - 2\omega_{SQ})\, a^{\dagger 2}\sigma_+ + B\,(2\omega_{SQ} - \omega_q)\, a^2\sigma_+ = \\ &= g_2 \left(a^{\dagger 2}\sigma_- + a^2\sigma_+ \right) \,, \end{aligned}$$

from which we find:

$$A = -B = \frac{g_2}{\omega_q - 2\omega_{SQ}} \longrightarrow S = -\frac{g_2}{2\omega_{SQ} - \omega_q} \left(a^{\dagger 2}\sigma_- - a^2\sigma_- \right) \,. \tag{C.5}$$

From this result, we can calculate the commutator

$$\begin{aligned} [S, \mathscr{H}_{TP}] &= \frac{g_2^2}{2\omega_{SQ} - \omega_q} \left[[a^2\sigma_+, a^{\dagger 2}\sigma_-] - [a^{\dagger 2}\sigma_-, a^2\sigma_+] \right] = \\ &= -2\chi \left[a^\dagger a \left(a^\dagger a + 1 \right) \sigma_z + 2a^\dagger a + \sigma_z + 2 \right] \,, \end{aligned} \tag{C.6}$$

with

$$\chi = \frac{g_2^2}{2\omega_{SQ} - \omega_q} = \frac{\Delta\omega_\pm^2}{2\omega_{SQ} - \omega_q} \,.$$

Similarly, it can be done considering both JC and TPJC contributions. The resulting off-diagonal terms can be neglected, as they are of higher-order approximation.

Bibliography

[1] Richard P Feynman. Quantum mechanical computers. *Found. Phys.*, 16(6): 507–532, 1986.

[2] Seth Lloyd. Quantum-mechanical computers. *Scientific American*, 273(4): 140–145, 1995.

[3] Benjamin Schumacher. Quantum coding. *Physical Review A*, 51(4):2738, 1995.

[4] Peter W Shor. Quantum computing. *Documenta Mathematica*, 1(1000): 467–486, 1998.

[5] Chris Monroe, David M Meekhof, Barry E King, Wayne M Itano, and David J Wineland. Demonstration of a fundamental quantum logic gate. *Physical review letters*, 75(25):4714, 1995.

[6] Andrea Morello, Jarryd J Pla, Floris A Zwanenburg, Kok W Chan, Kuan Y Tan, Hans Huebl, Mikko Möttönen, Christopher D Nugroho, Changyi Yang, Jessica A Van Donkelaar, et al. Single-shot readout of an electron spin in silicon. *Nature*, 467(7316):687–691, 2010.

[7] Emanuel Knill, Raymond Laflamme, and Gerald J Milburn. A scheme for efficient quantum computation with linear optics. *nature*, 409(6816):46–52, 2001.

[8] Yasunobu Nakamura, Yu A Pashkin, and JS Tsai. Coherent control of macroscopic quantum states in a single-cooper-pair box. *nature*, 398(6730): 786–788, 1999.

[9] JE Mooij, TP Orlando, L Levitov, Lin Tian, Caspar H Van der Wal, and Seth Lloyd. Josephson persistent-current qubit. *Science*, 285(5430):1036–1039, 1999.

[10] Denis Vion, A Aassime, Audrey Cottet, Pl Joyez, H Pothier, C Urbina, Daniel Esteve, and Michel H Devoret. Manipulating the quantum state of an electrical circuit. *Science*, 296(5569):886–889, 2002.

[11] Jens Koch, Terri M Yu, Jay Gambetta, Andrew A Houck, David I Schuster, Johannes Majer, Alexandre Blais, Michel H Devoret, Steven M Girvin, and Robert J Schoelkopf. Charge-insensitive qubit design derived from the cooper pair box. *Physical Review A—Atomic, Molecular, and Optical Physics*, 76 (4):042319, 2007.

[12] Andreas Wallraff, David I Schuster, Alexandre Blais, Luigi Frunzio, R-S Huang, Johannes Majer, Sameer Kumar, Steven M Girvin, and Robert J Schoelkopf. Strong coupling of a single photon to a superconducting qubit using circuit quantum electrodynamics. *Nature*, 431(7005):162–167, 2004.

[13] Bruno Apolloni, C Carvalho, and Diego De Falco. Quantum stochastic optimization. *Stochastic Processes and their Applications*, 33(2):233–244, 1989.

[14] Tadashi Kadowaki and Hidetoshi Nishimori. Quantum annealing in the transverse ising model. *Physical Review E*, 58(5):5355, 1998.

[15] Michel H Devoret et al. Quantum fluctuations in electrical circuits. *Les Houches, Session LXIII*, 7(8):133–135, 1995.

[16] Walther Meissner and Robert Ochsenfeld. Ein neuer effekt bei eintritt der supraleitfähigkeit. *Naturwissenschaften*, 21(44):787–788, 1933.

[17] Robert Doll and M Näbauer. Experimental proof of magnetic flux quantization in a superconducting ring. *Physical Review Letters*, 7(2):51, 1961.

[18] Fritz London and Heinz London. *Superfluids, Volume I: Macroscopic Theory of Superconductivity*. John Wiley & Sons, 1950.

[19] Brian David Josephson. Possible new effects in superconductive tunnelling. *Physics letters*, 1(7):251–253, 1962.

[20] Brian David Josephson. Supercurrents through barriers. *Advances in Physics*, 14(56):419–451, 1965.

[21] Philip W Anderson and John M Rowell. Probable observation of the josephson superconducting tunneling effect. *Physical Review Letters*, 10(6):230, 1963.

[22] Fritz London and Heinz London. The electromagnetic equations of the supraconductor. *Proceedings of the Royal Society of London. Series A-Mathematical and Physical Sciences*, 149(866):71–88, 1935.

[23] VL Ginzburg and LD Landau. Theory of superconductivity. *Zh. Eksp. Teor. Fiz.;(USSR)*, 20(12), 1950.

[24] John Bardeen, Leon N Cooper, and John Robert Schrieffer. Theory of superconductivity. *Physical review*, 108(5):1175, 1957.

[25] Nikolay N Bogoljubov, Vladimir Veniaminovic Tolmachov, and DV Širkov. A new method in the theory of superconductivity. *Fortschritte der physik*, 6 (11-12):605–682, 1958.

[26] Vitaly L Ginzburg. On the theory of superconductivity. *Il Nuovo Cimento (1955-1965)*, 2:1234–1250, 1955.

[27] Leon N Cooper. Bound electron pairs in a degenerate fermi gas. *Physical Review*, 104(4):1189, 1956.

[28] Antonio Barone and Gianfranco Paternò. *Physics and Applications of the Josephson Effect*. John Wiley & Sons, New York, 1982. ISBN 0-471-01469-9. doi: 10.1002/352760278X.

[29] Uri Vool and Michel Devoret. Introduction to quantum electromagnetic circuits. *International Journal of Circuit Theory and Applications*, 45(7): 897–934, 2017.

[30] Lev Davidovich Landau and Evgenii Mikhailovich Lifshitz. *Mechanics*, volume 1. CUP Archive, 1960.

[31] Herbert Goldstein, Charles Poole, John Safko, and Stephen R Addison. Classical mechanics, 2002.

[32] Juan José García Ripoll. *Quantum information and quantum optics with superconducting circuits*. Cambridge University Press, 2022.

[33] David M Pozar. *Microwave engineering: theory and techniques*. John wiley & sons, 2021.

[34] Simon Michael Doyle. *Lumped Element Kinetic Inductance Detectors*. Phd thesis, Cardiff University, Cardiff, Wales, UK, April 2008. URL https://orca.cardiff.ac.uk/id/eprint/54728/. Unpublished; deposit 30 March 2016.

[35] S Felicetti, DZ Rossatto, E Rico, E Solano, and P Forn-Díaz. Two-photon quantum rabi model with superconducting circuits. *Physical review A*, 97(1): 013851, 2018.

[36] Caspar H van der Wal, FK Wilhelm, CJPM Harmans, and JE Mooij. Engineering decoherence in josephson persistent-current qubits: Measurement apparatus and other electromagnetic environments. *The European Physical Journal B-Condensed Matter and Complex Systems*, 31:111–124, 2003.

[37] Patrick Winkel, Kiril Borisov, Lukas Grünhaupt, Dennis Rieger, Martin Spiecker, Francesco Valenti, Alexey V Ustinov, Wolfgang Wernsdorfer, and Ioan M Pop. Implementation of a transmon qubit using superconducting granular aluminum. *Physical Review X*, 10(3):031032, 2020.

[38] Lukas Grünhaupt, Martin Spiecker, Daria Gusenkova, Nataliya Maleeva, Sebastian T Skacel, Ivan Takmakov, Francesco Valenti, Patrick Winkel, Hannes Rotzinger, Wolfgang Wernsdorfer, et al. Granular aluminium as a superconducting material for high-impedance quantum circuits. *Nature materials*, 18(8):816–819, 2019.

[39] Kaushik Mitra, FW Strauch, CJ Lobb, JR Anderson, FC Wellstood, and Eite Tiesinga. Quantum behavior of a dc squid phase qubit. *Physical Review B—Condensed Matter and Materials Physics*, 77(21):214512, 2008.

[40] Terry P Orlando, JE Mooij, Lin Tian, Caspar H Van Der Wal, LS Levitov, Seth Lloyd, and JJ Mazo. Superconducting persistent-current qubit. *Physical Review B*, 60(22):15398, 1999.

[41] Yueyin Qiu, Wei Xiong, Xiao-Ling He, Tie-Fu Li, and JQ You. Four-junction superconducting circuit. *Scientific Reports*, 6(1):28622, 2016.

[42] Alexandre Blais, Arne L Grimsmo, Steven M Girvin, and Andreas Wallraff. Circuit quantum electrodynamics. *Reviews of Modern Physics*, 93(2):025005, 2021.

[43] Alexandre Blais, Ren-Shou Huang, Andreas Wallraff, Steven M Girvin, and R Jun Schoelkopf. Cavity quantum electrodynamics for superconducting electrical circuits: An architecture for quantum computation. *Physical Review A—Atomic, Molecular, and Optical Physics*, 69(6):062320, 2004.

[44] Leonid V Abdurakhimov, Imran Mahboob, Hiraku Toida, Kousuke Kakuyanagi, and Shiro Saito. A long-lived capacitively shunted flux qubit embedded in a 3d cavity. *Applied Physics Letters*, 115(26), 2019.

[45] Sunmi Kim, Leonid V Abdurakhimov, Duong Pham, Wei Qiu, Hirotaka Terai, Sahel Ashhab, Shiro Saito, Taro Yamashita, and Kouichi Semba. Superconducting flux qubit with ferromagnetic josephson π-junction operating at zero magnetic field. *Communications Materials*, 5(1):216, 2024.

[46] Fei Yan, Simon Gustavsson, Archana Kamal, Jeffrey Birenbaum, Adam P Sears, David Hover, Ted J Gudmundsen, Danna Rosenberg, Gabriel Samach, Steven Weber, et al. The flux qubit revisited to enhance coherence and reproducibility. *Nature communications*, 7(1):12964, 2016.

[47] R Trappen, X Dai, MA Yurtalan, D Melanson, DM Tennant, AJ Martinez, Y Tang, J Gibson, JA Grover, SM Disseler, et al. Decoherence of a tunable capacitively shunted flux qubit. *arXiv preprint arXiv:2307.13961*, 2023.

[48] J-L Orgiazzi, C Deng, D Layden, R Marchildon, F Kitapli, F Shen, M Bal, FR Ong, and A Lupascu. Flux qubits in a planar circuit quantum electrodynamics architecture: Quantum control and decoherence. *Physical Review B*, 93(10):104518, 2016.

[49] David López Núñez. *Coherent Flux Qubits for Quantum Annealing*. PhD thesis, 2024.

[50] Mattan Kamon, Michael J Tsuk, and Jacob White. Fasthenry: A multipole-accelerated 3-d inductance extraction program. In *Proceedings of the 30th international design automation conference*, pages 678–683, 1993.

[51] COMSOL Multiphysics. Introduction to comsol multiphysics®. *COMSOL Multiphysics, Burlington, MA, accessed Feb*, 9(2018):32, 1998.

[52] Slawomir Koziel. Multi-fidelity multi-grid design optimization of planar microwave structures with sonnet. *International Review of Progress in Applied Computational Electromagnetics*, 4:26–29, 2010.

[53] Lukas Grünhaupt, Uwe von Lüpke, Daria Gusenkova, Sebastian T Skacel, Nataliya Maleeva, Steffen Schlör, Alexander Bilmes, Hannes Rotzinger, Alexey V Ustinov, Martin Weides, et al. An argon ion beam milling process for native alox layers enabling coherent superconducting contacts. *Applied Physics Letters*, 111(7), 2017.

[54] Marius V Costache, German Bridoux, Ingmar Neumann, and Sergio O Valenzuela. Lateral metallic devices made by a multiangle shadow evaporation technique. *Journal of Vacuum Science & Technology B*, 30(4), 2012.

[55] Vinay Ambegaokar and Alexis Baratoff. Tunneling between superconductors. *Physical review letters*, 10(11):486, 1963.

[56] Paul V Klimov, Julian Kelly, Zijun Chen, Matthew Neeley, Anthony Megrant, Brian Burkett, Rami Barends, Kunal Arya, Ben Chiaro, Yu Chen, et al. Fluctuations of energy-relaxation times in superconducting qubits. *Physical review letters*, 121(9):090502, 2018.

[57] Jonathan J Burnett, Andreas Bengtsson, Marco Scigliuzzo, David Niepce, Marina Kudra, Per Delsing, and Jonas Bylander. Decoherence benchmarking of superconducting qubits. *npj Quantum Information*, 5(1):54, 2019.

[58] FG Paauw, A Fedorov, CJP M Harmans, and JE Mooij. Tuning the gap of a superconducting flux qubit. *Physical review letters*, 102(9):090501, 2009.

[59] Sergey Novikov, Robert Hinkey, Steven Disseler, James I Basham, Tameem Albash, Andrew Risinger, David Ferguson, Daniel A Lidar, and Kenneth M Zick. Exploring more-coherent quantum annealing. In *2018 IEEE International Conference on Rebooting Computing (ICRC)*, pages 1–7. IEEE, 2018.

[60] Kunihiro Inomata, Tsuyoshi Yamamoto, P-M Billangeon, Y Nakamura, and JS Tsai. Large dispersive shift of cavity resonance induced by a superconducting flux qubit in the straddling regime. *Physical Review B—Condensed Matter and Materials Physics*, 86(14):140508, 2012.

[61] IV Antonov, RS Shaikhaidarov, VN Antonov, and OV Astafiev. Superconducting 'twin'qubit. *Physical Review B*, 102(11):115422, 2020.

[62] P Forn-Díaz, L Lamata, E Rico, J Kono, and E Solano. Ultrastrong coupling regimes of light-matter interaction. *Reviews of Modern Physics*, 91(2): 025005, 2019.

[63] A Osman, J Simon, A Bengtsson, S Kosen, P Krantz, D P Lozano, M Scigliuzzo, P Delsing, Jonas Bylander, and A Fadavi Roudsari. Simplified josephson-junction fabrication process for reproducibly high-performance superconducting qubits. *Applied Physics Letters*, 118(6), 2021.

[64] John Taylor. *Introduction to error analysis, the study of uncertainties in physical measurements*. University Science Books, 1997.

[65] Jonas Bylander, Simon Gustavsson, Fei Yan, Fumiki Yoshihara, Khalil Harrabi, George Fitch, David G Cory, Yasunobu Nakamura, Jaw-Shen Tsai, and

William D Oliver. Noise spectroscopy through dynamical decoupling with a superconducting flux qubit. *Nature Physics*, 7(7):565–570, 2011.

[66] Mustafa Bal, Akshay A Murthy, Shaojiang Zhu, Francesco Crisa, Xinyuan You, Ziwen Huang, Tanay Roy, Jaeyel Lee, David van Zanten, Roman Pilipenko, et al. Systematic improvements in transmon qubit coherence enabled by niobium surface encapsulation. *npj Quantum Information*, 10(1): 43, 2024.

[67] Daniel Yuki Nakada. *Fabrication and measurement of a niobium persistent current qubit*. PhD thesis, Massachusetts Institute of Technology, 2004.

[68] Aaron Somoroff, Patrick Truitt, Adam Weis, Jacob Bernhardt, Daniel Yohannes, Jason Walter, Konstantin Kalashnikov, Mario Renzullo, Raymond A Mencia, Maxim G Vavilov, et al. Fluxonium qubits in a flip-chip package. *Physical Review Applied*, 21(2):024015, 2024.

[69] Pol Forn-Díaz, Jürgen Lisenfeld, David Marcos, Juan José Garcia-Ripoll, Enrique Solano, CJPM Harmans, and JE Mooij. Observation of the bloch-siegert shift in a qubit-oscillator system¡? format?¿ in the ultrastrong coupling regime. *Physical review letters*, 105(23):237001, 2010.

[70] Pol Forn-Diaz, J José García-Ripoll, Borja Peropadre, J-L Orgiazzi, MA Yurtalan, R Belyansky, Christopher M Wilson, and Adrian Lupascu. Ultrastrong coupling of a single artificial atom to an electromagnetic continuum in the nonperturbative regime. *Nature Physics*, 13(1):39–43, 2017.

[71] Thomas Niemczyk, F Deppe, H Huebl, EP Menzel, F Hocke, MJ Schwarz, JJ Garcia-Ripoll, D Zueco, T Hümmer, E Solano, et al. Circuit quantum electrodynamics in the ultrastrong-coupling regime. *Nature Physics*, 6(10): 772–776, 2010.

[72] Zhen Chen, Yimin Wang, Tiefu Li, Lin Tian, Yueyin Qiu, Kunihiro Inomata, Fumiki Yoshihara, Siyuan Han, Franco Nori, JS Tsai, et al. Single-photon-driven high-order sideband transitions in an ultrastrongly coupled circuit-quantum-electrodynamics system. *Physical Review A*, 96(1):012325, 2017.

[73] Alba Torras-Coloma, Luca Cozzolino, Ariadna Gómez del Pulgar-Martínez, Elia Bertoldo, and P. Forn-Díaz. Superinductor-based ultrastrong coupling in a superconducting circuit, 2025. URL https://arxiv.org/abs/2507.09339.

[74] David P DiVincenzo, Frederico Brito, and Roger H Koch. Decoherence rates in complex josephson qubit circuits. *Physical Review B—Condensed Matter and Materials Physics*, 74(1):014514, 2006.

[75] Dvir Kafri, Chris Quintana, Yu Chen, Alireza Shabani, John M Martinis, and Hartmut Neven. Tunable inductive coupling of superconducting qubits in the strongly nonlinear regime. *Physical Review A*, 95(5):052333, 2017.

[76] Conrad Wichmann and Ziwen Huang. Deriving effective coupling strength with born-oppenheimer approximation. Technical report, Fermi National Accelerator Laboratory (FNAL), Batavia, IL (United States), 2024.

[77] A Baust, E Hoffmann, M Haeberlein, MJ Schwarz, P Eder, J Goetz, F Wulschner, E Xie, L Zhong, F Quijandría, et al. Ultrastrong coupling in two-resonator circuit qed. *Physical Review B*, 93(21):214501, 2016.

[78] Steven J Weber, Gabriel O Samach, David Hover, Simon Gustavsson, David K Kim, Alexander Melville, Danna Rosenberg, Adam P Sears, Fei Yan, Jonilyn L Yoder, et al. Coherent coupled qubits for quantum annealing. *Physical Review Applied*, 8(1):014004, 2017.

[79] Caspar H Van Der Wal, ACJ Ter Haar, FK Wilhelm, RN Schouten, CJPM Harmans, TP Orlando, Seth Lloyd, and JE Mooij. Quantum superposition of macroscopic persistent-current states. *Science*, 290(5492):773–777, 2000.

[80] I Chiorescu, P Bertet, K Semba, Y Nakamura, CJPM Harmans, and JE Mooij. Coherent dynamics of a flux qubit coupled to a harmonic oscillator. *Nature*, 431(7005):159–162, 2004.

[81] A Lupaşcu, CJM Verwijs, RN Schouten, CJPM Harmans, and JE Mooij. Nondestructive readout for a superconducting flux qubit. *Physical review letters*, 93(17):177006, 2004.

[82] A Lupaşcu, Shiro Saito, Thibaut Picot, PC De Groot, CJPM Harmans, and JE Mooij. Quantum non-demolition measurement of a superconducting two-level system. *nature physics*, 3(2):119–123, 2007.

[83] A Lupaşcu, EFC Driessen, Leif Roschier, CJPM Harmans, and JE Mooij. High-contrast dispersive readout of a superconducting flux qubit using a nonlinear resonator. *Physical review letters*, 96(12):127003, 2006.

[84] I Siddiqi, R Vijay, M Metcalfe, E Boaknin, L Frunzio, RJ Schoelkopf, and MH Devoret. Dispersive measurements of superconducting qubit coherence

with a fast latching readout. *Physical Review B—Condensed Matter and Materials Physics*, 73(5):054510, 2006.

[85] Irfan Siddiqi, R Vijay, F Pierre, CM Wilson, L Frunzio, M Metcalfe, C Rigetti, and MH Devoret. The josephson bifurcation amplifier for quantum measurements. *Quantum Computing in Solid State Systems*, pages 28–37, 2006.

[86] Hyeokshin Kwon, AJ Przybysz, TA Palomaki, RM Lewis, BS Palmer, H Paik, SK Dutta, BK Cooper, JR Anderson, CJ Lobb, et al. Dc squid phase qubit with an lc filter. *IEEE transactions on applied superconductivity*, 19(3): 957–960, 2009.

[87] Hanhee Paik, SK Dutta, RM Lewis, TA Palomaki, BK Cooper, RC Ramos, H Xu, AJ Dragt, JR Anderson, CJ Lobb, et al. Decoherence in dc squid phase qubits. *Physical Review B—Condensed Matter and Materials Physics*, 77(21):214510, 2008.

[88] Eyob A Sete, John M Martinis, and Alexander N Korotkov. Quantum theory of a bandpass purcell filter for qubit readout. *Physical Review A*, 92(1): 012325, 2015.

[89] Göran Wendin and VS Shumeiko. Superconducting quantum circuits, qubits and computing. *arXiv preprint cond-mat/0508729*, 2005.

[90] Borja Peropadre, Pol Forn-Díaz, Enrique Solano, and Juan José García-Ripoll. Switchable ultrastrong coupling in circuit qed. *Physical review letters*, 105(2):023601, 2010.

[91] JNL Connor, T Uzer, RA Marcus, and AD Smith. Eigenvalues of the schrödinger equation for a periodic potential with nonperiodic boundary conditions: A uniform semiclassical analysis. *The Journal of chemical physics*, 80(10):5095–5106, 1984.

[92] P Bertet, I Chiorescu, CJPM Harmans, and JE Mooij. Dephasing of a flux-qubit coupled to a harmonic oscillator. *arXiv preprint cond-mat/0507290*, 2005.

[93] Patrice Bertet, Irinel Chiorescu, Guido Burkard, Kouichi Semba, CJPM Harmans, David P DiVincenzo, and JE Mooij. Relaxation and dephasing in a flux-qubit. *arXiv preprint cond-mat/0412485*, 2004.

[94] You-Fei Xie, Liwei Duan, and Qing-Hu Chen. Generalized quantum rabi model with both one-and two-photon terms: A concise analytical study. *Physical Review A*, 99(1):013809, 2019.

[95] Hossein Fakhri, S Mirzaei, and M Sayyah-Fard. Two-photon jaynes–cummings model: a two-level atom interacting with the para-bose field. *Quantum Information Processing*, 20(12):398, 2021.

[96] CV Sukumar and B Buck. Multi-phonon generalisation of the jaynes-cummings model. *Physics Letters A*, 83(5):211–213, 1981.

[97] Dean G Jarrett, Ching-Chen Yeh, Shamith U Payagala, Alireza R Panna, Yanfei Yang, Linli Meng, Swapnil M Mhatre, Ngoc Thanh Mai Tran, Heather M Hill, Dipanjan Saha, et al. Star-mesh quantized hall array resistance devices. *arXiv preprint arXiv:2304.11243*, 2023.

[98] E.B. Curtis, D. Ingerman, and J.A. Morrow. Circular planar graphs and resistor networks. *Linear Algebra and its Applications*, 283(1):115–150, 1998.

[99] Caroline A Schneider, Wayne S Rasband, and Kevin W Eliceiri. Nih image to imagej: 25 years of image analysis. *Nature methods*, 9(7):671–675, 2012.

[100] Julia Zotova, Rui Wang, Alexander Semenov, Yu Zhou, Ivan Khrapach, Akiyoshi Tomonaga, Oleg Astafiev, and Jaw-Shen Tsai. Compact superconducting microwave resonators based on al-alo x-al capacitors. *Physical Review Applied*, 19(4):044067, 2023.

[101] Rukhsan Ul Haq and Keshav Singh. A systematic method for schrieffer-wolff transformation and its generalizations. *arXiv preprint arXiv:2004.06534*, 2020.

[102] C. Cohen-Tannoudji, B. Diu, and F. Laloë. *Quantum Mechanics, Volume 1: Basic Concepts, Tools, and Applications*. Wiley, 2019. ISBN 9783527345533. URL https://books.google.es/books?id=tVI_EAAAQBAJ.